Research Papers
Issue RP0285
October 2017

CMCC Division:
Climate Simulations
and Predictions CSP

RP0285 – CMCC-SPS3: The CMCC Seasonal Prediction System 3

By ***Antonella Sanna***
Fondazione CMCC
antonella.sanna@cmcc.it

Andrea Borrelli
Fondazione CMCC
andrea.borrelli@cmcc.it

Panos Athanasiadis
Fondazione CMCC
panos.athanasiadis@cmcc.it

Stefano Materia
Fondazione CMCC
stefano.materia@cmcc.it

Andrea Storto
Fondazione CMCC
andrea.storto@cmcc.it

Antonio Navarra
Fondazione CMCC
INGV
antonio.navarra@cmcc.it

Stefano Tibaldi
Fondazione CMCC
stefano.tibaldi@cmcc.it

and ***Silvio Gualdi***
Fondazione CMCC
silvio.gualdi@cmcc.it

Acknowledgments: The activities leading to these results has received funding from the Copernicus Climate Change Service (C3S) program under the D433_Lot2 tender project.

SUMMARY

This technical report describes the new Seasonal Prediction System developed at CMCC to perform seasonal forecasts operationally (CMCC-SPS3). A more realistic representation of the Climate System components such as the ocean, the sea ice, the snow cover, the soil moisture and the stratosphere is crucial to obtain reliable forecasts at the sub-seasonal to seasonal time-scale. This new Seasonal Prediction System currently operational at the Euro-Mediterranean Center on Climate Change was indeed developed with the aim of achieving enhanced predictive skill in a variety of different aspects. In comparison to the previous system (SPS2), the new model has a completely different dynamical core, based on the new CMCC Earth System Model (Fogli and Iovino, 2014). The new system features a better horizontal resolution of both the atmospheric and oceanic components, better representation of the stratosphere, more realistic initialization procedures for atmosphere, land, sea and ice modules and a larger ensemble size (50 members). Such improvements have a positive impact on the climate and on the predictive skill of the new system. After a brief description of each system component, the initialization strategy is discussed along with the main characteristics of the forecast system from a technical point of view. An analysis of its climate and of the forecasting skill is presented for the 24-year re–forecast period 1993–2016. The technical report is concluded with a preliminary attempt of comparison of the SPS3 overall performances with both SPS2 and other Seasonal Prediction Systems.

Keywords Seasonal Predictions, Climate Model, Ensemble Forecasts

CONTENS:

1. INTRODUCTION

The Euro-Mediterranean Center on Climate Change (CMCC) has developed a multi-year experience in Seasonal Forecasting. Since the turn of this century, a seasonal forecasting system has been operated by CMCC in research mode, and in particular within the DEMETER project (1999–2003). This System was originally based on the SINTEX model (Gualdi et al., 2003), implemented at a T42 horizontal resolution and with 19 vertical levels. The initial conditions were obtained from forced integrations of the atmospheric (AMIP-like runs) and oceanic (OMIP-like runs) components. This Seasonal Prediction System contributed to the DEMETER Multi Model Ensemble (Palmer et al., 2004) and sensitivity experiments were carried out to assess its performance in predicting ENSO (Gualdi et al., 2005).

Since May 2014, the second version (SPSv2, Materia et al., 2014; Athanasiadis et al., 2014) of the CMCC seasonal forecasting system has become fully operational in the framework of the CLIMAFRICA EU-Project (2010-2014). Since then, forecast products (from an ensemble of nine members) are delivered on a monthly basis (by the 15th of each month) to the Asian Pacific Climate Centre, South Korea (APCC, http://www.apcc21.org/eng/index.jsp), where they contribute to a multi model ensemble system (which includes NCEP, NASA, POAMA and two Canadian seasonal forecasting models) to generate global seasonal forecasts for a wide variety of users (Min et al., 2014).

Finally, since the 1st of July 2016, CMCC has started delivering Pre-Operational Global Seasonal Predictions to Copernicus C3S, as part of the Copernicus C3S_433_LOT2 Contract (the so-called POP Phase).

The fully coupled atmosphere-land-ocean-ice model at the heart of the currently operational system, the CMCC-SPS3 which is the object of this Technical Report, is based on the CMCC–CM2 coupled model (Fogli and Iovino, 2014). This, in turn, consists of several independent model components simultaneously simulating the

Earth's atmosphere, ocean, land, land and sea ice, together with a central coupler/driver component that controls data synchronization and exchange.

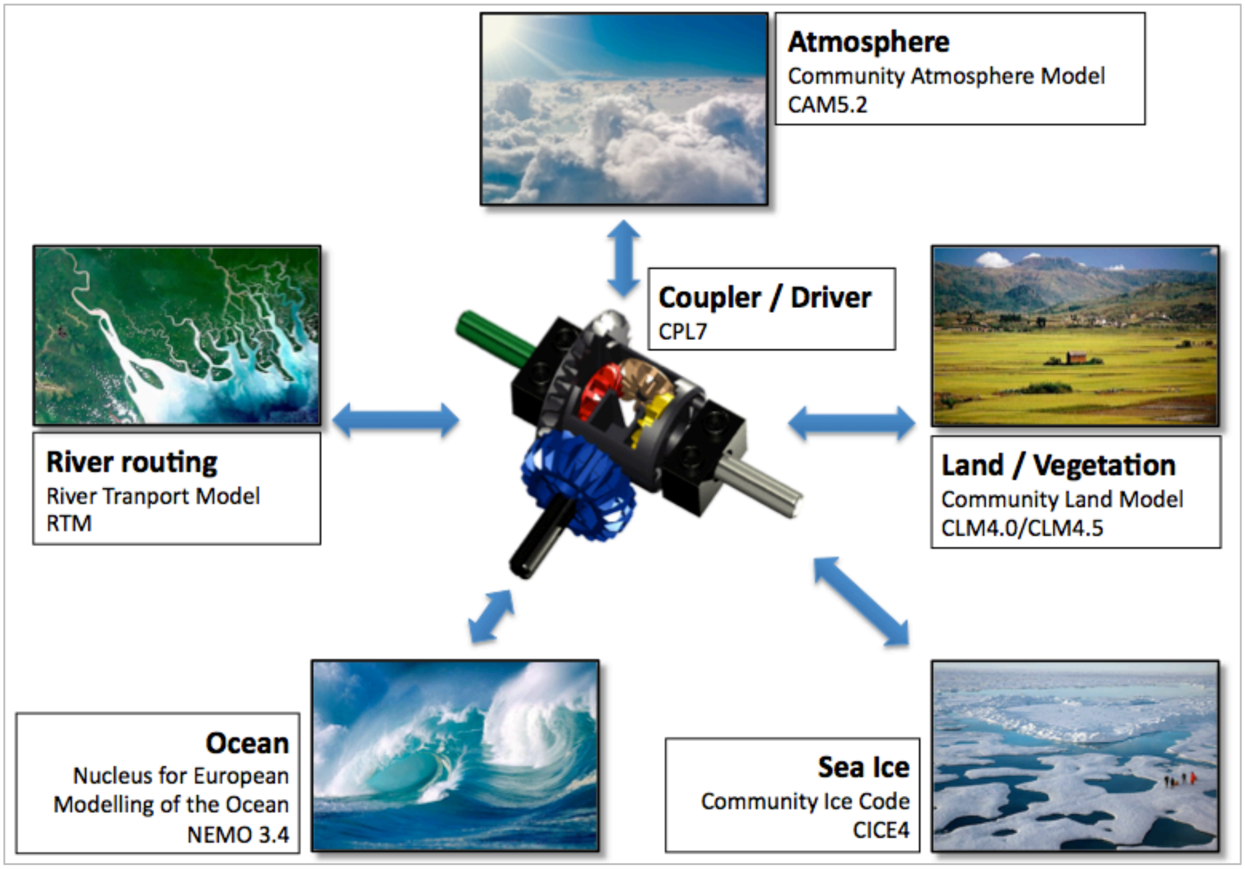

Figure 1. Scheme of the CMCC-SPS3 fully coupled Climate Model

The system can be configured in a number of different ways from both a scientific and technical perspective and can be efficiently run on various hardware platforms. It supports many resolutions and has the flexibility to set up simulations with different component configurations and parallel decompositions, which allows it to be run from a single atmosphere-only model in stand-alone forced configuration to the fully interactive coupled system.

The global model components can be combined in numerous ways, according to the different user's need and science perspectives. In the general framework of the seasonal forecast structure, the model is set in transient, fully-coupled configuration, with annually-varying greenhouse gases as established by the CMIP5 protocol (scenario RCP8.5 after 2005, see IPCC 2013).

Figure 1.1 shows a schematic of the CMCC–CM2 model components. The CMCC-CM2 atmospheric, land surface and sea ice models are based on the Community Earth System Model version 1.2.2 and a detailed description is given in Hurrell et al. (2013) and references therein. The ocean component is the European model Nucleus for European Modelling of the Ocean (NEMO), in its 3.4 version (for a detailed description, see Madec et al., 2008).

The purpose of this report is to provide, in addition to a description of the system and of its components, a preliminary, although fairly complete, assessment of the quality of the CMCC-SPS3 forecasting system, both in terms of model climate and of forecast performance.

2. SYSTEM COMPONENTS

2.1 ATMOSPHERE

The atmospheric component of CMCC-SPS3 is the Community Atmosphere Model version 5 (CAM5.3, see Neale et al., 2010 for a description of the model macrophysics) which can be configured to use a spectral transform, a finite volume or a finite elements dynamical core. The atmosphere implemented in the CMCC-SPS3 runs in the spectral element configuration (a formulation of the finite element method that uses high degree hybrid polynomials as basis functions, Patera 1984), with a horizontal resolution of about 110 km, 46 vertical levels up to about 0.3 hPa and an integration time-step of 30 minutes.

A description of the treatment for stratiform cloud formation, condensation, and evaporation macrophysics is given in Neale et al. (2012). A two-moment microphysical parameterization (Morrison and Gettelman, 2008; Gettelman et al. 2008) is used to predict the mass and number of smaller cloud particles (liquid and ice), while the mass and number of larger-precipitating particles (rain and snow) are diagnosed. Cloud microphysics is currently coupled to a fixed climatology of aerosols (referring to the year 2000), but there is an available option to combine it to a modal aerosol treatment (Liu et al,. 2012) that predicts the aerosol mass and number of internal mixtures of black and organic carbon, dust, sea salt, and sulfate aerosols. A Rapid Radiative Transfer Model for GCMs (RRTMG; Iacono et al., 2008) is used to calculate the radiative fluxes and heating rates for gaseous and condensed atmospheric species. A statistical technique is used to represent sub-grid-scale cloud overlap (Pincus et al., 2003). New moist turbulence (Bretherton and Park, 2009) and shallow convection parameterization schemes (Park and Bretherton, 2009) provide substantial improvements to the simulation of shallow clouds in the boundary layer.

As previously mentioned, the version of CAM5 used has a modified vertical grid that has 46 levels instead of 30 and a model top at 0.3 hPa instead of at about 2 hPa. This 46LCAM5 includes a parameterization of non-orographic gravity waves following Richter et al. (2014). The convective gravity wave efficiency was adjusted to produce a QBO period in the lower stratosphere similar to observations.

2.2 OCEAN

The Nucleus for European Modelling of the Ocean (NEMO) is a flexible tool for representing the ocean and its interactions with the other components of the Earth climate system over a wide range of spatial and temporal scales. The NEMO model solves the primitive equations subject to the Boussinesq, hydrostatic and incompressibility approximations. The prognostic variables are the three velocity components, the sea surface height, the potential temperature and the practical salinity.

The ocean component used in CMCC-SPS3 is based on the eddy-permitting version 3.4 of NEMO, with a horizontal resolution of about 25 km, 50 vertical levels (31 in the first 500 m) and an integration time-step of 18 minutes.

In the horizontal direction, the model uses a nearly isotropic curvilinear orthogonal grid with an Arakawa C–type three-dimensional arrangement of variables. For our global configurations, we use tri-polar ORCA-like grids (based on Mercator projection), which have a pole in the Southern Hemisphere collocated with the geographic South Pole and two poles placed on land in the Northern Hemisphere (in Siberia and Canada) in order to overcome the North Pole singularity. Poleward of 20°N, the two poles introduce a weak anisotropy over the ocean areas. CMCC-CM2 marine component may be run in two configurations: a lower 1° resolution (ORCA1) and a higher, eddy-permitting, 1/4° resolution, which is the one used in the seasonal forecast system.

The model uses a filtered, linear, free-surface formulation, where lateral water, tracers and momentum fluxes are calculated using fixed-reference ocean surface height. The time integration scheme used is a Robert–Asselin filtered leapfrog for non-diffusive processes and a forward (backward) scheme for horizontal (vertical) diffusive processes (Griffies, 2004). The linear free-surface is integrated in time implicitly using the same time step.

NEMO uses a non-linear equation of state. Tracers advection uses a Total Variance Dissipation (TVD) scheme while momentum advection is formulated in vector invariant form, using an energy and enstrophy conserving scheme (Zalesak, 1979). The vertical physics is parameterized using a Turbulent Kinetic Energy (TKE) closure scheme (Gaspar, 1990) plus parameterizations of double diffusion, Langmuir cell and surface wave breaking. An enhanced vertical diffusion parameterization is used in regions where the stratification becomes unstable. Tracers' lateral diffusion uses a diffusivity coefficient scaled according to the grid spacing, while lateral viscosity makes use of a space-varying coefficient. Both are parameterized by a horizontal bi-Laplacian operator. Free-slip boundary conditions are applied at the ocean lateral boundaries. At the ocean floor, a bottom intensified tidally-driven mixing (Simmons et al., 2004), a diffusive bottom boundary layer scheme and a nonlinear bottom friction are applied. No geothermal heat flux is applied through the ocean floor. The shortwave radiation from the atmosphere is absorbed in the surface layers using RGB chlorophyll-dependent attenuation coefficients.

2.3 SEA ICE

The sea ice component is version 4 of the Community Ice CodE (CICE4) (Hunke and Lipscomb, 2008) which uses the same horizontal grid of the ocean model, but an integration timestep of 30 minutes. It includes the thermodynamics of Bitz and Lipscomb (1999), the elastic–viscous–plastic dynamics of Hunke and Dukowicz (2002), and a subgrid scale representation of ice thickness distribution following Thorndike et al. (1975).

As documented in Holland et al. (2012), the most notable improvements in the sea ice component of CESM compared to earlier model versions includes a multiple scattering shortwave radiation treatment (Briegleb and Light, 2007) and associated capabilities to simulate explicitly melt pond evolution and the deposition and cycling of aerosols (dust and black carbon) within the ice pack. These new capabilities influence both the mean climate state and simulated climate feedbacks at high latitudes (Holland et al., 2012).

2.4 LAND SURFACE

The land component is the Community Land Model (CLM4.5) (Oleson et al., 2013), designed to represent and enable study of the physical, chemical, and biological processes by which terrestrial ecosystems affect and are affected by climate, across a variety of spatial and temporal scales.

CLM4.5 runs at the same resolution as the atmospheric model (about 1 degree), with a 30 minute time-step. The configuration incorporated in CMCC-SPS3 includes a treatment of mass and energy fluxes associated with prescribed temporal change in land cover. Using an annual time series of the spatial distribution of plant functional types (PFTs) and wood harvest, CLM4.5 diagnoses the change in area for each PFT at every model time step by performing mass and energy balance that cause variations of PFT area during the six-month integration.

A revised snow model incorporates the Snow, Ice, and Aerosol Radiation (SNICAR) model (Flanner et al. 2007). SNICAR includes aerosol deposition of black carbon and dust (either prescribed or prognostically determined by CAM), grain-size dependent snow aging, and vertically resolved snowpack heating. Dust is mobilized from the land by winds (Zender et al., 2003) and passed to the atmospheric aerosol model.

The representation of permafrost was significantly improved in CLM4 (Lawrence et al., 2011), while in this version a perched water table above icy permafrost ground is introduced (Swenson et al., 2012). The lake model in use in CLM4 is replaced with a revised more realistic one (Subin et al., 2012); a surface water is introduced, permitting prognostic wetland distribution and the energy fluxes are calculated separately for snow/water-covered and snow/water-free land and glacier units.

New features like a prognostic carbon–nitrogen (CN) model (Thornton et al., 2007) and an urban canyon model (Oleson et al., 2008) are not switched on in the SPS configuration, nor is a transient land cover and land use change capability, including wood harvest (Lawrence et al., 2012). Following the choice of keeping the CN model off, the crop model, based on agricultural version of the Integrated Biosphere Simulator (AgroIBIS, Kucharik and Brye, 2003), is also not active.

2.5 RIVER ROUTING

The RTM (River Transport Model) was developed to route total runoff from the land surface model to either the active ocean, or to marginal seas with a design that enables the hydrologic cycle to be closed (Branstetter, 2001; Branstetter and Famiglietti, 1999). The horizontal resolution is half-degree (about 50km) and the integration time-step is three-hourly.

2.6 THE COUPLER

All system components are synchronized by the CESM coupler/driver (cpl7) (Craig et al., 2011). The coupling architecture provides plug-and-play capability of data and active components and includes a user-friendly scripting system and informative timing utilities. Together, these tools enable a user to create a wide variety of out of the box experiments for different model configurations and resolutions and also to determine the optimal load balance for those experiments to ensure maximal throughput and efficiency. In CMCC-SPS3, the coupling is performed every 90 minutes.

3. INITIAL CONDITIONS

An important feature implemented in the CMCC-SPS3 concerns the more realistic methodology of producing the initial conditions (ICs) for the ocean, land-surface and sea ice models, with substantial improvement with respect to the previous system (CMCC-SPS2, Materia et al., 2014; Athanasiadis et al., 2014). Moreover, in order to increase the signal-to-noise ratio (signal being the predictable component of the climate variability, and noise the inherently unpredictable chaotic component), the ensemble size of re-forecasts has been significantly increased from nine to forty members, and to fifty members in the real-time forecast configuration.

3.1 ATMOSPHERE

The atmospheric component is initialized, for all historical re-forecasts, with data from the ERA Interim reanalysis (Berrisford et al., 2009, hereafter ERAI). The multilevel fields (e.g. temperature, specific humidity, zonal and meridional wind) are interpolated from the 60 hybrid levels of ERAI to the 46 hybrid levels of CAM5.3. In the real-time forecast configuration, ECMWF real-time operational analyses are currently used in place of the previously used ECMWF MARS-derived fields, since operational analyses are available 24h in advance of MARS-derived fields, allowing a considerable operational speed-up.

The basic vertical interpolation approach is to calculate the pressure at each level for the input and output hybrid levels, and then interpolate the input variable to the pressures of the desired output hybrid levels. Log-linear interpolation is used.

At each latitude, longitude and level (lev[k]) pressure is computed using an NCAR Command Language (NCL) built-in function:

$$p(k) = A(k)*p0 + B(k)*ps \qquad (1)$$

where p0 is the surface reference pressure, ps is the surface pressure and A and B are two empirical coefficients.

Surface ICs (surface pressure, geopotential height, surface temperature, land-sea mask and snow depth) are subject to a horizontal bi-linear interpolation from the T159 ERA-Interim Gaussian Grid (ECMWF operational analyses in the real-time forecasting configuration) to the spectral elements grid, at about one-degree horizontal resolution.

3.2 OCEAN AND SEA-ICE

The initial conditions for the ocean and the sea-ice components are provided by the monthly reanalysis of the eddy-permitting C-GLORS ocean data assimilation system (Storto et al., 2011). Data assimilation is performed with a 3D variational data assimilation scheme (Courtier et al., 1998) which adjusts the initial value of the mathematical model rather than changing the state directly at analysis time, as it was the case in the optimal statistical interpolation used for the ocean reanalyses that were initializing the previous operational system CMCC-SPS2. The model used to produce the reanalysis instrumental for the monthly ocean initial condition set is the same as the ocean component of CMCC-SPS3, that is NEMO at ¼° horizontal resolution and 50 vertical levels.

For the re-forecast period, the ocean and sea-ice initial conditions have been obtained from a re-analysis spanning the period 1993-2016, which includes:

i. a three-dimensional variational data assimilation scheme, called OceanVarthat (Dobricic and Pinardi, 2008; Storto et al., 2014), which assimilates hydrographic profiles from the U.K. MetOffice Hadley Centre EN3 dataset (Ingleby and Huddlestone, 2007) supplemented by the EN4 dataset (Good et al., 2013) and along-track altimetric observations provided by AVISO (Storto et al., 2011);

ii. the NEMO ocean model, configured at ¼ degree resolution using a tripolar grid, with 50 vertical depth levels with partial steps and coupled to the LIM2 sea-ice model;

iii. a nudging scheme that assimilates space-borne sea-surface temperature observations supplied by NOAA (Reynolds et al., 2007), sea-ice concentration data supplied by NSIDC (Cavalieri et al., 1999) and sea-ice thickness fields analysed by the Pan-Arctic Ice Ocean Modelling and Assimilation System (PIOMAS, Zhang and Rothrock, 2003);

iv. and a large-scale bias-correction scheme that corrects the model tendencies in order to limit the large-scale biases induced by the model and by the atmospheric forcing.

C-GLORS has been forced with both ECMWF ERA-Interim (Dee et al., 2011) re-analyses and NCEP Reanalyses v1 (Kalnay et al., 1996), using the bulk formulas proposed by Large and Yeager (2004).

The atmospheric fields used are three-hourly temperature and humidity at 2 meters, wind at 10 meters, daily short-wave and long-wave radiation and total and solid precipitation. The shortwave radiation is modulated through a scheme that reproduces the diurnal cycle (Bernie et al., 2007). Further details on the analysis-reanalysis system and its performance are available in Storto et al. (2014), where the positive contributions of all assimilation components (OceanVar, surface nudging, LSBC) to the overall accuracy of C-GLORS are documented. Ocean and sea-ice initial conditions for the operational seasonal forecasts are produced by C-GLORS with atmospheric fields obtained from both ECMWF and NCEP analyses relative to the period immediately preceding the forecast starting date.

The ICs for the sea-ice component are produced at the same time as the ocean reanalysis. Since, technically, the CICE model was originally designed to start from two possible configurations (namely a sea-ice climatology and a prescribed analytical distribution) an ad-hoc routine was developed in order to allow the model to use the actual IC provided by the reanalysis.

3.3 LAND

In CMCC-SPS3, initialization of the land component is achieved through a Land Data Assimilation System (LDAS, Koster et al., 2009). The technique consists of forcing a land-surface model (CLM4.5, the Common Land Model version 4, i.e. the land component of SPS3, uncoupled from an atmospheric model) with observed, near-surface meteorological fields variables consisting of incoming solar radiation, total precipitation (solid and liquid), surface pressure, 2m-specific humidity, 2m-temperature and 10m-horizontal wind, and then let the model evolve freely in response to observations. This approach allows full initialization of the land component, including the sub-surface portion, which stores the greater part of the information beneficial for predictions at the seasonal scale, and allows fully consistent simulation of land properties.

The atmospheric boundary conditions are provided by either NCEP or ERAI reanalysis (ECMWF operational analyses in the real-time forecasting configuration) datasets. This provides, in principle, two possible (equivalent) land initialization datasets which will be used to generate the initial condition ensemble (see the following Sect. 4). The simulation starts from arbitrary ICs (the so-called “cold start” configuration) and needs a certain amount of time to create a physically sound and well-balanced state of the soil. Since the Carbon-Nitrogen model, which would require hundreds of years to reach equilibrium, is not active, a few years of integration are considered sufficient for this particular purpose. A 20-year spin-up (1973-1992) has been tested to provide an untrended time-series of soil moisture and soil temperature, so the 31st December restart was used as the first land-surface initial condition.

4. GENERATION OF THE PREDICTION ENSEMBLE

In order to take account of the uncertainty associated with the initial conditions, 50 (40) perturbations of the initial state are built for the forecasts (re-forecasts), creating in this way a rather large ensemble of possible initial states for CMCC-SPS3. Perturbations are generated by combining the initial states of the three main components: the atmosphere (10 perturbations of the tropospheric layers), the ocean (8 perturbations for the real-time forecasts, 4 for the re-forecasts) and the land surface (3 perturbations). Out of the possible 240 (10x8x3, reduced to 120 in the re-forecast configuration, 10x4x3), 50 (40) unique combinations are randomly chosen to compose the CMCC-SPS3 initial conditions set.

The way in which perturbations are constructed differs for each system component:

- **Atmosphere**. The atmospheric initial condition of CMCC-SPS3 is provided by the ECMWF operational analysis (the ERAI atmospheric reanalysis for the re-forecasts) at 00z UTC on day 1 of the start month. Further nine alternative initial conditions are generated with a time-lagging technique. This means that the ECMWF operational analyses (ERAI reanalyses for the re-forecasts), based on synoptic times of the preceding 12, 24, 36, … hours, and so on, back to 120 hours before the start date are used. For all initial conditions starting at 12z UTC, a 12h time realignment forecast is performed, so that all lagged ICs start at 00z UTC.

- **Ocean**. Both the assimilated observations and the atmospheric forcing (winds, short- and long-wave radiation, 2-meter temperature and specific humidity, precipitation) of the control ocean data-assimilation model are perturbed. The observations are perturbed by adding a random error proportional to the mean observational error. The atmospheric forcing perturbation is constructed by computing, for each month and each variable, the daily differences between the atmospheric forcing datasets (NCEP and operational ECMWF or ERAI), and randomly adding one of these field differences to each daily forcing.

- **Land-surface**. Land surface is perturbed by modifying the atmospheric boundary conditions (2-meter temperature, sea level pressure, 2-meter specific humidity, 10-meter winds, precipitation and surface solar radiation) in the land component forced simulation. The required variables are derived using three datasets: ERAI, NCEP and a linear interpolation of the two. With this forcing imposed every three or six hours, CLM4.5 produces three comparable restarts that are used as initial conditions.

5. THE MODEL CLIMATE: BIAS

The evaluation of the model climate is based on the entire set of 24 years of seasonal forecasts (the “re–forecasts”) performed on the four canonical starting dates of February 1st, May 1st, August 1st and November 1st and will be based on global fields of atmospheric temperature, surface temperature and precipitation and on hemispheric fields (NH and SH) of mean sea-level pressure and 500 hPa geopotential height. Such fields will be shown as mean model-produced fields and differences from an observed climate for the corresponding period. The averaging period will mostly be three months, for lead 0 and lead 3 periods. This will allow an estimate of the climate drift of the model as portrayed by the comparison between the first three (lead 0) and the second three months (lead 3) of the forecasting period.

5.1 THE RE-FORECASTS

The complete forecast system in full operational configuration has been re-run over the 24-year-period 1993–2016 from all first-of-the-month starting dates and for a six-month forecast period. The system was run in ensemble mode with a population of 40 members. A model climatological mean has then been constructed, which is compared to ERA Interim for the same time frame. This allows an assessment of the model systematic error in terms of mean bias and variability and provides a good statistical basis to compute predicted anomalies from the model climate, thereby attempting to remove mean model bias from the re–forecasts. Bias removal (by computing predicted anomalies from the model climate) is an operational standard practice to improve the model's performance in forecasting mode and performance assessment.

With the purpose of maintaining manageable the number of maps and graphs displayed while providing a fairly complete overall picture of the model's behaviour and skill, this technical report will mostly concentrate on three-monthly mean fields for four staring dates (February, May, August and November) for lead 0 and lead 3 (the first three months and the second three months of the seasonal forecasts).

5.2 ATMOSPHERIC TEMPERATURE BIASES

For the purpose of this Technical Report, the diagnostics of atmospheric temperature will be limited to global 2m Temperature for all four starting dates (SDs) and to 850 hPa temperature for the May and November starting dates. Section 9.2 contains a comparison of T2m Bias with other state-of-the art SPSs.

5.2.1 2M TEMPERATURE BIAS

Temperature at 2 meter (T2m) is an extremely useful near-surface parameter and, together with precipitation, one of the most requested and used by seasonal forecasts users. As for all other diagnostics, we will concentrate on three-monthly mean fields at lead 0 and lead 3 (the first three and the second three months of the forecast integrations). Maps will be presented for the four canonical SDs (February, May, August and September). The re-forecasts span the 24-year period from 1993 to 2016 and always refer to 40 members ensemble sets. Figure 5.1 and 5.2 show T2m mean map (upper), bias (lower), lead 0 (left) and lead 3 (right) for all four SDs in sequence. Because of the very large influence of the seasonal cycle on T2m parameter, lead 0 maps of a given start date are always much more similar to lead 3 maps of the preceding start date than they are to the lead 3 maps of the same start date.

During NH winter months (lead 0, Nov SD and lead 3 Aug SD), temperature biases tend to be negative (up to 2–3°C) over the higher latitude continental areas of North America, Greenland and Eurasia, while they are almost zero or slightly positive over the lower latitudes of Europe and Asia and selected portions of North America. Positive biases up to 3-4°C can be seen over NH Polar Regions. Light, positive values dominate the continental areas of the SH. The biases are much lower on oceanic areas, as it is to be expected because of the higher predictability of the SSTs and of the influence they have over T2m. The bias is always increasing from lead 0 to lead 3, even in seasonal transition periods.

During summer and autumn months, two fairly large areas of cold bias (up to 2-3°C) become evident in the eastern part of both the Atlantic and the Pacific Ocean basins, mostly limited to NH midlatitude and Tropics.

The overall amplitude and spatial structure of the SPS3 lead 0 T2m biases are, in any case, comparable with similar seasonal prediction global coupled models.

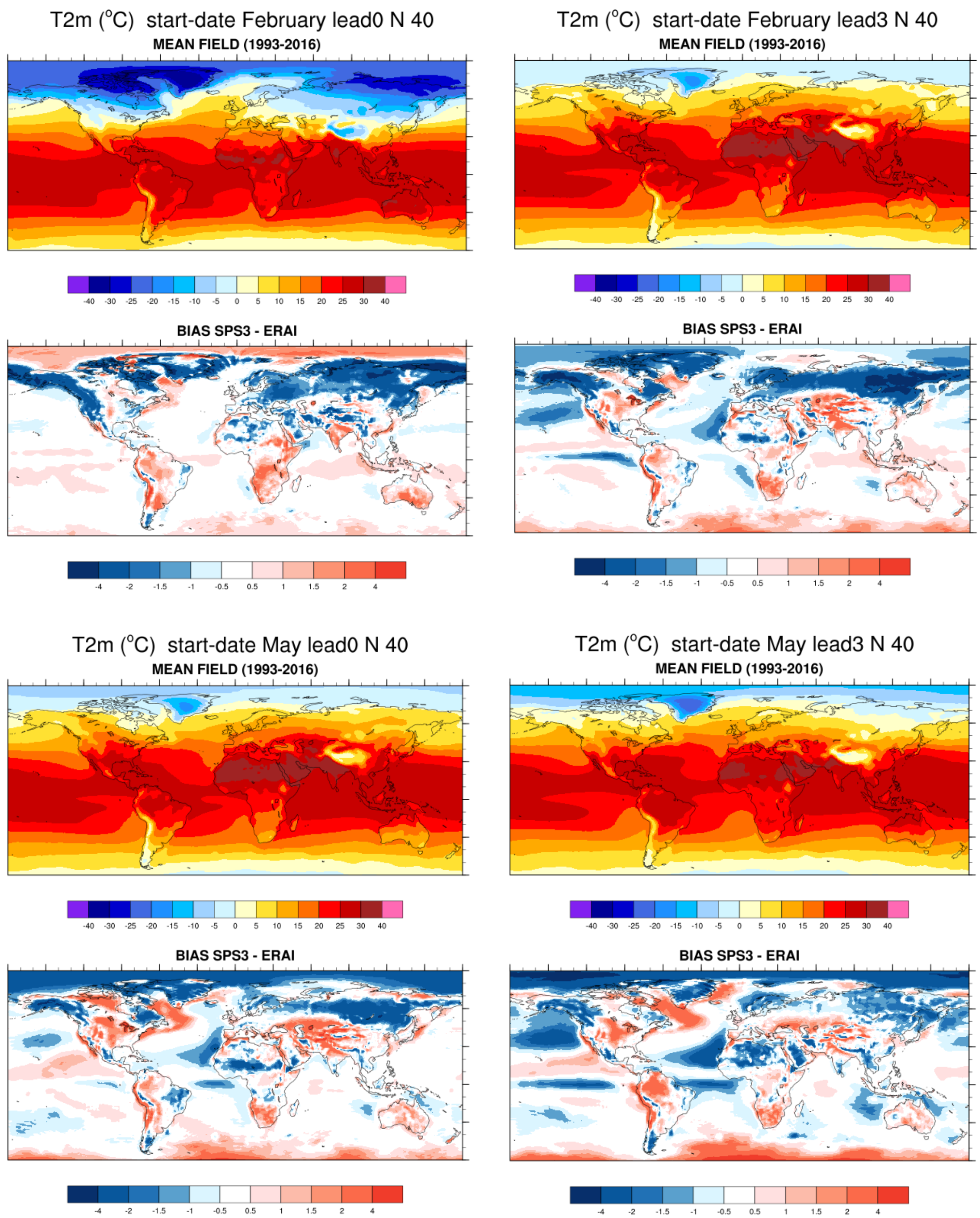

Figure 5.1. T2m three-monthly model mean and bias (from ERA Interim) for February (upper 2 panel rows) and May (lower 2 panel rows) start dates. Lead time 0 (left panels) means the first three months of integration, lead time 3 (right panels) means the second three months of integration.

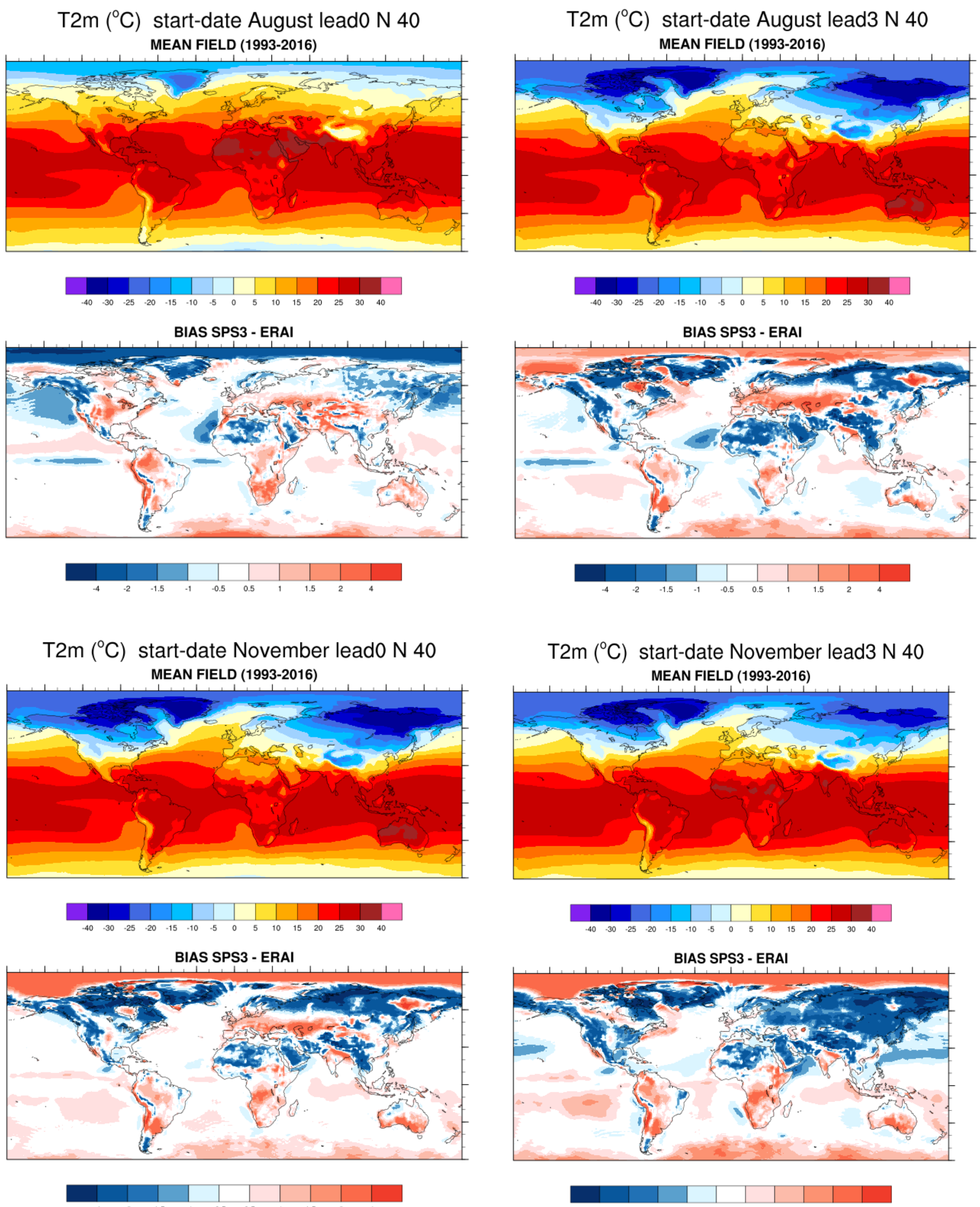

Figure 5.2 T2m three-monthly model mean and bias (from ERA Interim) for August (upper 2 panel rows) and November (lower 2 panel rows) start dates. Lead time 0 (left panels) means the first three months of integration, lead time 3 (right panels) means the second three months of integration.

5.2.2 850HPA TEMPERATURE BIAS

From Figure 5.3, it can be seen that the general behaviour of the model, as far as NH winter 850 hPa temperature is concerned, is of a slight mid-latitudinal cooling in both hemispheres and a corresponding slight warming of the higher latitudes and of the tropical regions, in particular the tropical Pacific and the South American coastal Pacific (the main El Nino region).

Cooling and warming are respectively still slowly increasing in the second three months of the forecast (up to approximately 2 °C on average). Central Western Europe, little affected by bias for all 6 months of the forecast period for the May start date, presents a moderate negative bias for the second three months of the November start date (lead 3). High mountain areas (e.g. Greenland, Himalaya, Andes and Rockies) should be disregarded since 850 hPa surface is below ground and temperature is extrapolated and therefore affected by large errors.

5.3 PRECIPITATION BIAS

Precipitation is possibly, together with T2m, the parameter most sought after by seasonal forecast users. As we did for T2m, we will concentrate on three-monthly mean fields at lead 0 and lead 3 (the first three and the second three months of the forecast integrations). Maps will again be presented for the four canonical SDs (February, May, August and November). The re-forecasts span the 24-year period from 1993 to 2016 and always refer to 40 members ensemble sets. The four Figures 5.4 to 5.7 show precipitation mean maps (CMCC-SPS3, upper), bias (CMCC-SPS3, middle with NCAR-GPCP analysis as reference, CMCC-SPS2 for comparison, with EMRAI analyses for reference, see comment later), lead 0 (left) and lead 3 (right), for all 4 SDs (Feb, May, Aug, Nov) respectively in sequence. Because of the very large influence of the seasonal cycle on precipitation, lead 0 maps of a given start date are always very similar (sometimes more similar) to lead 3 maps of the preceding start date, in addition to being similar to the lead 3 maps of the same start date.

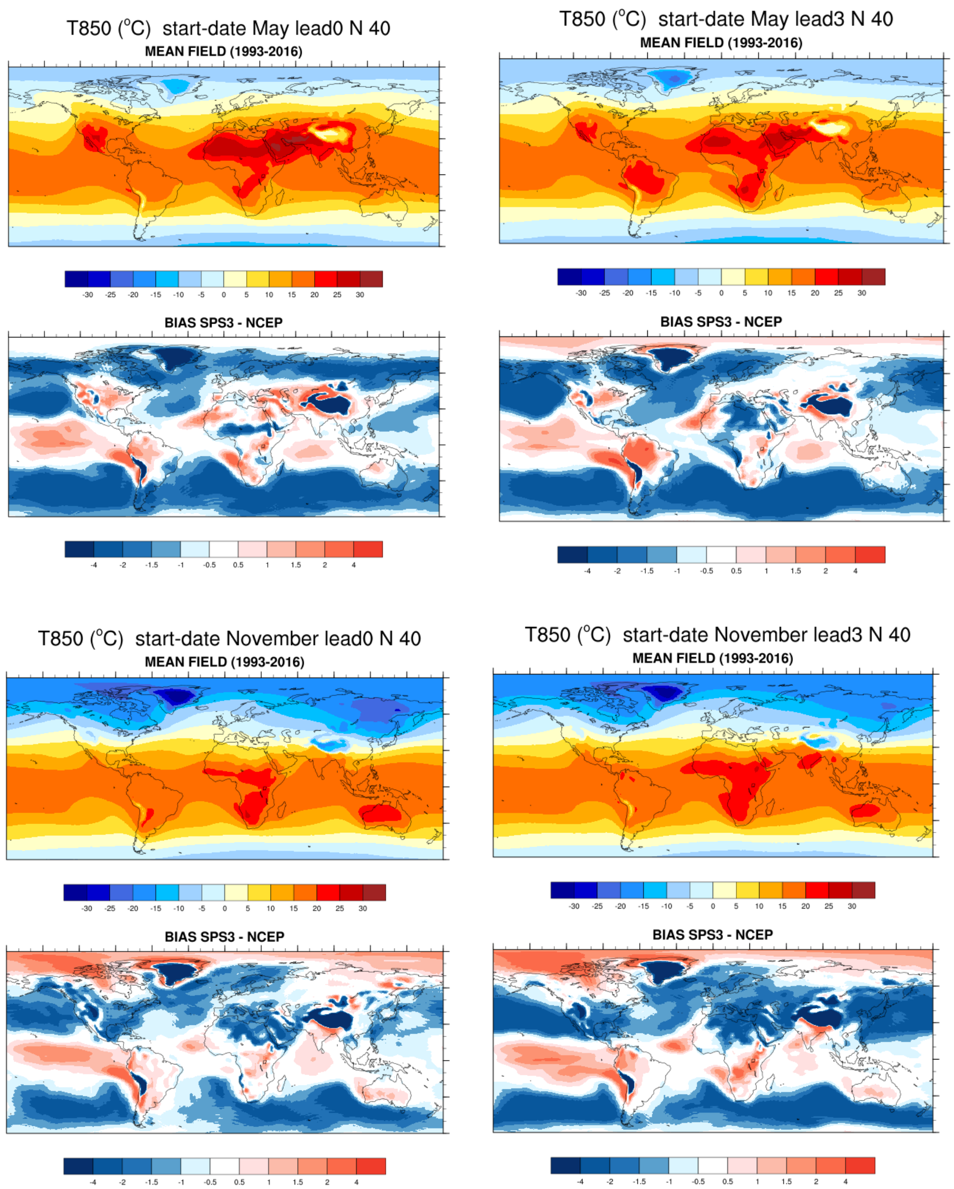

Figure 5.3 850 hPa Temperature three-monthly model mean and bias (from NCEP reanalyses) for May (top) and November (bottom) start dates. Lead time 0 (left panels) refers to the first three months of integration, lead time 3 (right panels) refers to the second three months of integration.

The main feature of the precipitation bias fields for all start dates, is a clear tendency to produce a double Intertropical Convergence Zone (ITCZ) in the Tropical Pacific, which is a systematic error common to most of the state – of the – art coupled general circulation models (CGCMs). Furthermore, errors appear to be generally larger for start dates which span mostly summer months (e.g. May), than for start dates which span mostly winter months (e.g. November).

By comparing biases of CMCC-SPS3 and of CMCC-SPS2 (middle and lower panels), unfortunately only over land, it is possible to verify that SPS3 has a much-improved precipitation bias (note, however, the change of sign of the bias over Africa and South America, possibly due to the use of NCAR–GPCP climate, which uses short-range precipitation forecasts as a proxy to compute global precipitation climate fields).

The overall amplitude and spatial structure of the SPS3 lead 0 precipitation biases are, as previously noted for temperature, highly comparable with similar seasonal prediction global coupled models (for a direct comparison, see later Sect. 9.3).

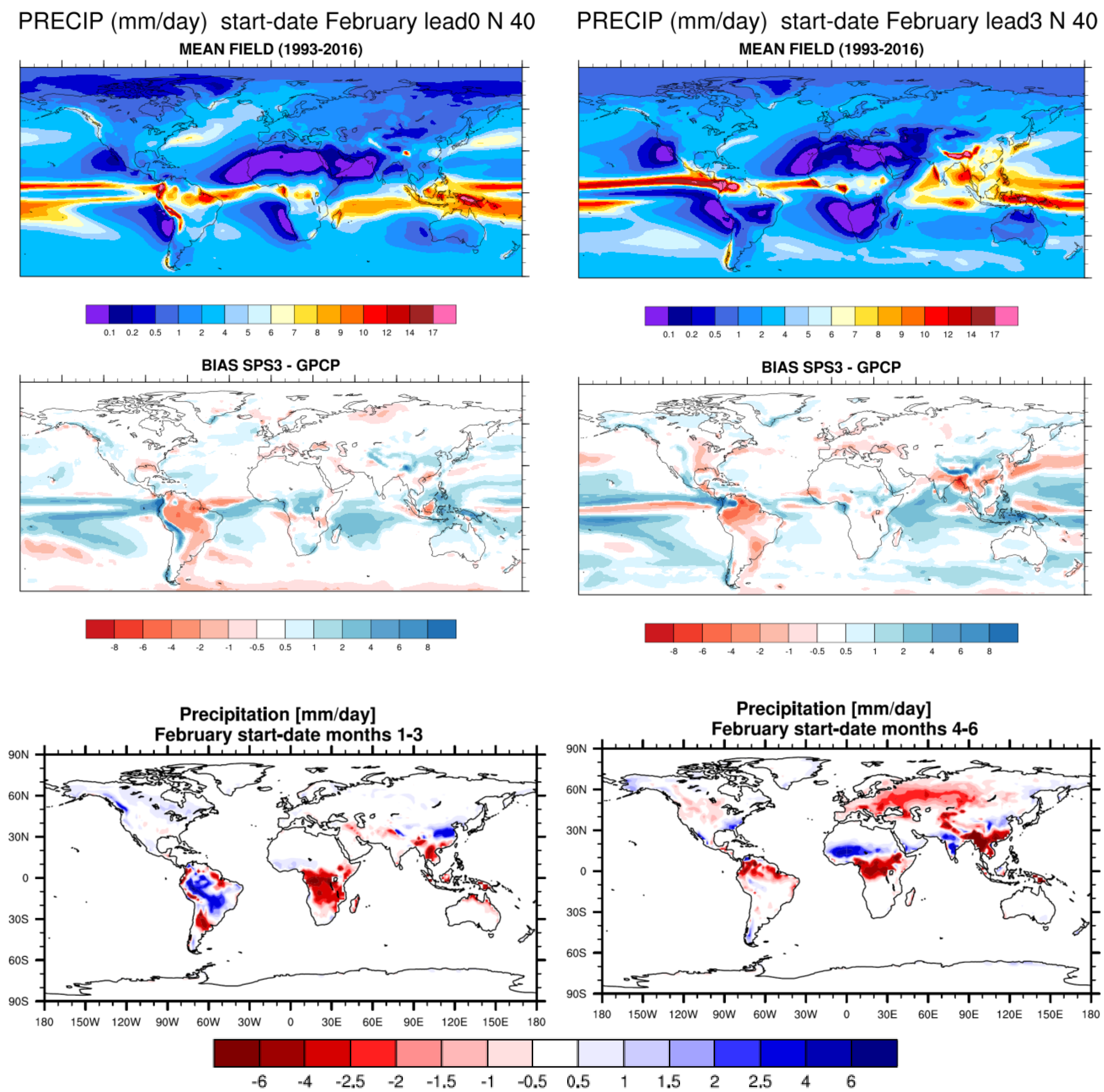

Fig 5.4 Precipitation three-monthly model mean and bias (from GPCP) for February (upper 2 panel rows) start dates. Lead time 0 (left panels) means the first three months of integration, lead time 3 (right panels) means the second three months of integration. Lower panel row: precipitation bias for the previous CMCC-SPS2 operational model, CRU analysis.

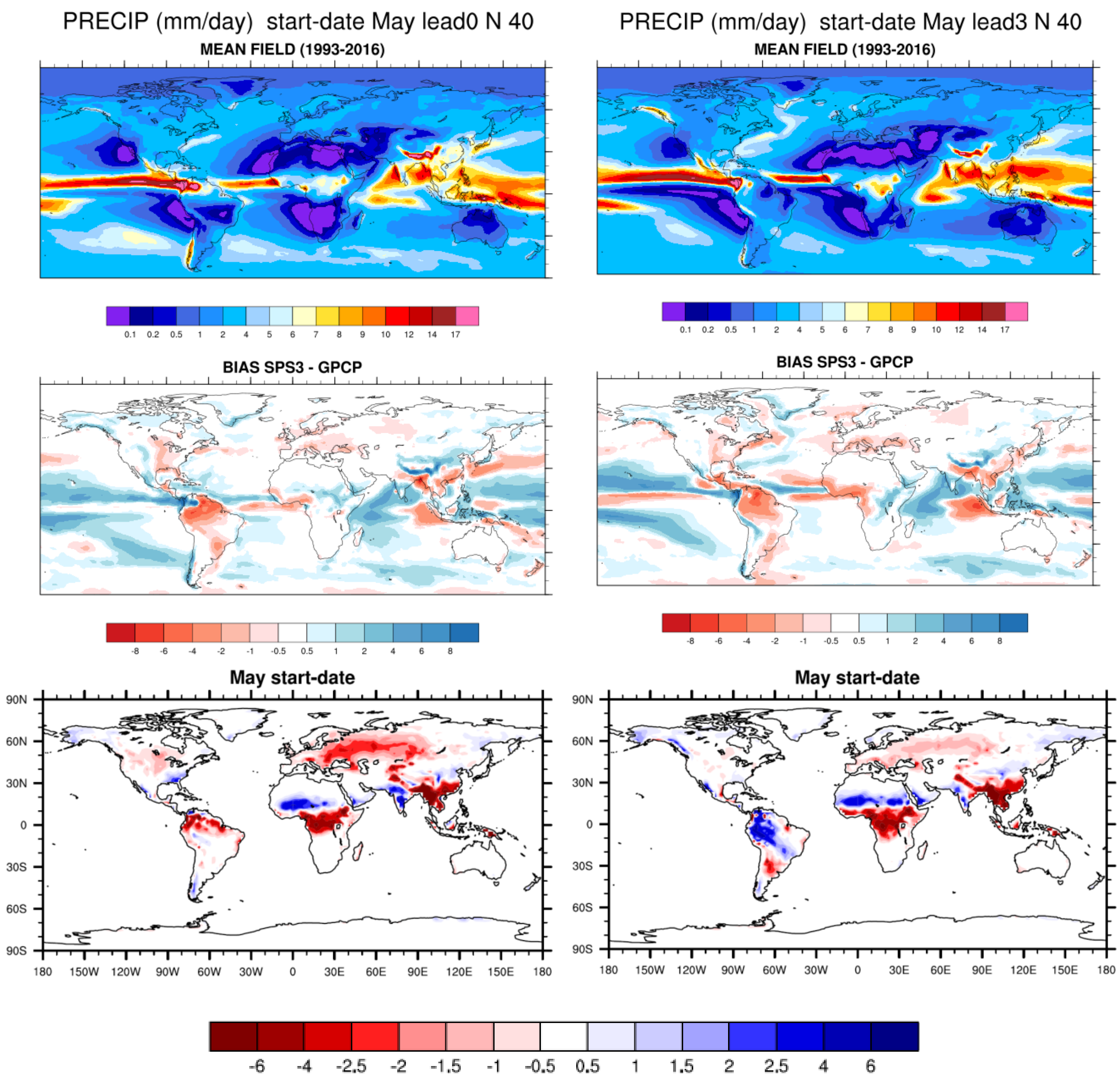

Figure 5.5 Precipitation three-monthly model mean and bias (from GPCP) for May (upper 2 panel rows) start dates. Lead time 0 (left panels) means the first three months of integration, lead time 3 (right panels) means the second three months of integration. Lower panel row: precipitation bias for the previous CMCC-SPS2 operational model.

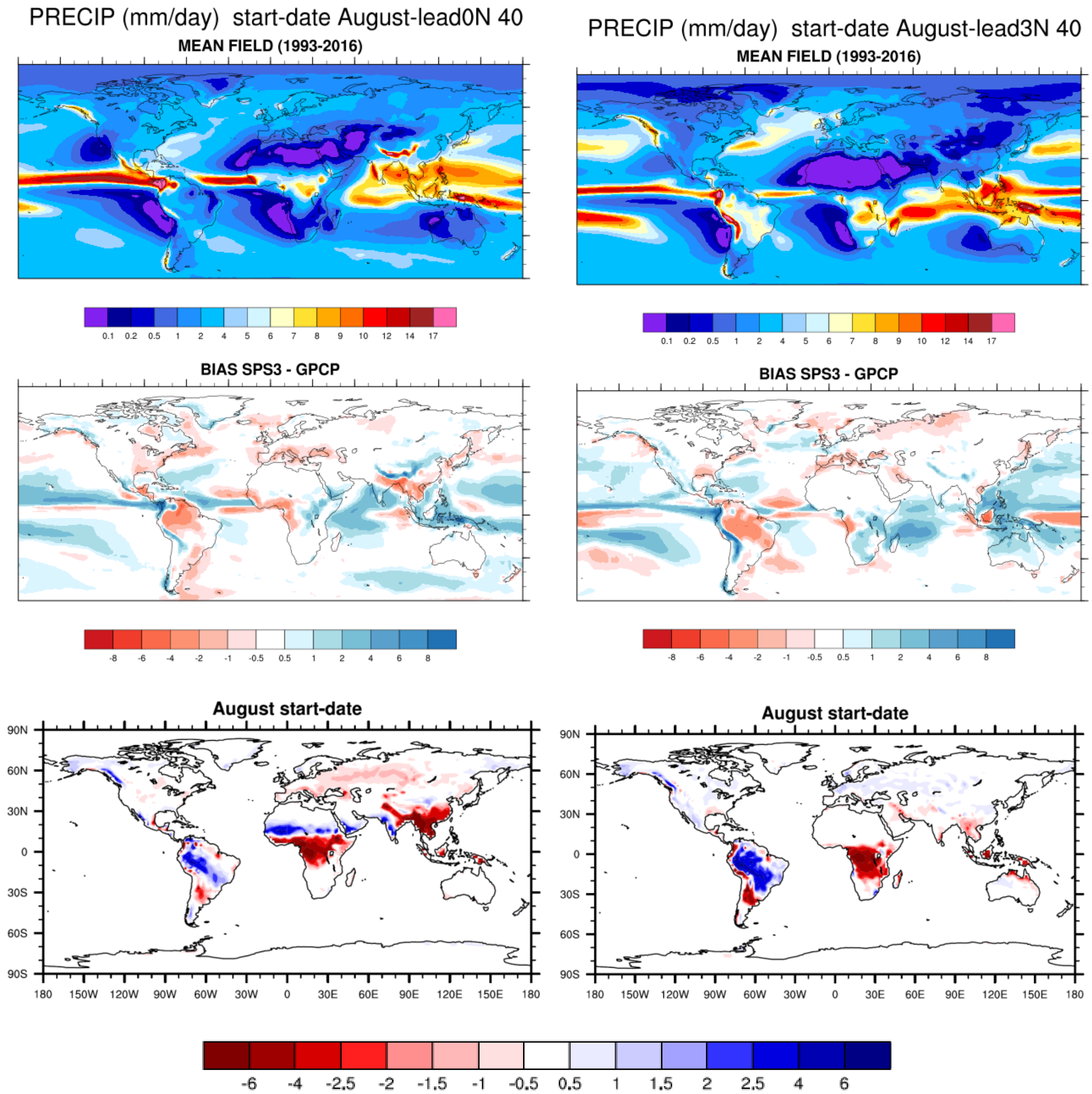

Figure 5.6 Precipitation three-monthly model mean and bias (from GPCP) for August (upper 2 panel rows) start dates. Lead time 0 (left panels) means the first three months of integration, lead time 3 (right panels) means the second three months of integration. Lower panel row: precipitation bias for the previous CMCC-SPS2 operational model.

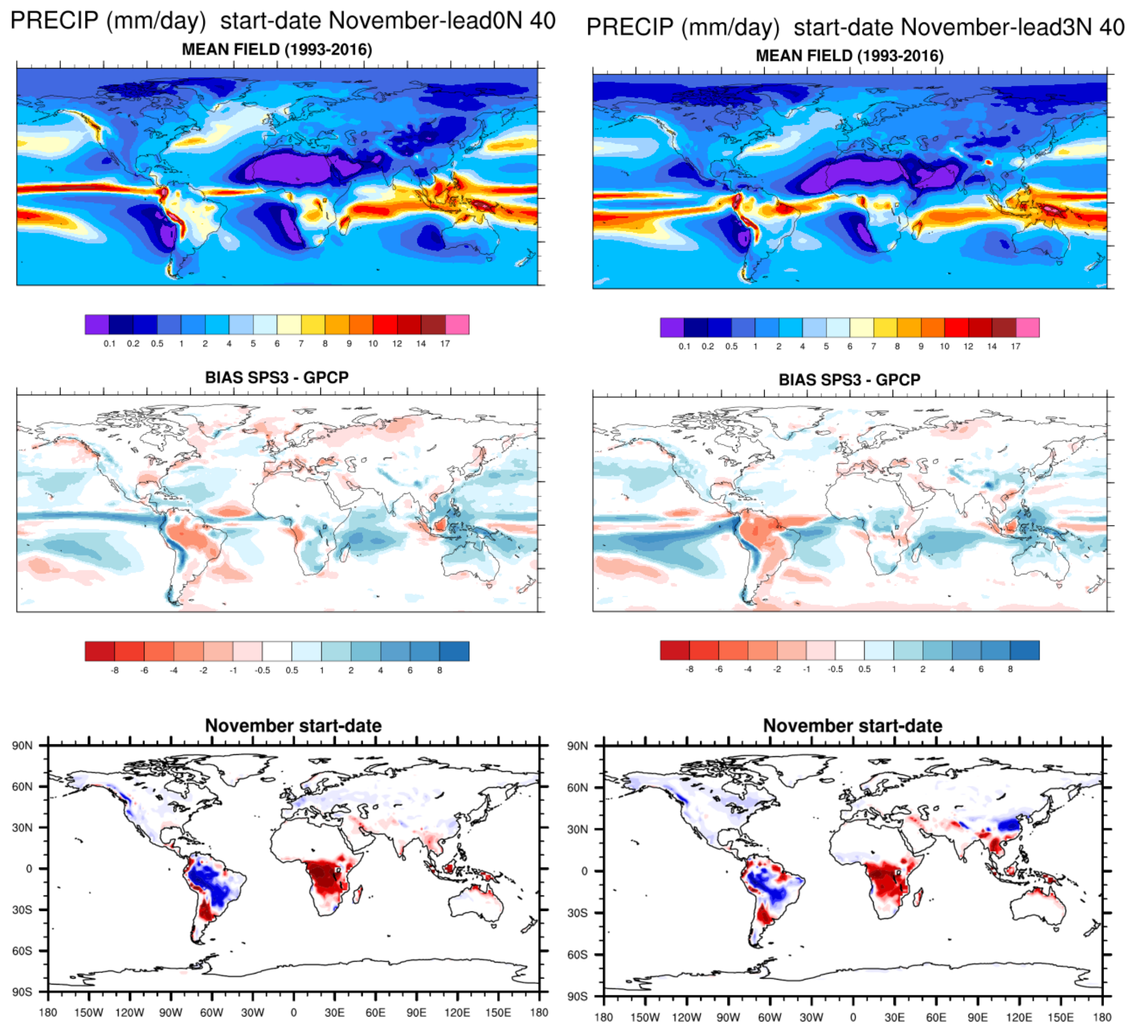

Figure 5.7 Precipitation three-monthly model mean and bias (from GPCP) for November (upper 2 panel rows) start dates. Lead time 0 (left panels) means the first three months of integration, lead time 3 (right panels) means the second three months of integration. Lower panel row: precipitation bias for the previous CMCC-SPS2 operational model.

5.4 MEAN SEA LEVEL PRESSURE AND 500 HPA GEOPOTENTIAL HEIGHT BIASES

The next four figures (5.8, 5.9, 5.10 and 5.11) show the model bias in MSLP and 500 hPa Geopotential height for all start dates, for lead 0 and 3 and for both hemispheres. We will concentrate here only on the NH maps of model bias.

The most prominent feature common (at various degrees of intensity) to all bias maps shown is the dominance of an almost equivalent baroptropic zonal wavenumber 2 structure, with high biases over the oceans and low biases over the land masses. The phase of such structures is therefore aligned west of the Greenwich meridian in the Euro-Atlantic sector and along the dateline in the Pacific sector. During winter months (e.g. start date November) errors tend to be larger around 0E and 180E and smaller at 90E and 90W, negative at higher latitudes and positive at lower, subtropical latitudes.

The character of the error is such that it is consistent with weaker planetary stationary waves and a zonalization of the westerlies, with mean mid-latitude geostrophic zonal westerly winds considerably stronger in the model than in the real atmospheric climate (an extremely common feature of practically all global coupled and atmosphere-only GCMs), possibly linked with some model misrepresentation of the thermal land-sea contrast and/or of orographic forcing (lack of low-level gravity-wave drag).

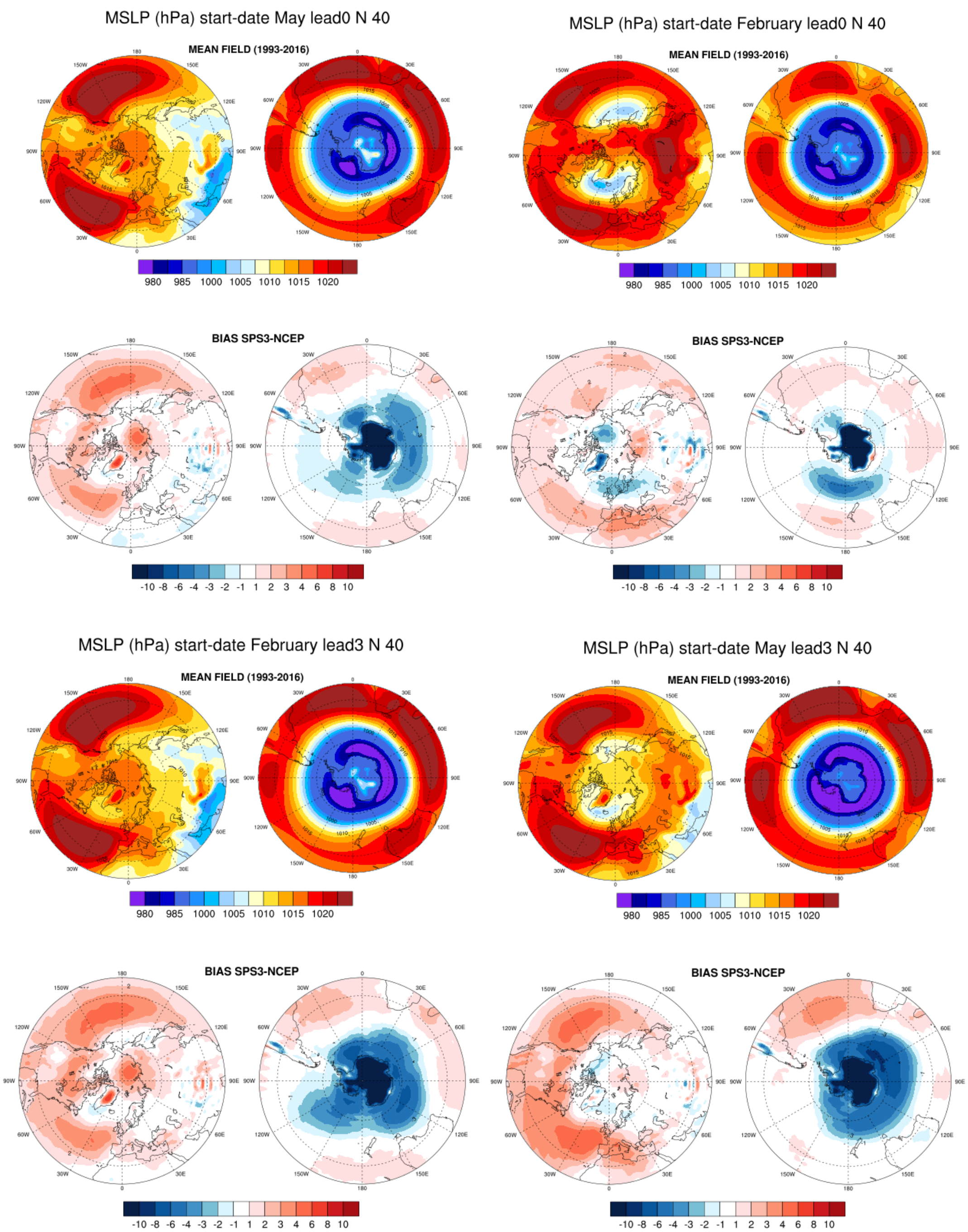

Figure 5.8 Mean Sea Level Pressure (MSLP) three-monthly model mean and bias (from NCEP reanalyses) for February (upper 2 panel rows) and May (lower 2 panel rows) start dates. Lead time 0 (left 2 panels), lead time 3 (right 2panels). Northern Hemisphere, left; Southern Hemisphere, right.

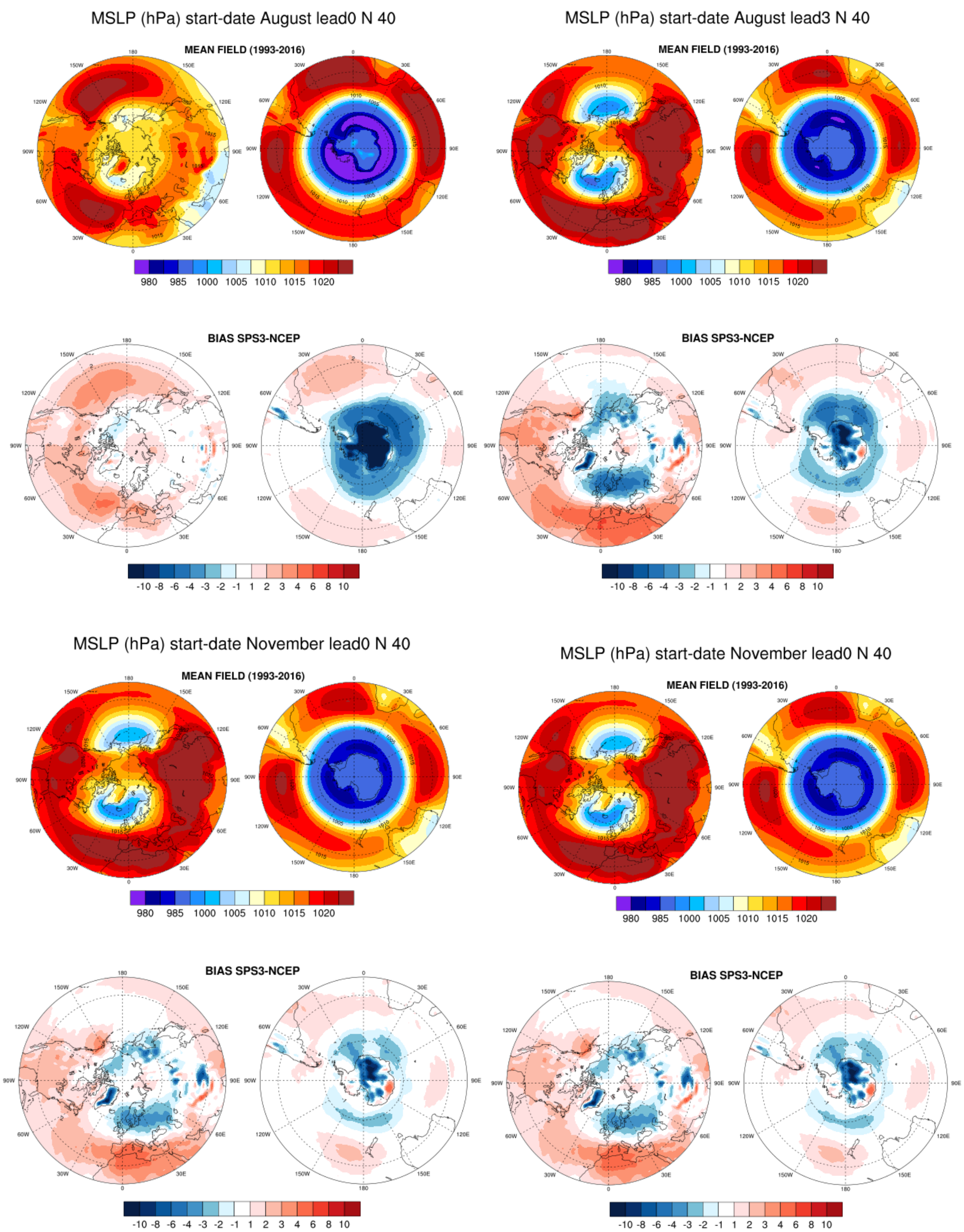

Figure 5.9 Mean Sea Level Pressure (MSLP) three-monthly model mean and bias (from NCEP reanalyses) for August (upper 2 panel rows) and November (lower 2 panel rows) start dates. Lead time 0 (left 2 panels), lead time 3 (right 2panels). Northern Hemisphere, left; Southern Hemisphere, right.

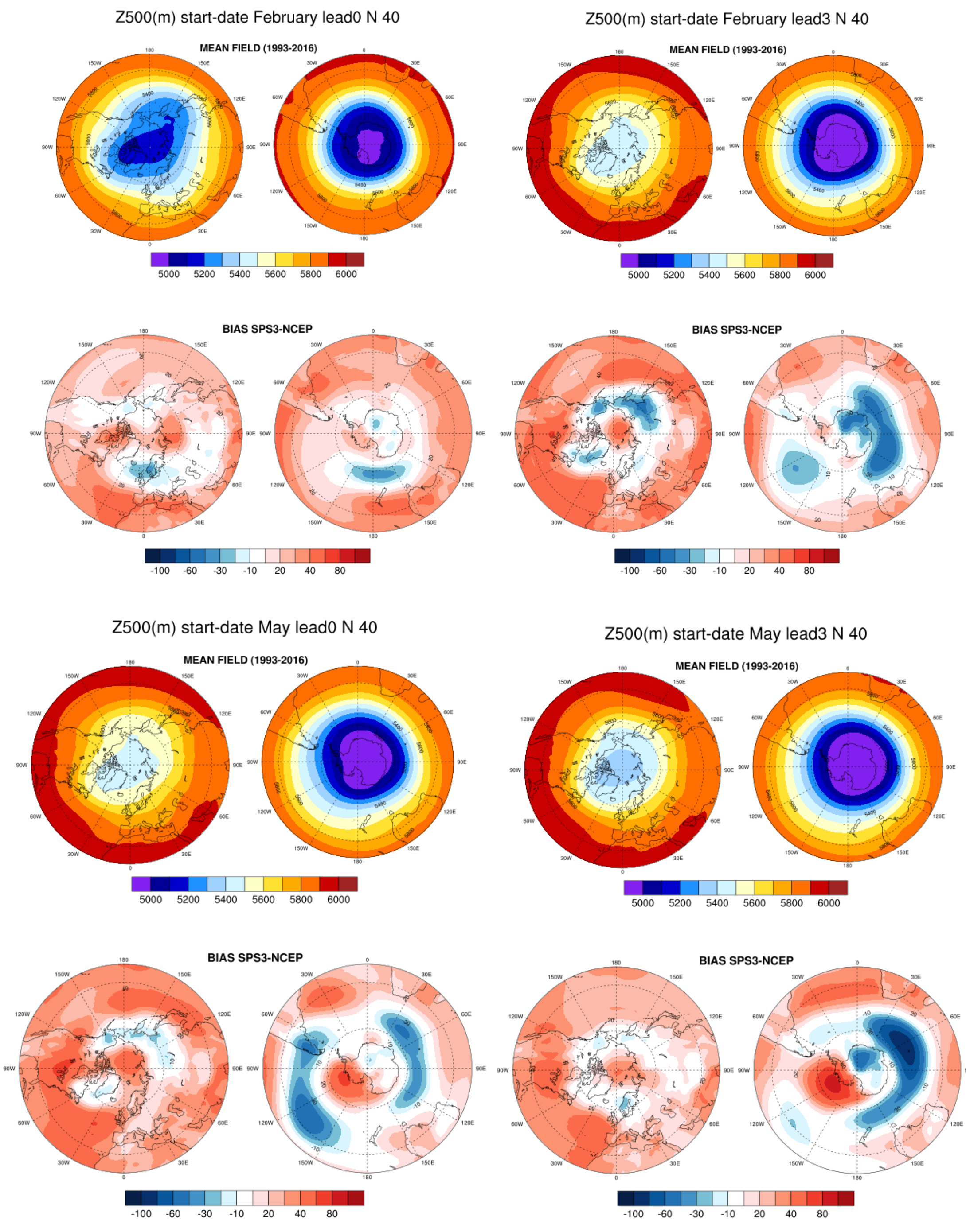

Figure 5.10. 500–hPa Geopotential Height three-monthly model mean and bias (from NCEP reanalyses) for February (upper 2 panel rows) and May (lower 2 panel rows) start dates. Lead time 0 (left 2 panels), lead time 3 (right 2panels). Northern Hemisphere, left; Southern Hemisphere, right.

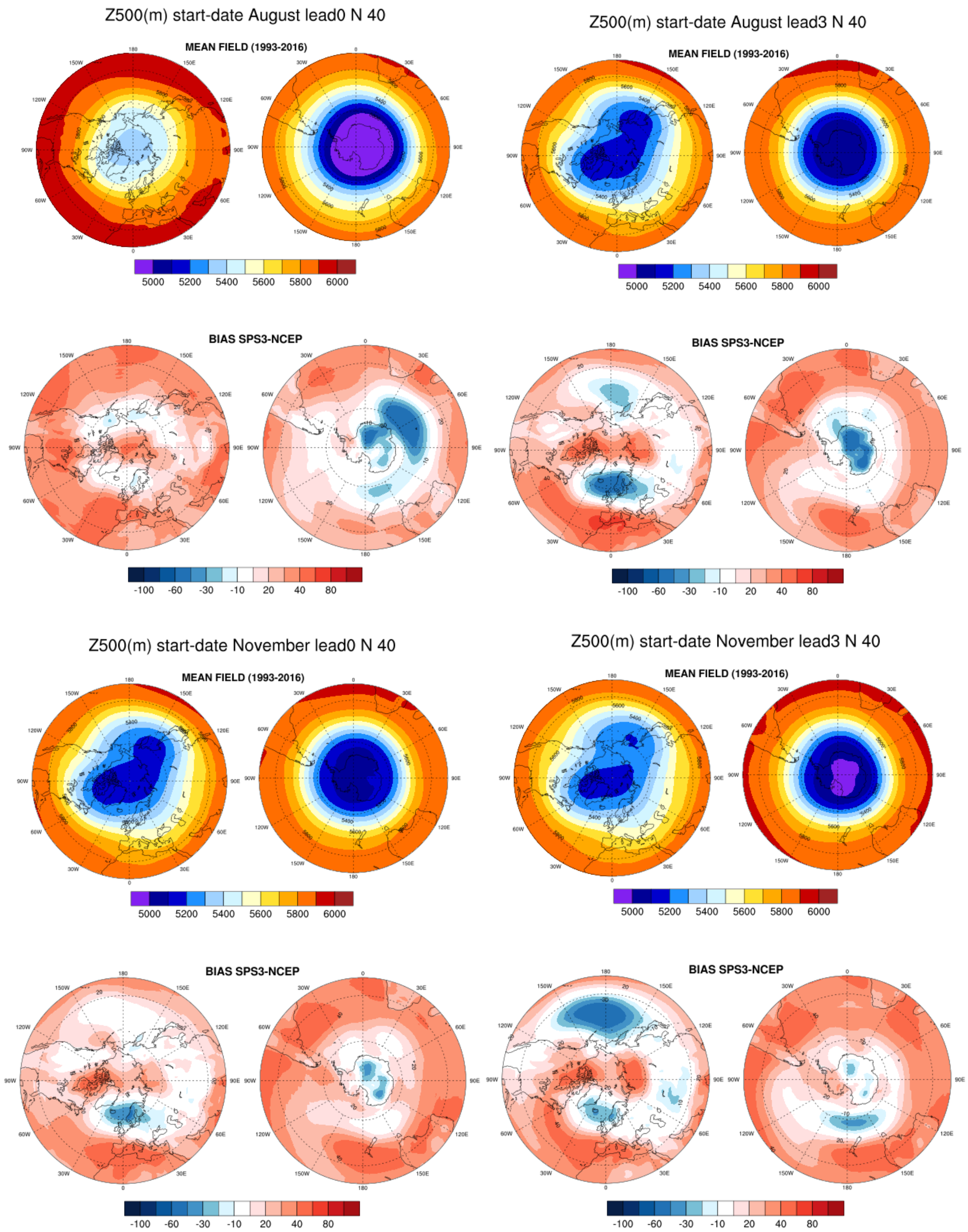

Figure 5.11 500 hPa Geopotential Height three-monthly model mean and bias (from NCEP reanalyses) for August (upper 2 panel rows) and November (lower 2 panel rows) start dates. Lead time 0 (left 2 panels), lead time 3 (right 2panels). Northern Hemisphere, left; Southern Hemisphere, right.

5.5 SEA SURFACE TEMPERATURE BIAS

The main features of the Sea Surface Temperature bias fields for all start dates are shown in Figures 5.12, 5.13, 5.14 and 5.15.

Maps are again presented for the four canonical SDs (February, May, August and November). The re-forecasts span the 24-year period from 1993 to 2016 and always refer to 40 members ensemble sets. The four Figures 5.12 to 5.15 show CMCC-SPS3 mean SST maps (upper panels), SST bias (from ERAI re-analyses, middle panels) and CMCC-SPS2 bias for comparison (lower panels), lead 0 (left) and lead 3 (right), for all 4 SDs (Feb, May, Aug, Nov) respectively in sequence. As it was the case for precipitation fields, because of the very large influence of the seasonal cycle on SSTs, lead 0 maps of a given start date are always fairly similar to lead 3 maps of the preceding start date, often more similar then they are to the lead 3 maps of the same start date, as they should be if the bias was increasing linearly.

Again, as for precipitation, SST bias maps for all start dates bear the signature of a clear tendency to produce a double Intertropical Convergence Zone (ITCZ) in the Tropical Pacific, which is a systematic error common to most of the state-of-the-art coupled general circulation models (CGCMs). Furthermore, errors appear to be generally larger for start dates which span mostly autumn months (e.g. August at lead 1 and May at lead 3), and smaller for the lead 0 February start date, which spans mostly spring months.

SST values between -0.5°C and 0.5°C have been masked, hence most ocean surface looks white in the plot. In general, Northern Hemisphere coastal sea areas appear warmer than in ERAI reanalysis, in particular at mid and high latitudes. Kuroshio current and Gulf Stream temperatures are overestimated, as well as Mediterranean coastal temperatures. The three, main coastal upwelling regions (California and Baja California, western South America and west southern Africa) are also warmer than reanalysis, but the rather high ocean resolution produces smaller biases compared to the SPS2 system (Figure 5.12 to 5.15, lower panels). The main cold bias is noticeable in the equatorial Pacific, in particular in the NINO3 and NINO3.4 regions where the error is of 1.5°C-2°C magnitude. Cold biases are also evident in sub-tropical eastern Atlantic, whose cold temperatures spread through northwestern Africa and the Portuguese coast and northern Pacific.

The November forecast biases shown in Figure 5.15 (middle panels) display a warmer ocean in the Southern Hemisphere and the Tropical oceans, and a colder ocean in the Northern Hemisphere. The Kuroshio current is here colder than in reanalysis, while the Gulf Stream is still warmer but the bias magnitude is mitigated. The Mediterranean Sea and most northern Indian Ocean are affected by negative SST bias, while tropical Indian, Atlantic and the ENSO region show positive anomalies.

By comparing biases of CMCC-SPS3 and of CMCC-SPS2 (middle and lower panels respectively), it is possible to verify that SPS3 presents a somewhat reduced SST bias.

The overall amplitude and spatial structure of the SPS3 lead 0 SST biases are, as previously noted for temperature and precipitation, highly comparable biases of similar seasonal prediction global coupled models (for a direct comparison, see later Sect. 9.3).

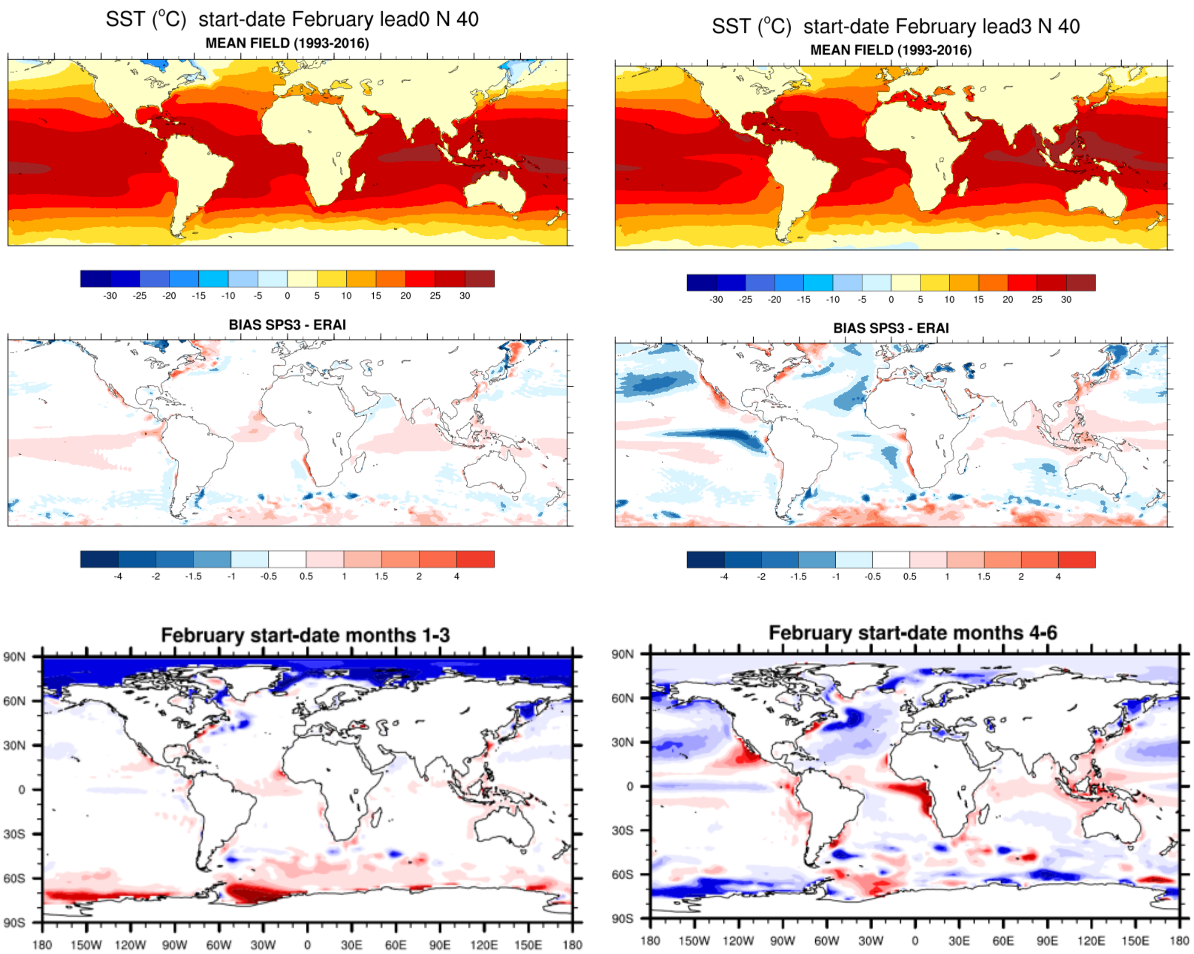

Figure 5.12 Sea Surface Temperature (SST) three-monthly model mean and bias (from ERA Interim) for February (upper 2 panel rows) start dates. Lead time 0 (left panels) means the first three months of integration, lead time 3 (right panels) means the second three months of integration. Lower panel row: precipitation bias the for previous CMCC-SPS2 operational model.

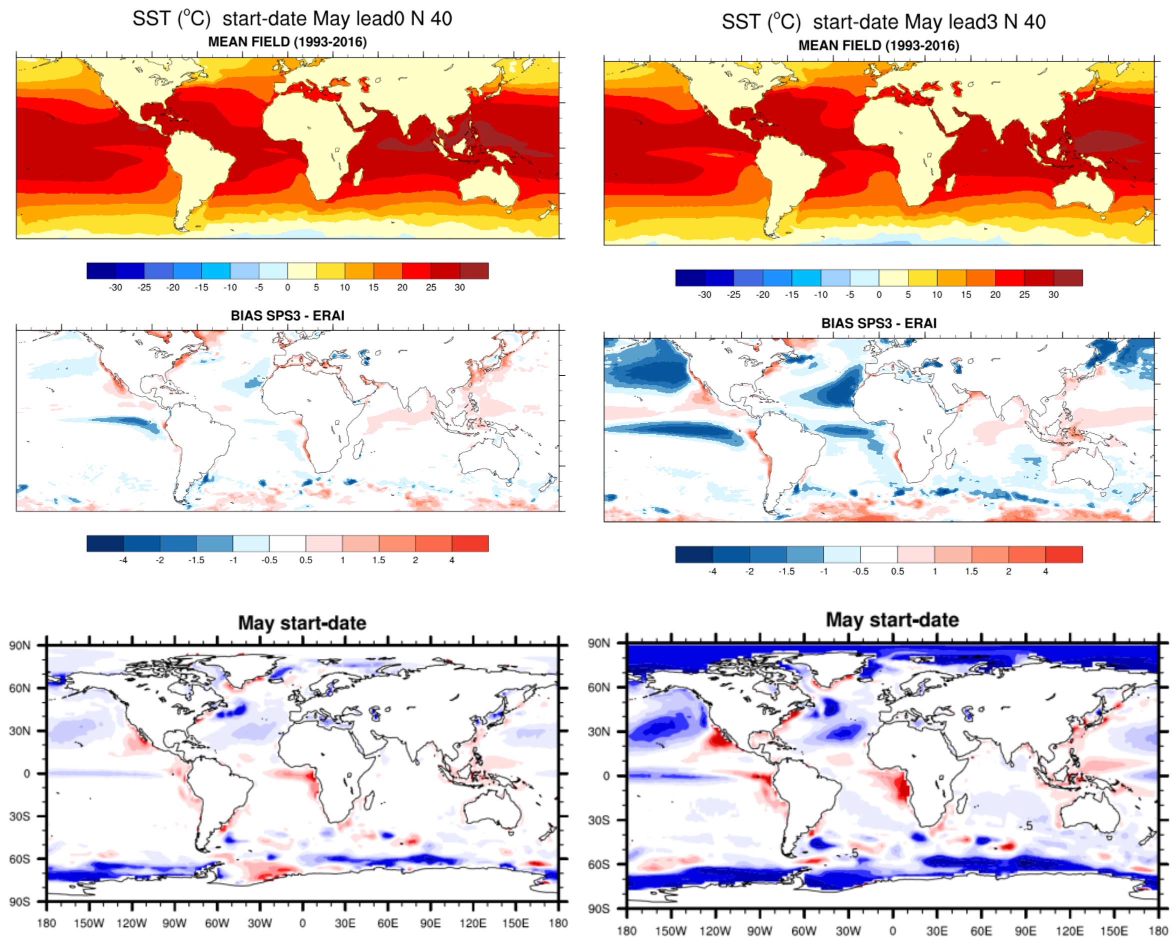

Figure 5.13 Sea Surface Temperature (SST) three-monthly model mean and bias (from ERA Interim) for May (upper 2 panel rows) start dates. Lead time 0 (left panels) means the first three months of integration, lead time 3 (right panels) means the second three months of integration. Lower panel row: precipitation bias for the previous CMCC-SPS2 operational model.

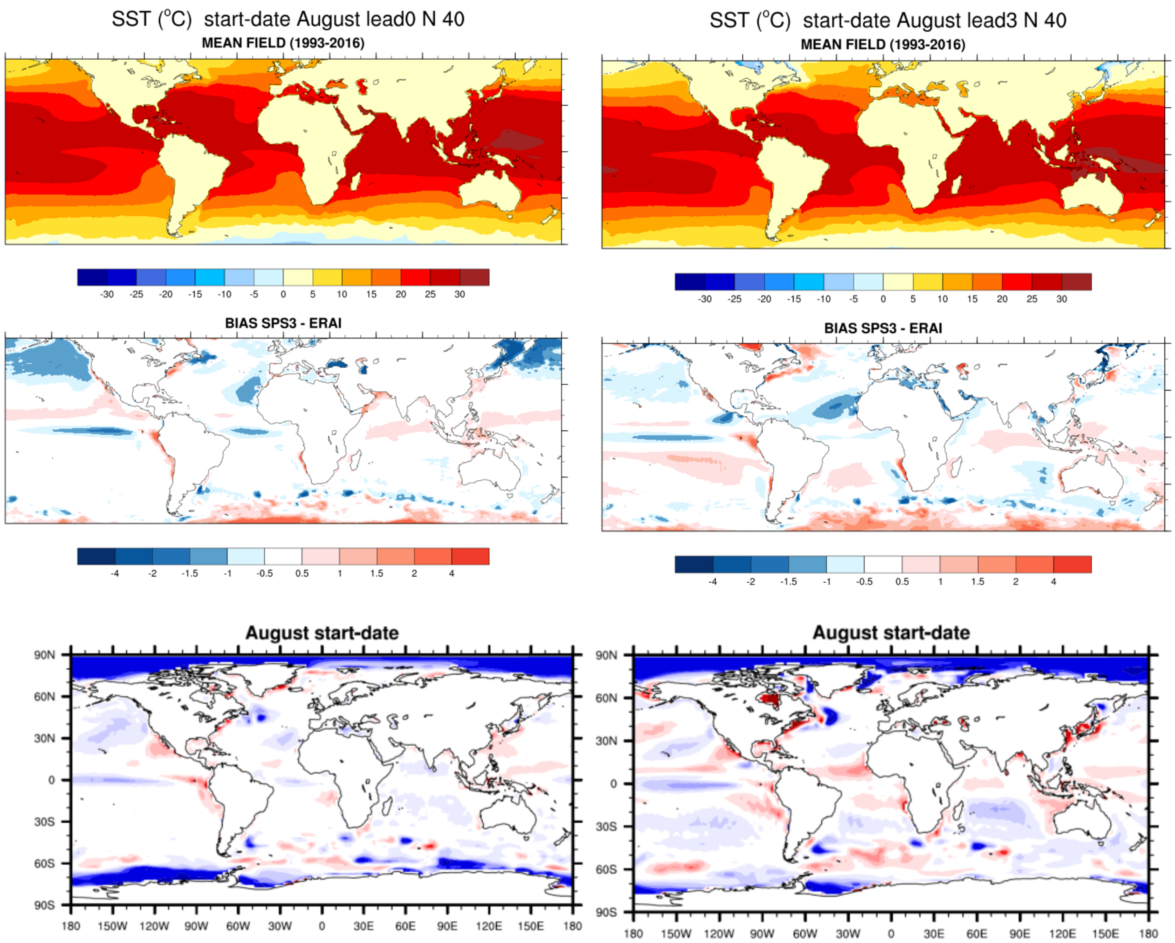

Figure 5.14 Sea Surface Temperature (SST) three-monthly model mean and bias (from ERA Interim) for August (upper 2 panel rows) start dates. Lead time 0 (left panels) means the first three months of integration, lead time 3 (right panels) means the second three months of integration. Lower panel row: precipitation bias for the previous CMCC-SPS2 operational model.

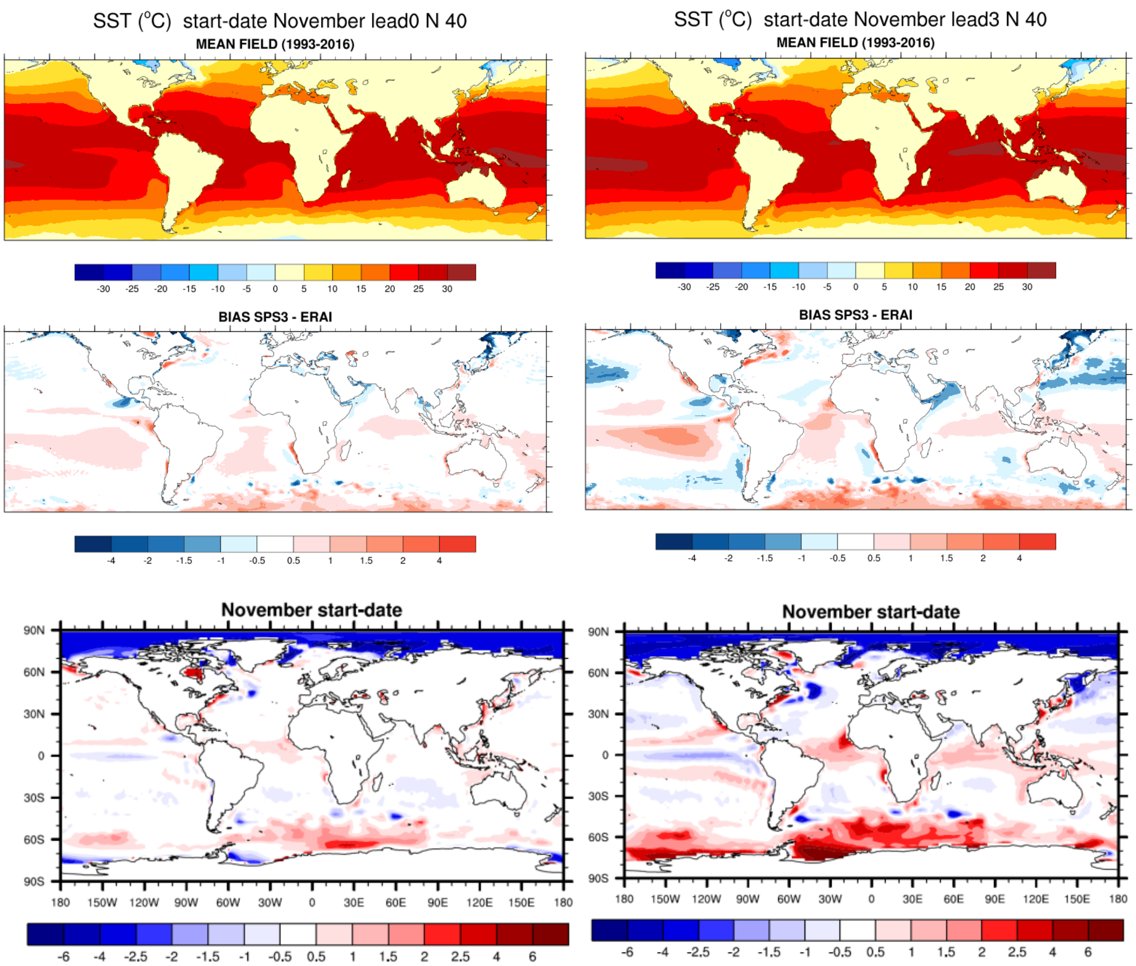

Figure 5.15 Sea Surface Temperature (SST) three-monthly model mean and bias (from ERA Interim) for November (upper 2 panel rows) start dates. Lead time 0 (left panels) means the first three months of integration, lead time 3 (right panels) means the second three months of integration. Lower panel row: precipitation bias for the previous CMCC-SPS2 operational model.

5.6 NH ATMOSPHERIC BLOCKING CLIMATOLOGY

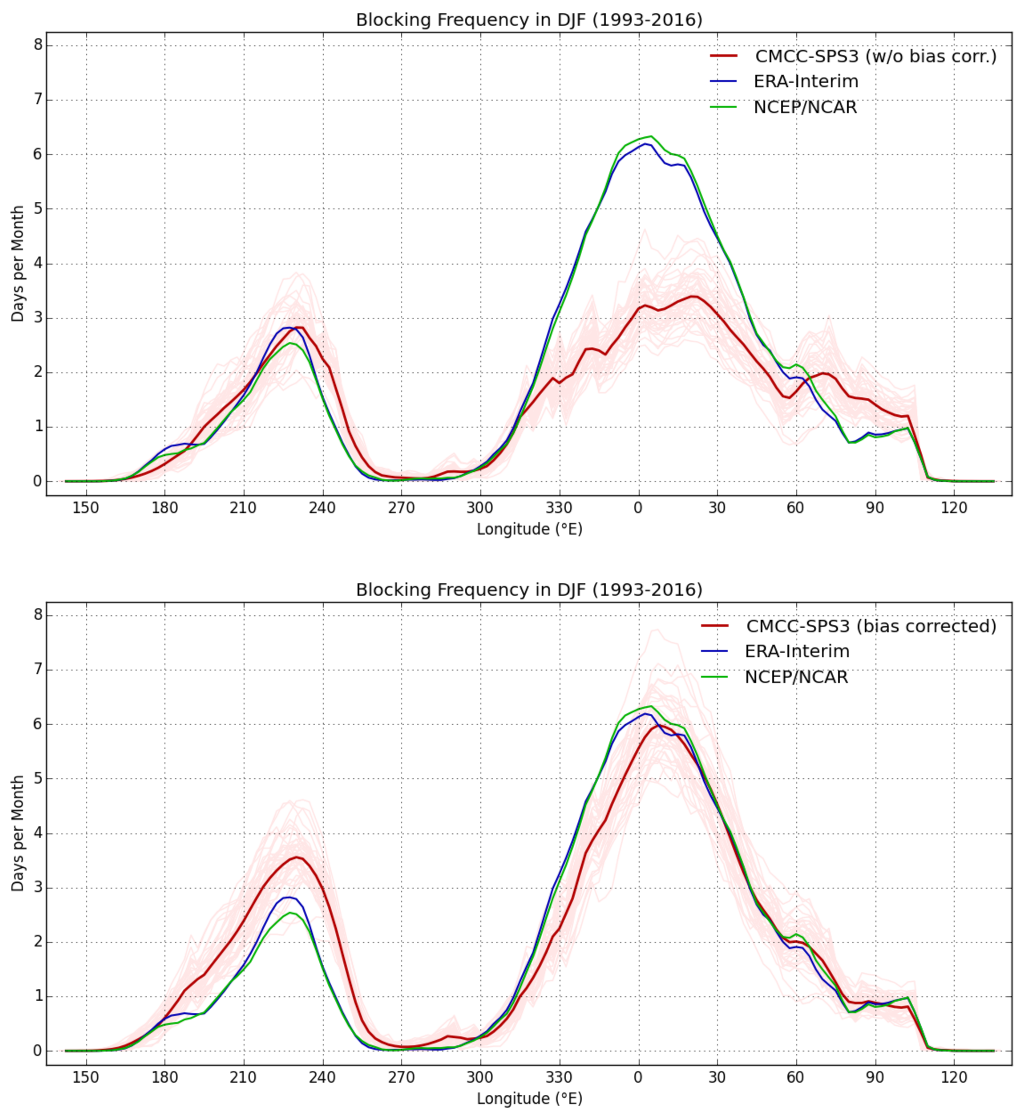

Figure. 5.16 Winter (DJF) climatologies of blocking frequency along the CBL (Central Bolocking Latitude), defined in Athanasiadis et al (2014) for CMCC-SPS3 and the ERA-Interim and NCEP/NCAR reanalyses (1993–2016). Model climatologies are shown for each individual ensemble member (light-red lines). The ensemble-mean climatology (red line) is computed as the average of the individual-member climatologies. Upper panel: Blocking index computed on direct model Z500 daily mean fields. Lower panel: The same but after a standard bias correction of the Z500 daily mean fields has been applied to the CMCC-SPS3 using ERA-Interim reanalyses.

Blocking is an important phenomenon affecting strongly the extratropical atmospheric circulation, weather and climate. The representation of blocking in numerical prediction models of all time ranges, from medium-range weather forecasts to climate projections, is beyond doubt crucial for the realistic representation of persistent weather regimes and of weather and climate extremes affecting large areas of the globe. Given the direct relationship between blocking, jet stream variability and extratropical teleconnections [Woollings et al. 2008; Athanasiadis et al. 2010; Davini et al. 2012; Masato et al. 2012], which represent different facets of the extratropical low-frequency variability, the successful representation of blocking is particularly important also in seasonal forecasting. Here a standard diagnostic is used for the Northern Hemisphere blocking.

Daily mean fields of Z500 are used covering the winter period (DJF) from 12/1993 to 02/2017. For CMCC-SPS3, these fields are derived from the hindcasts initialized in November. Prior to further processing, all fields have been interpolated to a common regular 2.5°x2.5° grid. Also, the mean bias (difference of the respective smoothed daily climatologies) has been subtracted from the daily Z500 fields as in Scaife et al. (2010). For the detection of blocking, the one-dimensional approach introduced by Tibaldi and Molteni (1990) is adopted, with the difference that here the central blocking latitude (CBL) is allowed to vary with longitude. The CBL follows the zone of maximum baroclinic activity, as in Athanasiadis et al. 2014.

The capability of the CMCC-SPS3 to reproduce the observed Northern Hemisphere climatological blocking frequency is assessed. The resulting profiles of wintertime blocking frequency are shown in Figure 5.16. At a first glance, one would say that the agreement between CMCC-SPS3 and the two reanalyses (ERA-Interim, NCEP/NCAR) is quite good, though significant departures can be seen in the domains where blocking is most frequent. Moreover, although mean bias correction much improves the model statistics for blocking, the actual low-frequency variability and the weather associated to blocking remain unaltered in the model. Reducing mean biases in the model itself can however improve significantly the representation of other dynamically linked processes.

6. SEASONAL PREDICTION SKILL SCORES

Each re-forecast consists of a six-month integration from the beginning of the month, evaluated as a deviation from the model's own climatology (model anomaly). It is then compared to the reanalysis anomaly for the corresponding time-frame. The operation is repeated for all start dates to obtain a good statistical basis for the evaluation of model accuracy, skill, reliability, discrimination, etc.

For the sake of conciseness, the scores shown in this Section are limited to RMS errors, Anomaly Correlations and ROC scores computed on 2m Temperature and Precipitation fields.

El Niño, PNA and NAO specific forecast scores are shown and commented respectively in Sects. 7 and 8.

6.1 RMS ERRORS

Figure 6.1 shows RMSE of T2m for all four start dates (top to bottom, Feb. to Nov.) for lead month 0 (left) and 3 (right). The largest errors are evident for NH winter and spring months, practically irrespective of the lead month (0 or 3) and affect the middle latitudes and (more intensely) the high latitudes of the Northern Hemisphere. Land and ice-covered areas are much more affected than sea areas and North America and Asia more than Western Europe. Errors for summer and autumn months remain of the order of 2 °C, while in winter and spring they can reach 3 to 4 °C. A problem spot with errors larger than 5 °C is evident in winter and spring months in the Baffin Bay, between Greenland and Canada, consistently with the fairly large bias of T2m in similar seasons shown in Figures 5.1 and 5.2. These errors can be most likely due to problems with the SSTs and with sea-ice, although a comparison with SST bias maps (Figures 5.12-5.15) is made somewhat difficult due to different map plotting latitude limits.

Figure 6.2 shows a comparison between RMSE of T2m for CMCC-SPS3 and for SPS2, for all four start dates but for lead month 1 only. Some improvements are evident, although the main character of the error fields has remained the same, including the Baffin Bay winter months problem.

The RMS errors of precipitation rate (Figure 6.3) shows global errors larger in winter and spring seasons (almost irrespective of lead month) in the tropical Pacific and Indian oceans, with spot maxima larger than 4 mm/day only for tropical Pacific and Indian oceans and for lead month 0. Noticeable is the large area of errors above 2 mm/day in the SH central Pacific, from the Tropics up to approximately 40°S.

6.1.1 RMS ERROR OF 2M TEMPERATURE

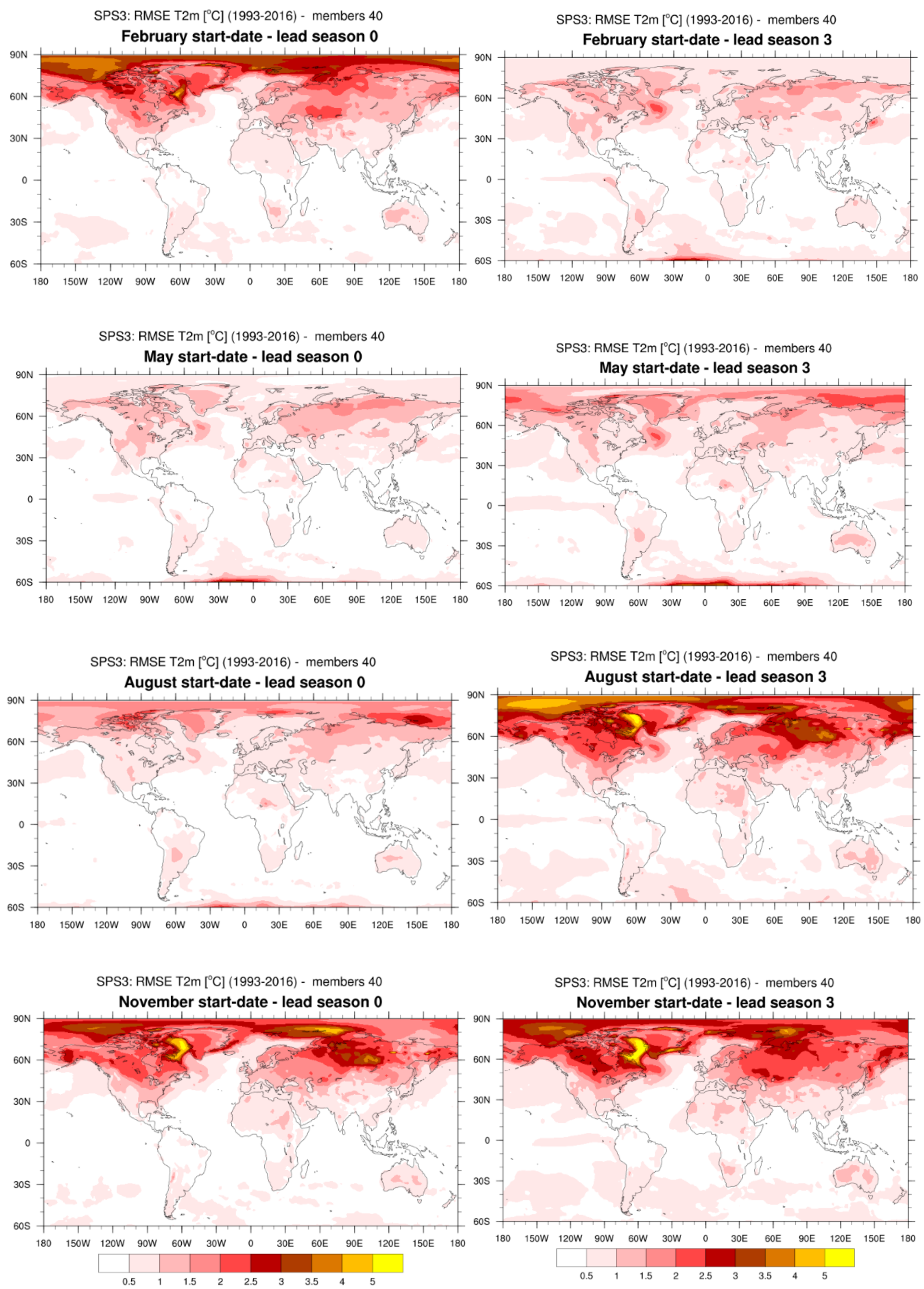

Figure 6.1 Root Mean Square Error (RMSE) for three-monthly mean T2m, all 4 start dates; lead month 0, left panels; lead month 3, right panels.

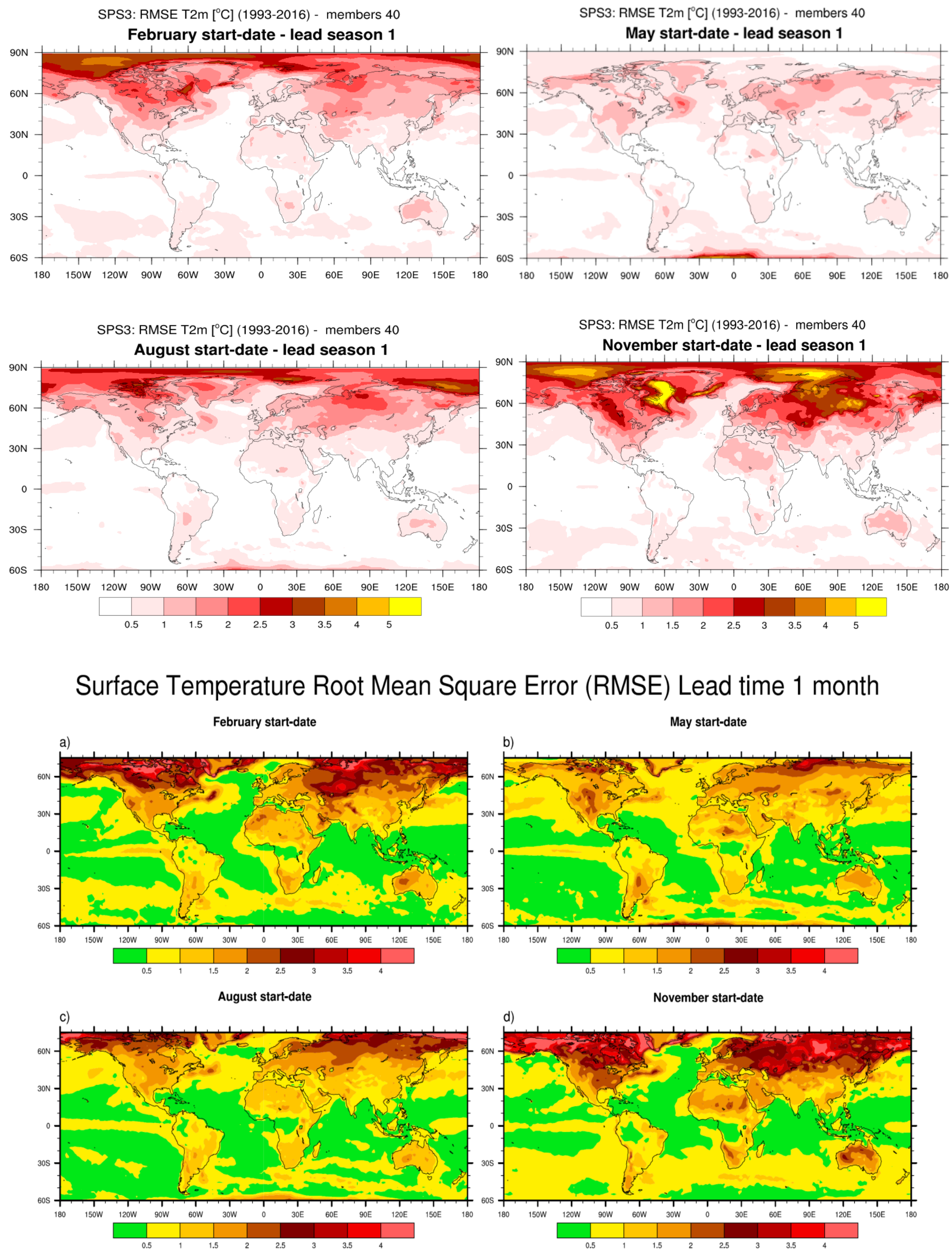

Figure 6.2 Root Mean Square Error (RMSE) for three-monthly mean T2m, all 4 start dates; lead month 1 (integrations months 2, 3 and 4; upper 4 panels) compared with the same errors of the previous CMCC-SPS2 model (lower 4 panels).

6.1.2 RMS ERROR OF PRECIPITATION

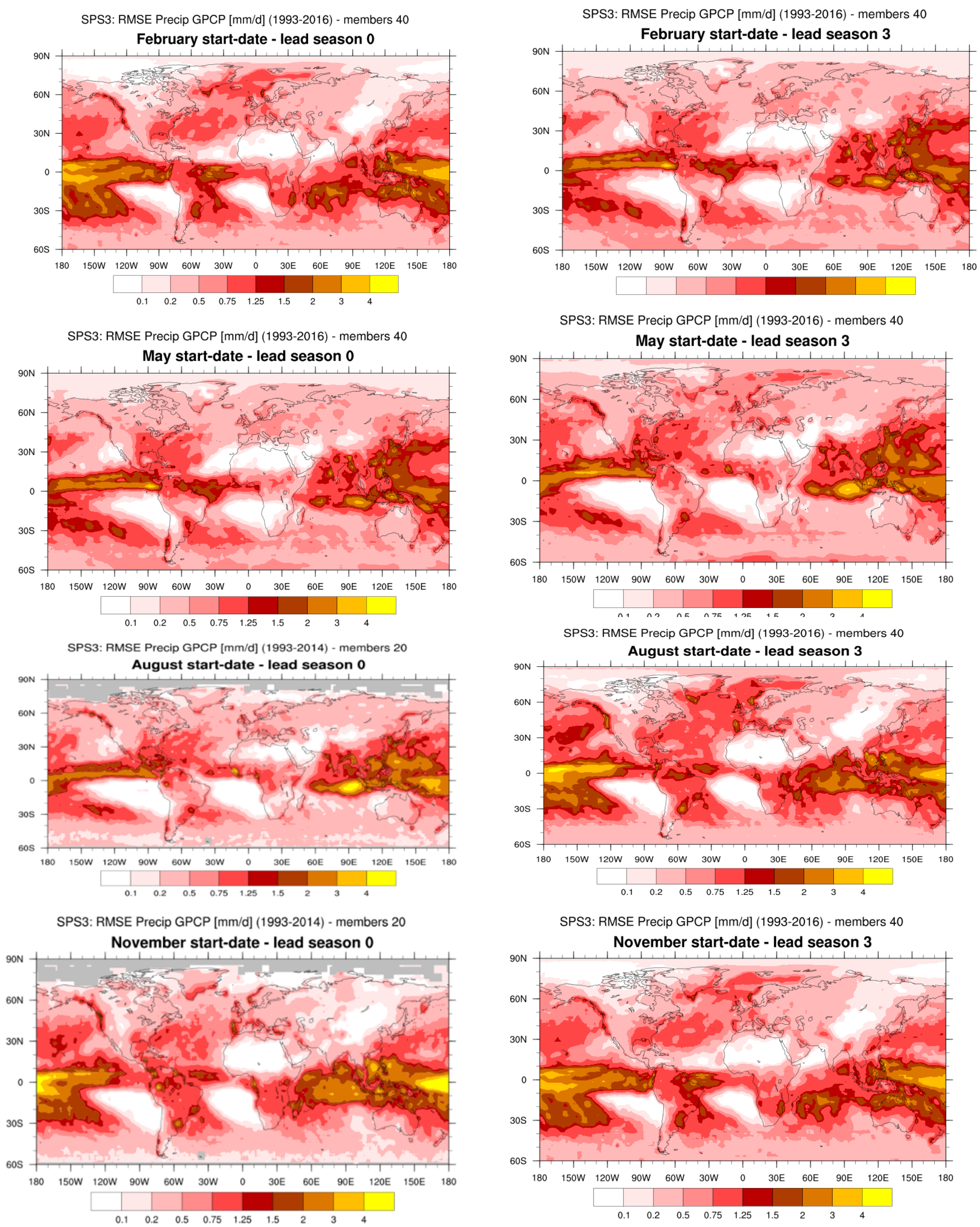

Figure 6.3 Root Mean Square Error (RMSE) for three-monthly mean Precipitation, all 4 start dates; lead month 0, left panels; lead month 3, right panels.

6.2 ANOMALY CORRELATIONS

Figure 6.4 shows Anomaly Correlation Coefficient of T2m for all four start dates (top to bottom, Feb. to Nov.) for lead month 0 (left) and 3 (right). The largest correlation values, contrary to RMSE, take place for lead month 0, with little dependency upon season (start date). Winter and spring seasons, however, score a little bit better. Geographical areas where skill is higher are evidently intertropical oceanic areas, extending also to the midlatitudes of both Pacific (more) and Atlantic (to a lesser degree) oceanic areas. Large portions of the Northern Hemisphere (mostly continental areas, but also the more northern latitudes of the Atlantic Ocean and Greenland) show very low correlation values (up to zero) for lead month 3. The problem spot with very low skill (large forecast errors) in the Baffin Bay, between Greenland and Canada, is again present, as it was for RMSE. Again, some problems with the SSTs and with sea-ice, are probably to be held responsible.

Figure 6.5 shows a comparison between ACC of T2m of CMCC-SPS3 and SPS2 for all four start dates but for lead month 1 only. Some improvements are evident, although the main characters of the correlation fields have remained the same.

The Anomaly Correlation Coefficient maps for precipitation rate (Figure 6.6) show global skill smaller for lead month 3 than for lead month 0, fairly irrespective of season (start date), with the exception of lead 3, August start date (and, to a lesser extent, also May start date), which shows good tropical ocean correlations even at the later lead time. Correlations are very large (around 1) in large portions of the tropical Pacific and Indian oceans, but appear to extend to higher latitudes of all oceanic areas, mostly for lead month 0. Some lower correlations appear in the SH central Pacific, from the Tropics up to approximately 40°S, as it was even more evident in RMSE maps for precipitation shown previously.

6.2.1 ANOMALY CORRELATION COEFFICIENT OF 2M TEMPERATURE

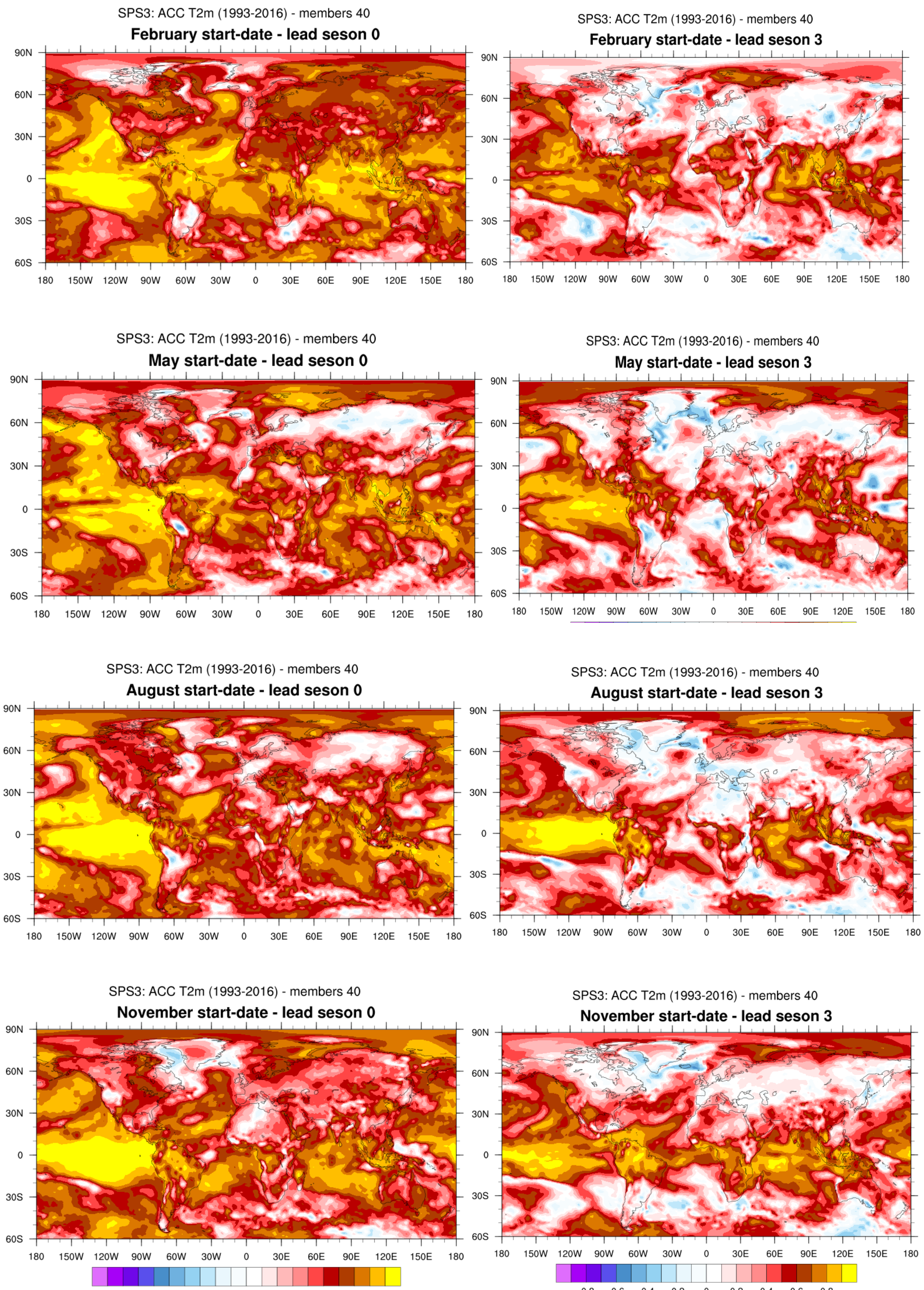

Figure 6.4 Anomaly Correlation Coefficient (ACC) for three-monthly mean T2m, all 4 start dates; lead month 0, left panels; lead month 3, right panels.

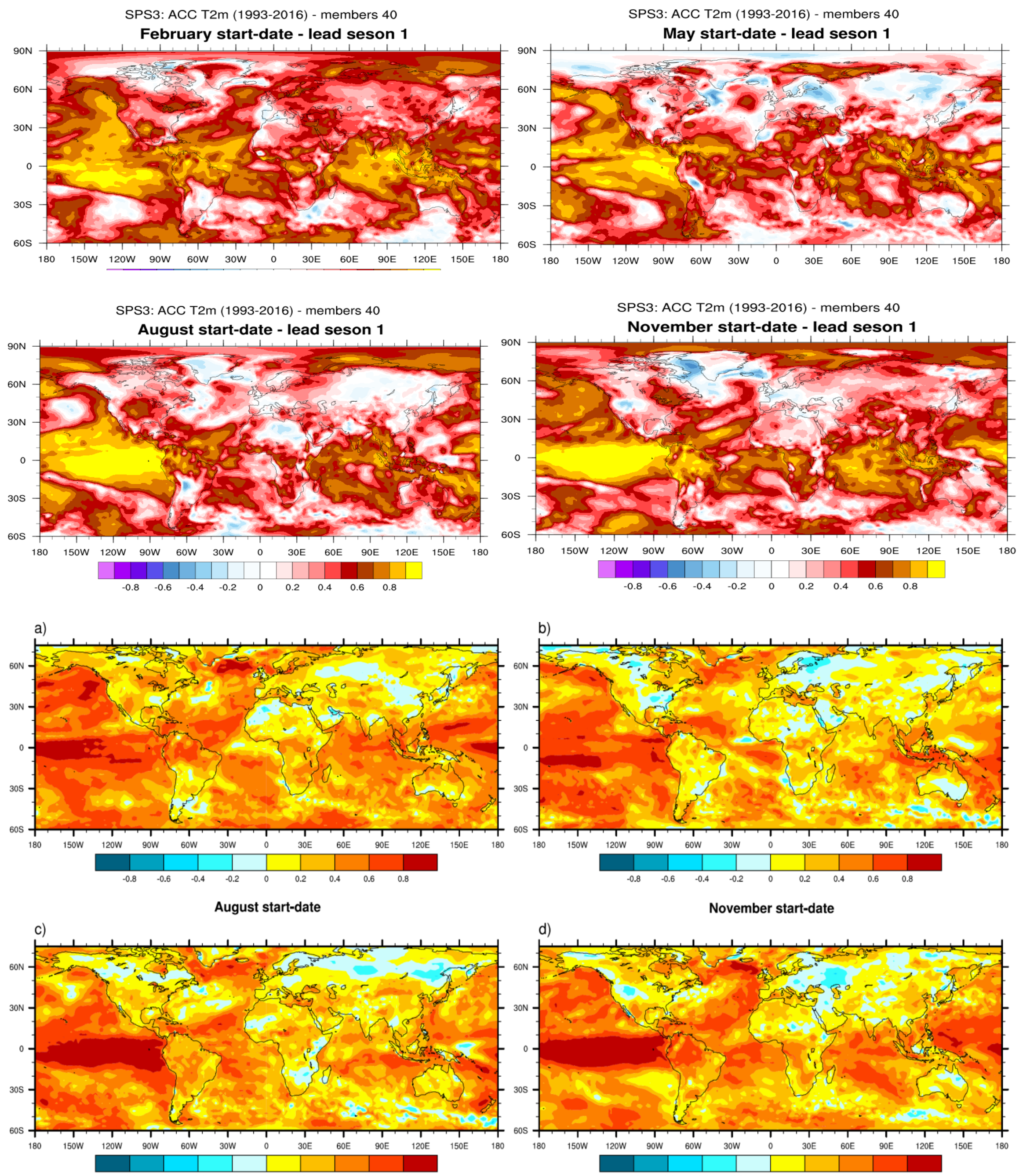

Figure 6.5 Anomaly Correlation Coefficient (ACC) for three-monthly mean T2m, all 4 start dates; lead month 1 (integrations months 2, 3 and 4; upper 4 panels) compared with ACC of Surface Temperature of the previous CMCC-SPS2 model (lower 4 panels).

6.2.2 ANOMALY CORRELATION COEFFICIENT OF PRECIPITATION

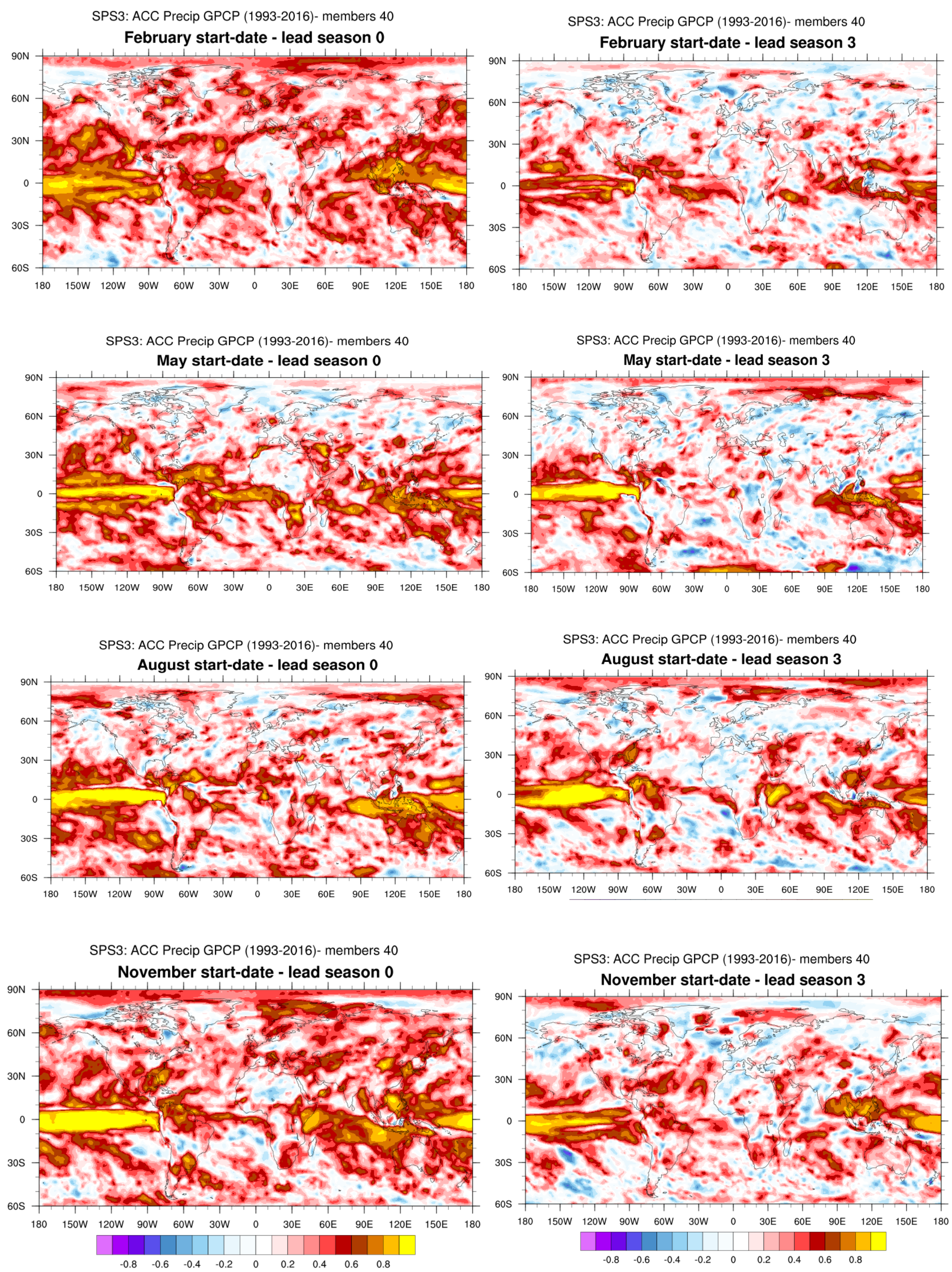

Figure 6.6 Anomaly Correlation Coefficient (ACC) for three-monthly mean Precipitation, all 4 start dates; lead month 0, left panels; lead month.

6.3 ROC SCORES

This section contains Relative Operative Characteristics (ROC; Stanski et al., 1989) Scores for 2m Temperature (Figure 6.7) and Precipitation (Figure 6.8), for start dates May (upper panels) and November (lower panels, start date May only for Precipitation), lead 0 (left panels) and lead 3 (right panels). The scores are subdivided into two terciles (upper and lower) and have been calculated using ERA-Interim to verify the near-surface temperatures and the Global Precipitation Climatology Project (GPCP; Adler et al., 2003) dataset to verify precipitation.

The ROC score is usually computed for ensemble forecast systems in order to verify the skill of the forecast in evaluating probabilities of occurrence of given events. It therefore measures the power of discrimination of the ensemble forecast and values above 0.5 denote useful skill compared to climatology.

Figure 6.7 shows the near-surface temperature ROC for upper and lower terciles in May–June–July (MJJ) and August–September–October (ASO) (start date May, lead time 0 and 3 respectively), and November–December–January (NDJ) and February–March–April (FMA) (start date November, lead time 0 and 3 respectively). The plots show useful skill across the globe, especially over the oceans and in the tropical regions. Over land, there are useful levels of skill over most of South America and large portions of Africa in both start dates and for both the upper and lower terciles. In these regions and over the tropical oceans, the skill appears to be larger at lead 0, but it remains substantial also at lead 3.

In the extratropics, at lead 0, there are useful levels of skill over Northern Europe and North America in NDJ, whereas in MJJ a reasonably good level of skill is found in Southern Europe – Mediterranean region. At lead 3, most of the continental areas of Eurasia are characterised by no skill. This verification result suggests that the model is able to significantly discriminate cold and warm episodes over the larger part of the globe.

Figure 6.8 shows the precipitation ROC for upper and lower terciles in MMJ and ASO (start date May, lead time 0 and 3 respectively). The results shown suggest that SPS3 is successful in discriminating below– and above–normal rainfall conditions over the larger part of the globe, and particularly over tropical oceans. Maximum skill is obtained on the equatorial Pacific region across all lead times. Similar skill patterns are found for large parts of tropical and Southern Africa, ranging from ROC sores of predominantly 0.6 to patches of 0.9.

According to these results, it appears evident that the performance of the model is better and more consistent in predicting near–surface temperatures than rainfall. This result is consistent with the findings from numerous similar systems (e.g., Beraki et al. 2014; MacLachlan et al. 2015).

6.3.1 ROC SCORES FOR 2M TEMPERATURE

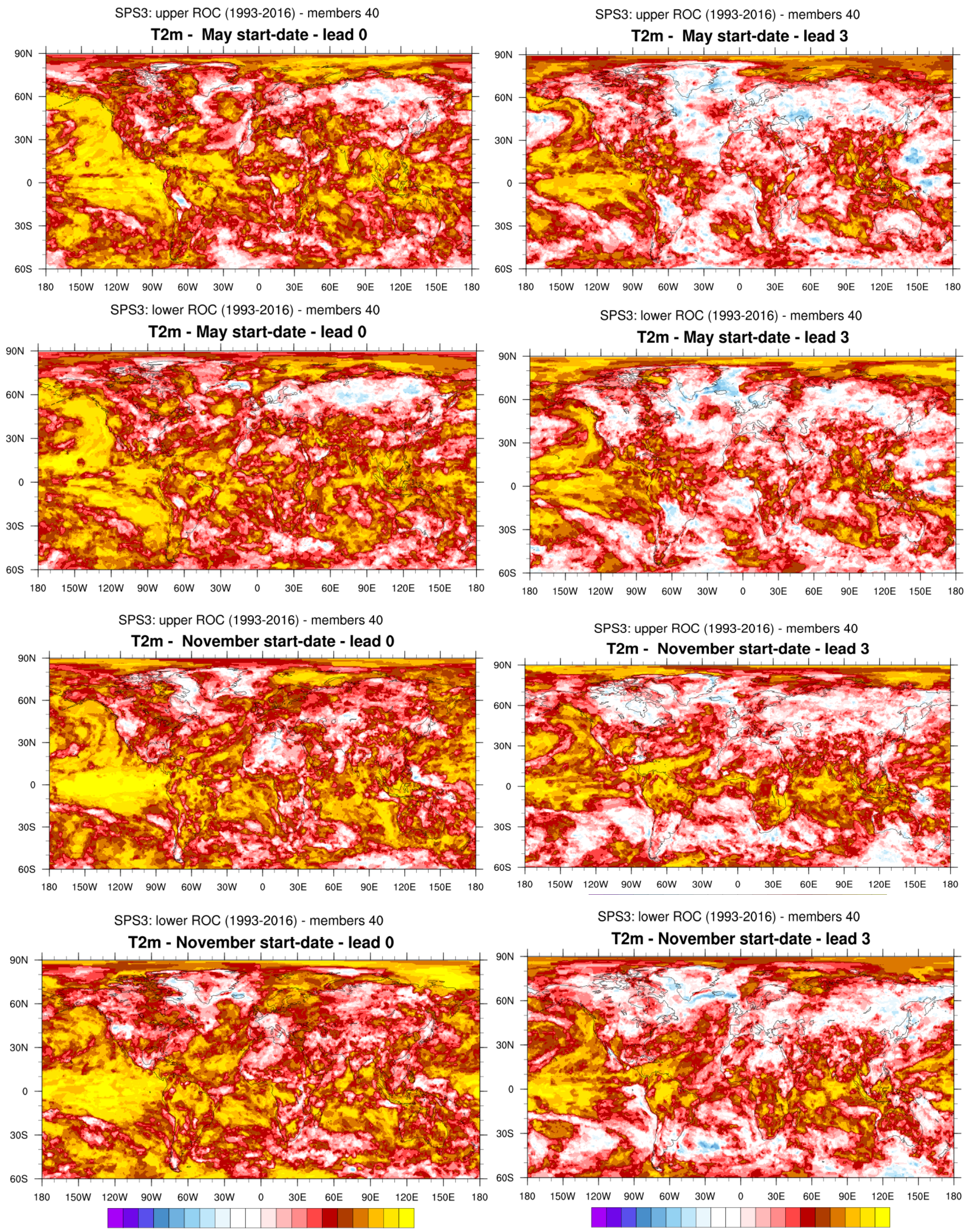

Figure 6.7 Relative Operating Characteristics (ROC Score) for three-monthly mean T2m, 4 upper panels May start date, 4 lower panels, November start date. Panels rows 1 and 3, upper tercile; panels rows 2 and 4, lower tercile. Left panels, lead 0, right panels, lead 3.

6.3.2 ROC SCORES FOR PRECIPITATION

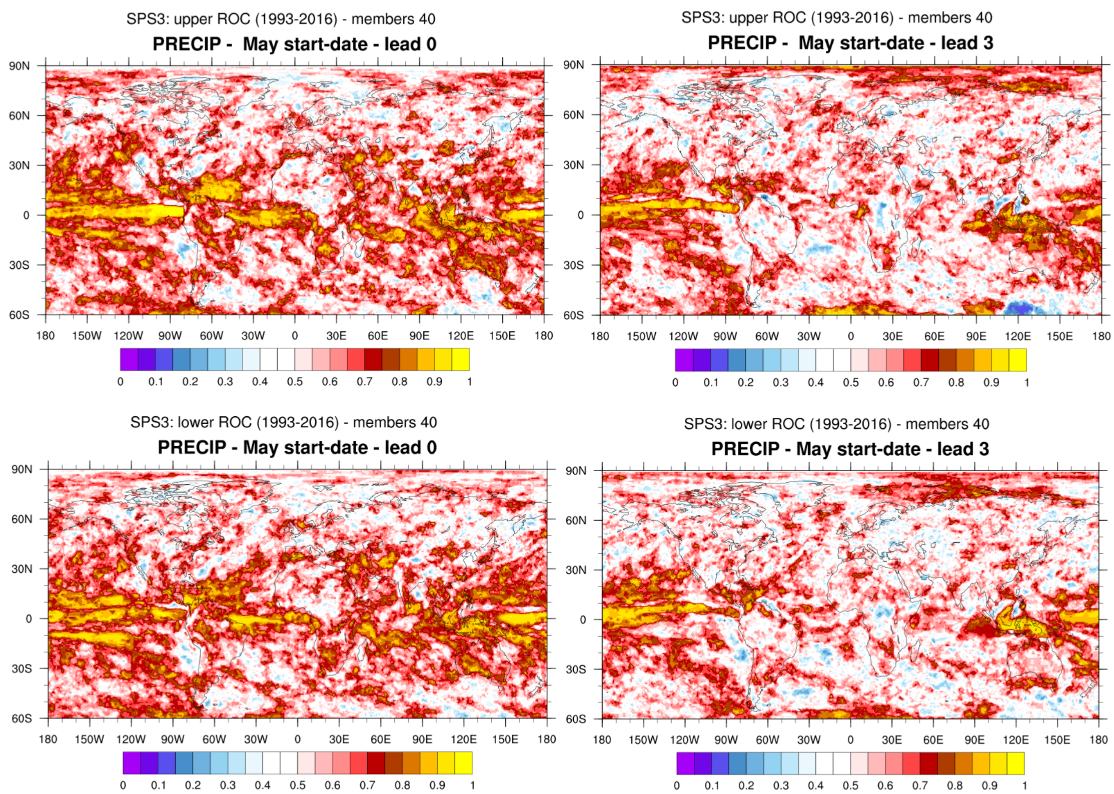

Figure 6.8: Relative Operating Characteristics (ROC Score) for three-monthly mean Precipitation, May start date. Upper panels, upper tercile; lower panels row, lower tercile. Left panels, lead 0, right panels, lead 3.

7. FORECASTING ENSO

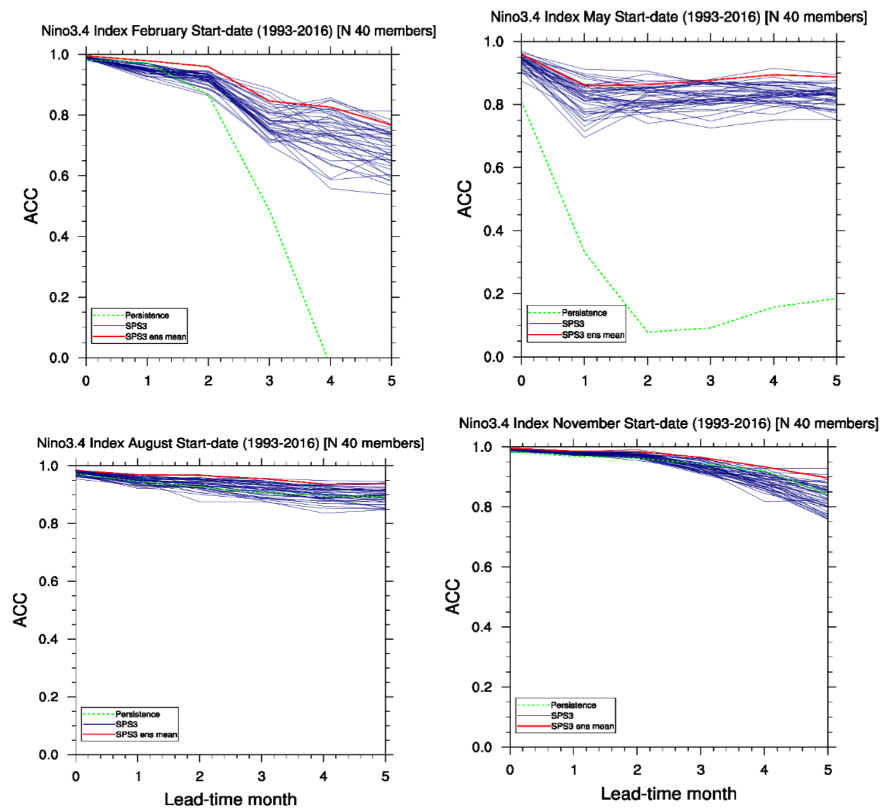

Figure 7.1. Predictive skill (ACC, anomaly correlation coefficient) of the NINO3.4 index for the 40 ensemble members of SPS3 (blue lines) and their ensemble mean (red lines). Clockwise from top left: February, May, August and November start dates. Green dashed line represents the persistence forecast.

Since the main driver of the global mean interannual SST variance is the variability in the equatorial Pacific associated with ENSO, the skill and accuracy of a seasonal prediction system in this region is a crucial ingredient for reliable seasonal forecasts. These values are displayed in Figure 7.1 and 7.2 as anomaly correlation (ACC) and root mean squared error (RMSE) respectively for the NINO3.4 region, in eastern-central equatorial Pacific.

ACC shows values higher than 0.6 in all the forecasts for every single ensemble member up to sixth forecast months (Figure 7.1) and the ensemble mean is, on average, always better than any individual member of the ensemble (deterministic forecast). RMSE shows similar characteristics (Figure 7.2), with the initial error evolving faster in the February and May start dates, and the ensemble mean having the highest accuracy. Here the ensemble spread is also shown: its value is confined within 0.4°C except for the May start date, when it exceeds this threshold after the third forecast month.

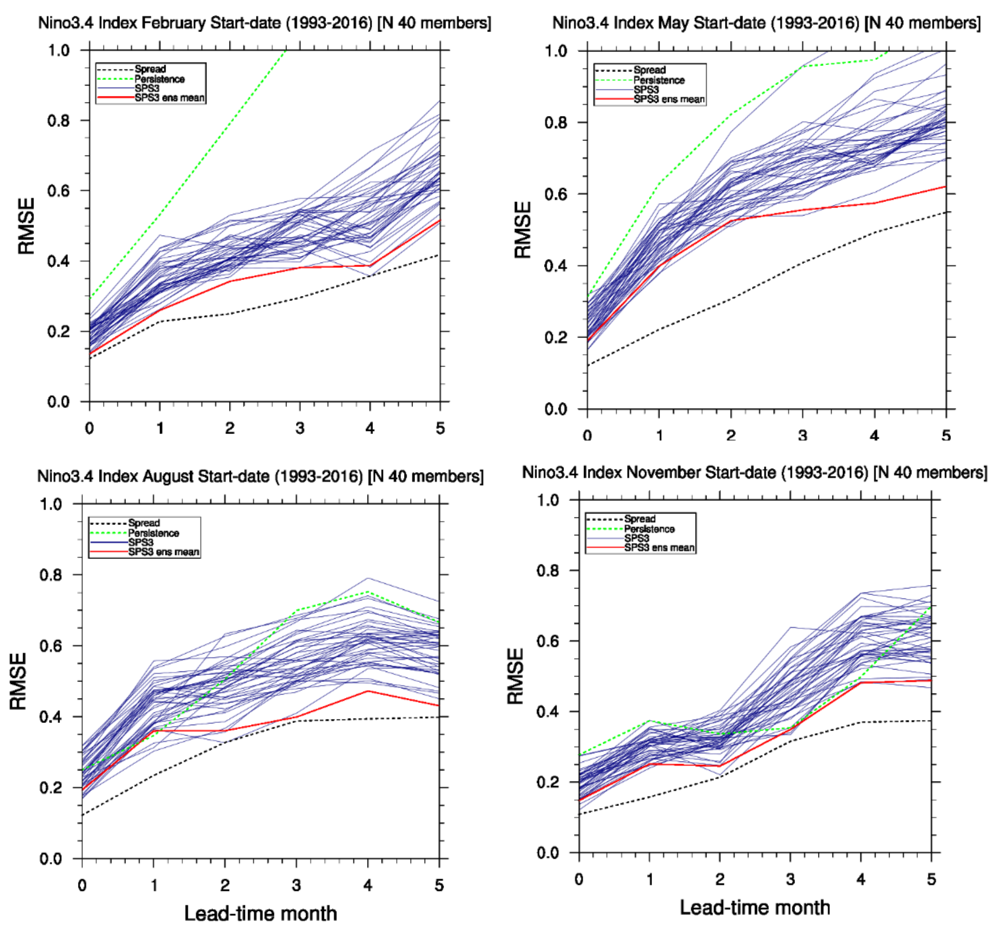

Figure 7.2. Accuracy in terms of RMSE (°C) of the NINO3.4 index for the 40 ensemble members of SPS3 (blue lines) and their ensemble mean (red lines). Clockwise from top left: February, May, August and November start dates. Green dashed line represents the persistence forecast.

Both these metrics (Figures 7.1 and 7.2, ACC and RMSE) reflect the seasonal dependency of the equatorial Pacific SST predictability: the so-called spring barrier has long been documented in ENSO forecasts as a drop of skill of the persistence forecast across the boreal spring (Chen et al., 2004). CMCC-SPS3 exhibits similar limitations due the lower predictability of ENSO in that season. This is also confirmed by the ACC curve for persistence forecast, which quickly drops to insignificant correlation values, indicating a predictability disconnection from the initial state, for February and May start dates. Instead, the ACC curve for persistence remains stable around 0.9 up to the sixth month for the start dates of August and November (Figure 7.2, lower panels), demonstrating higher SST predictability for these periods.

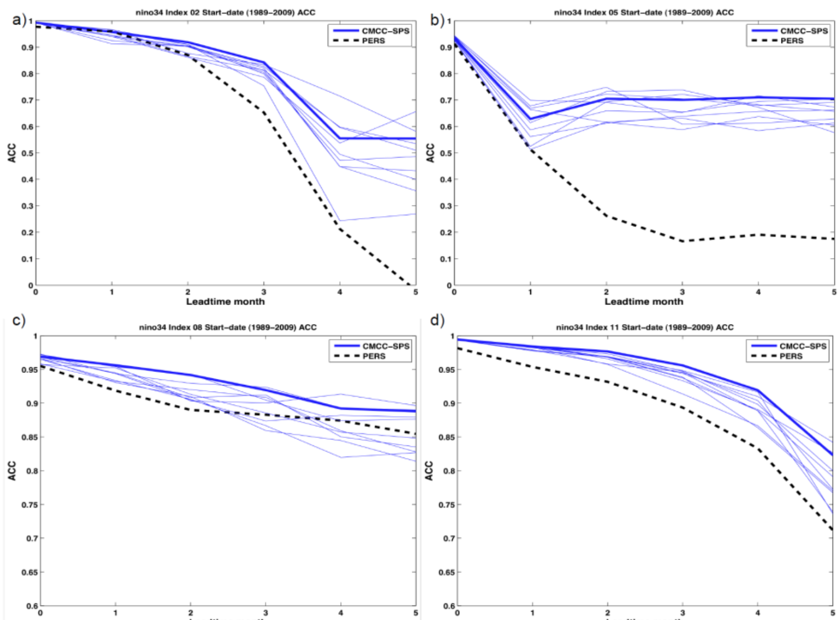

Figure 7.3 ACC of the NINO3.4 index for SPS2 ensemble members (thin lines) and ensemble mean (thick lines). a) February, b) May, c) August and d) November start dates. The black dashed line indicates persistence. The blue dashed line indicates the ensemble spread.

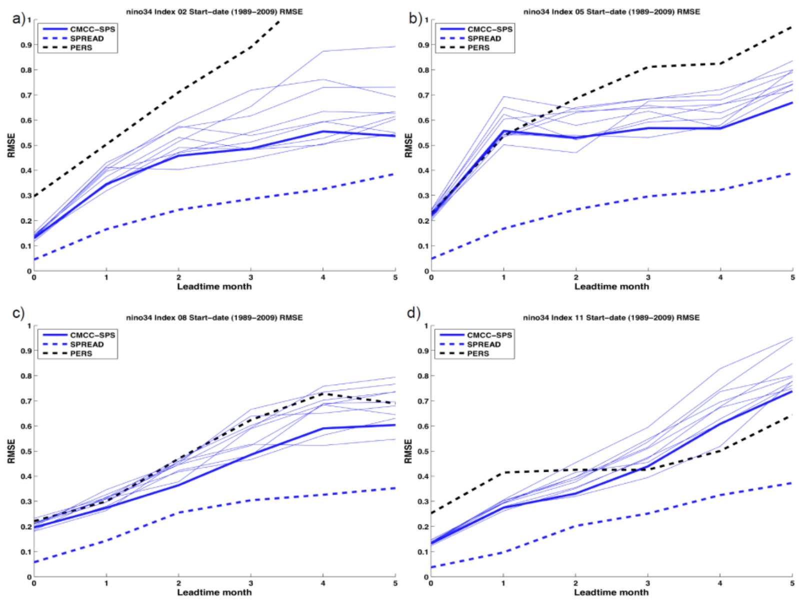

Figure 7.4 RMSE (°C) of the NINO3.4 index for (thin lines) SPS2 ensemble members and (thick line) ensemble mean. Clockwise from top left: February, May, August, November start dates. The black dashed line indicates persistence.

It is evident that the main characteristics of the RMSE and ACC curves are similar in SPS3 and SPS2, and that there is a slight improvement in terms of skill and accuracy in the most recent SPS version, especially in the forecast months farther from initialization. Despite the strong enhancement the new system has gone through, the ENSO prediction cannot improve much further, since the large majority of model skill in this area is dependent on observed initial conditions. In this regard, it is interesting to note the remarkable change in the persistence curves, which highlights that the reference period chosen has an influence on ENSO predictability.

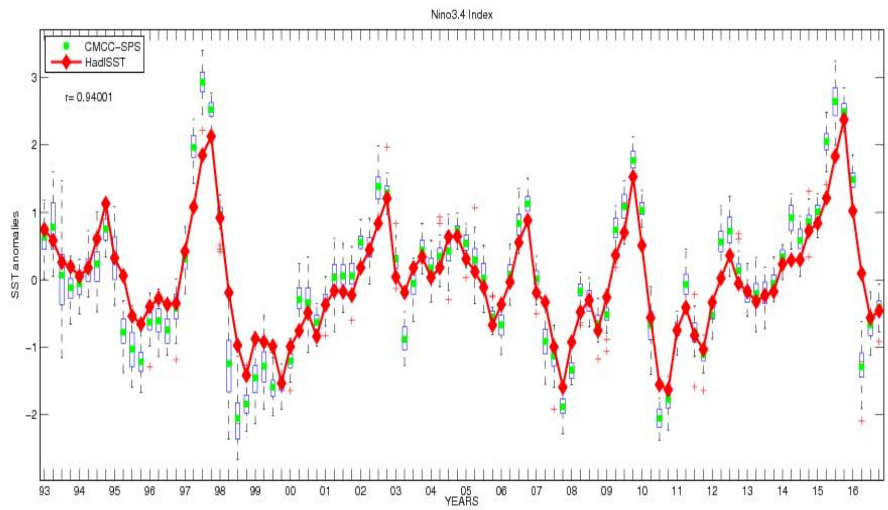

Figure 7.5. NINO3.4 index predicted for lead 1 on February, May, August and November start dates, years 1993-2016. The green dot identifies the ensemble mean, the central mark indicates the median, and the bottom and top edges of the box indicate the 25th and 75th percentiles, respectively. The whiskers extend to the most extreme data points not considered outliers, and the outliers are plotted individually using the red '+' symbol. The red diamonds linked by the red line are the observed NINO3.4 anomalies as in the HadSST2 (Rayner et al. 2006) observations.

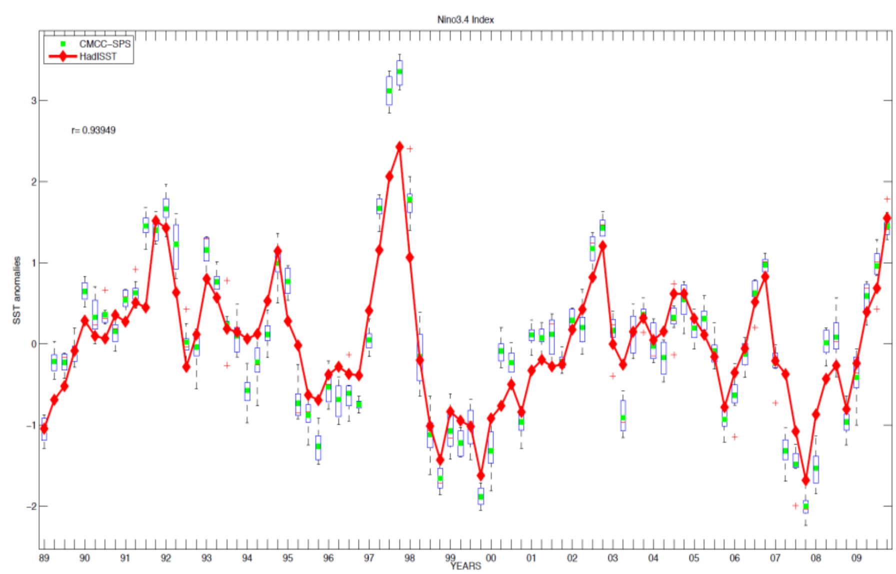

Figure 7.6 Same as Figure 7.5, but for SPS2 and for years 1989-2010.

Figure 7.5 shows the lead 1 forecast for the main start dates between 1993 and 2016. The time-series correlation is very high (0.94), while the bias is reduced much with the beginning of the century, when the ocean observation network has started expanding with the introduction of the Argo float system (Roemmich and Owens, 2000). Still, a few forecasts show larger bias comparing to the others, especially during the declining phases of strong El Niño episodes (as in 2016 and 1998) and in strong La Niña phases, which tend to be overestimated by SPS3. Figure 7.6 shows the same but for the previous CMCC-SPS2 and for a slightly different years span (1989-2010). An even stronger similarity is evident in these two diagrams, for the parts referring to the common time span, with good correspondence between timing and amplitude of maxima and minima of the index. This highlights that in going from SP2 to SPS3 the skill in predicting El Nino has improved slightly.

8. FORECASTING TELECONNECTION PATTERNS: NAO AND PNA

In seasonal forecasts, a significant part of the predictive skill in the extratropics (as well as in the Tropics, of course) depends on the prediction of large-scale teleconnections, such as the North Atlantic Oscillation (NAO) and the Pacific North American Pattern (PNA). Therefore, assessing the representation of such teleconnnections in a Seasonal Prediction System is fundamental. A more in-depth analysis is underway, here the CMCC-SPS3 re-forecasts (1993–2016) for the above-mentioned teleconnections are compared against the observations, referring to winter-mean indices.

8.1 NAO

Against past beliefs regarding the predictability of the NAO, recent studies have demonstrated significant predictive skill in wintertime exhibited by different Seasonal Prediction Systems (Riddle et al., 2013; Scaife et al., 2014, Athanasiadis et al., 2014). Furthermore, Athanasiadis et al., 2017) showed that a multi-model ensemble surpasses individual systems in this regard. Yet, the full potential of multi-model ensembles in seasonal forecasting is still to be explored and realised. CMCC-SPS3 is a good candidate for such ensembles, exhibiting NAO predictive skill comparable to other state-of-the-art systems.

Using ensemble mean MSLP anomalies from the CMCC-SPS3 hindcasts initialised in November, the NAO index for winter (DJF) was computed as in Lie and Wang (2003). In Figure 8.1 the latter is compared to the respective observed index (ERA-Interim). The correlation coefficient between such timeseries is known to depend significantly on the exact period examined (Kang et al. 2014, Shi et al., 2015). For the entire period shown (1993–2016) the correlation coefficient is not greater than 0.29, failing the statistical significance test at the 95% level (the respective threshold is 0.34 for 24 independent years). However, to allow comparison with other systems (UKMO-GloSea5, CMCC-SPS2, CFSv2 discussed in Athanasiadis et al., 2017), the correlation coefficient for CMCC-SPS3 for the same period 1997–2011 was calculated and found to be 0.50, which is found to be statistically significant at the same level (95%).

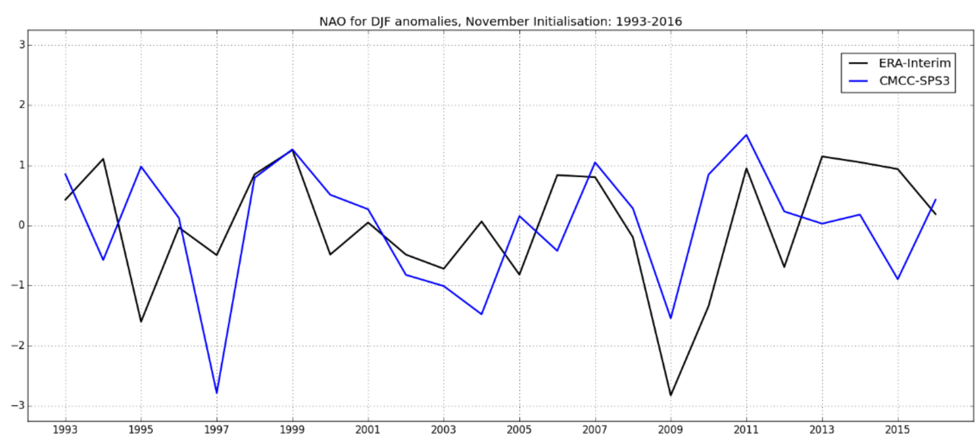

Figure 8.1 CMCC-SPS3 hindcasts of the winter-mean NAO index against the respective observed index (ERA-Interim).

8.2 PNA

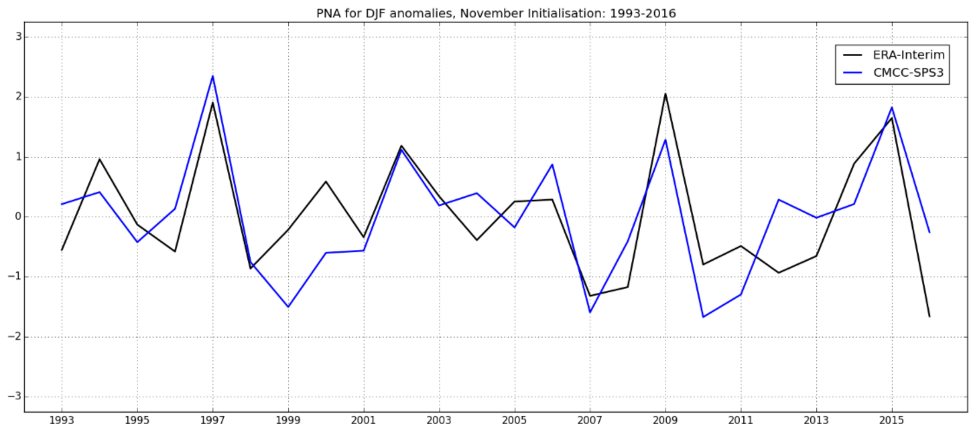

Figure 8.2 CMCC-SPS3 hindcasts of the winter-mean PNA index against the respective observed index (ERA-Interim).

Equally important to the NAO, which affects the extended North Atlantic domain, the PNA, Wallace and Gutzler (1981), is a key driver for the transient weather and climate over North America. The dynamics of the PNA produces higher predictability compared to the NAO, and a significant part of this predictability is related to ENSO and processes in the tropical Pacific. As it is the case for other Seasonal Prediction Systems, see Athanasiadis et al. (2014), the CMCC-SPS3 predictive skill for the PNA significantly exceeds that for the NAO. For the entire period shown in Figure 8.2 the correlation coefficient is 0.73, while for the period 1997–2011 it is found to be 0.82 (same as for the UKMO-GloSea5, Athanasiadis et al., 2014).

9. SOME COMPARISONS WITH OTHER STATE-OF-THE-ART FORECASTING SYSTEMS

We will attempt, in this section, a preliminary comparison exercise to measure the relative quality of CMCC-SPS3 Seasonal Forecasting System by comparing some biases and/or skill scores with other state-of-the-art Forecasting Systems. These will be, depending upon the bias/score type and the predicted variable/index, ECMWF (System 4), Meteo-France (Arpege 5), UKMO (GloSea5), NCEP (CFSv2) or the North-American Multimodel Ensemble System (NMME).

Combinations of climate variables and/or indices and skill scores shown will be:

- SST Bias: CMCC, Meteo-France, ECMWF, NCEP Figure 9.1
- T2m Bias: CMCC, Meteo France Figure 9.2
- Precipitation Bias: CMCC, Meteo-France, ECMWF, NCEP Figure 9.3
- ENSO, PNA, NAO: CMCC, NMME, UKMO, ECMWF Figure 9.4, 9.5, 9.6
- ACC T2m: CMCC, Meteo-France, ECMWF, NCEP Figure 9.7, 9.8
- ACC Precipitation CMCC, ECMWF, NCEP Figure 9.8, 9.9
- ROC score on Precip.: CMCC, UKMO, Figure 9.10, 9.11

9.1 SST BIAS

The SST bias at lead 0 for the CMCC May forecast is shown in Figure 9.1 (top left panel). Values between -0.5°C and 0.5°C have been masked, hence most ocean surface looks white in the plot. As already pointed out in Section 5, in general, Northern Hemisphere coastal sea areas appear warmer than in ERAI reanalysis, in particular at mid and high latitudes. Kuroshio current and Gulf Stream temperatures are overestimated, as well as Mediterranean coastal temperatures. The three, main coastal upwelling regions (California and Baja California, western South America and west southern Africa) are also warmer than reanalysis, but the rather high ocean resolution produces smaller biases compared to other lower resolution systems (right and lower panels of Figure 9.1) or the SPS2 version (Figure 5.12 to 5.15). The main cold bias is noticeable in the equatorial Pacific, in particular in the NINO3 and NINO3.4 regions where the error is of 1.5°C-2°C magnitude. Cold biases are also evident in sub-tropical eastern Atlantic, whose cold temperatures spread through northwestern Africa and the Portuguese coast and northern Pacific.

The SPS3 November forecast bias shown in Figure 9.1 (mid left panel) displays a warmer ocean in the Southern Hemisphere and the Tropical oceans, and a colder ocean in the Northern Hemisphere. The Kuroshio current is here colder than in reanalysis, while the Gulf Stream is still warmer but the bias magnitude is mitigated. The Mediterranean Sea and most northern Indian Ocean are affected by negative SST bias, while tropical Indian, Atlantic and the ENSO region show positive anomalies.

In a confrontation with another state-of-the-art system (Arpège System 5, AS5, top and middle right panels), SPS3 shows considerably lower biases, especially in the Northern Hemisphere, for the May forecast, while similar biases but reversed in sign can be noted in the November forecast for the subtropical Southern Ocean.

Analogous characteristics are found at mid latitudes in Southern Ocean, with patchy distribution of errors for the May start date, and a general warm bias for the November start date.

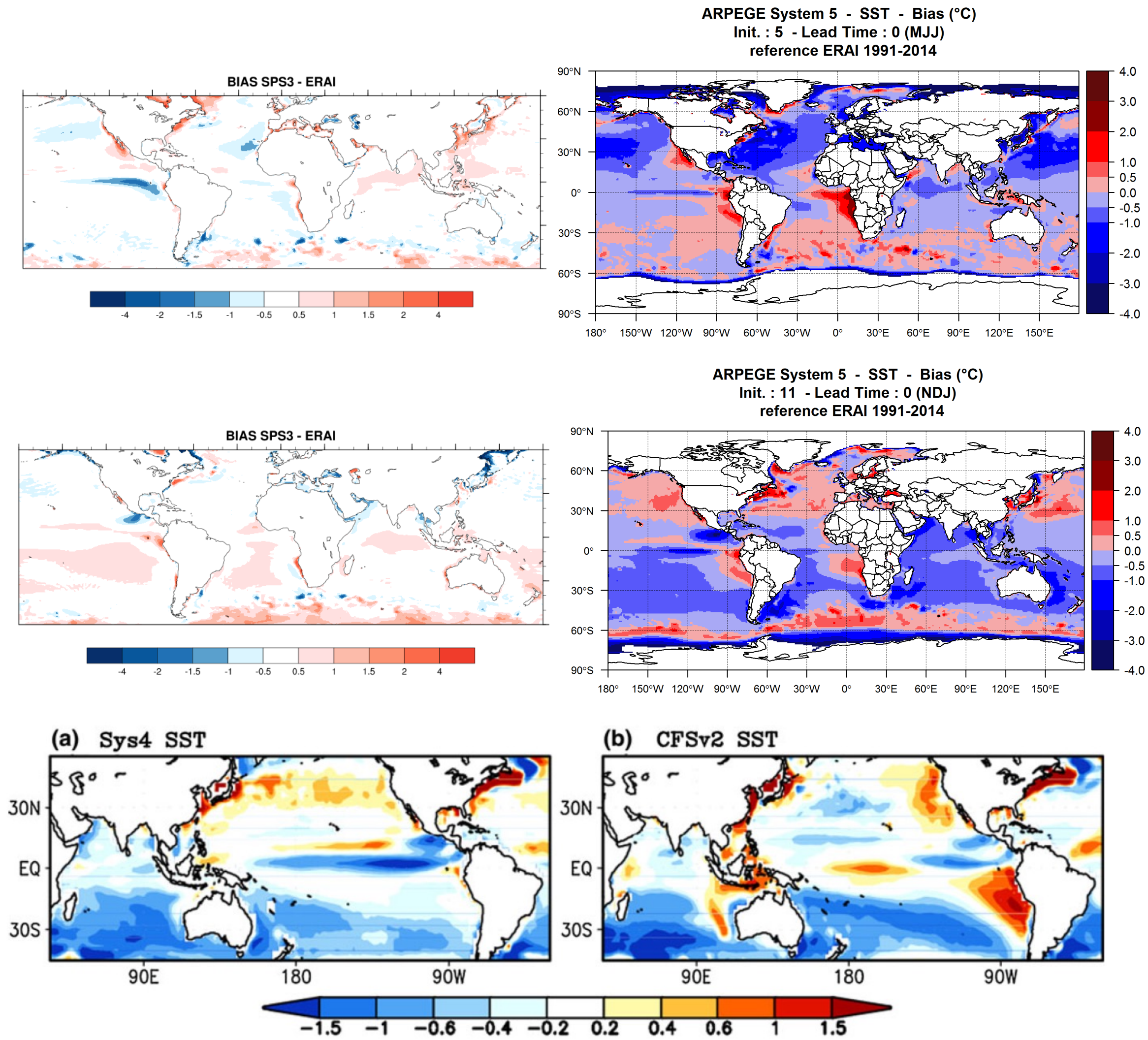

Figure 9.1 Sea Surface Temperature (SST) three-monthly model mean bias (from ERA Interim) for May start dates (upper 2 panels), and for November start dates (middle 2 panels), lead time 0. Left panels: CMCC model. Right panels: ARPEGE System 5 model (Meteo France). Lower two panels: DJF bias of Sys4 (ECMWF, left panel) and CFSv2 (NCEP, right panel), both for lead time 1.

Figure 9.1, two lower most panels, show the SST bias of ECMWF Sys4 (left) and NCEP CFSv2 (right) for Indian and Pacific Oceans. In the equatorial Pacific Ocean a much more pronounced cold bias is evident together with a large negative bias in the southern Indian Ocean, where SPS3 performs considerably better. CFS2 (right panel) also exhibits large negative biases in both middle and high latitudes of Indian and

Pacific Oceans, together with a very intense positive error spot in the upwelling region off the South American Pacific coast (both features being absent in SPS3).

We can therefore conclude that SPS3, as far as SST bias is concerned, performs as well or better than all three other state – of – the – art models here considered.

9.2 T2M BIAS

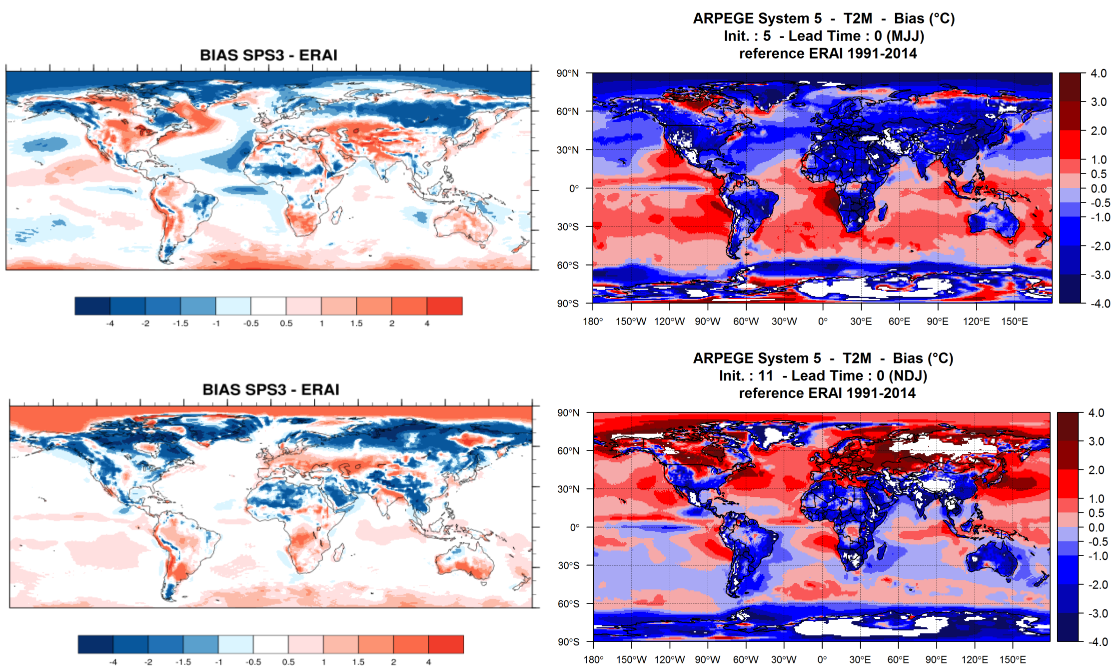

Figure 9.2 Temperature at 2m three-monthly model mean bias (from ERA Interim) for May start dates (upper 2 panels), and for November start dates (lower 2 panels), lead time 0. Left panels: CMCC model. Right panels: ARPEGE System 5 model (Meteo France).

Compared to ERAI reanalysis, SPS3 shows 2m-temperature bias, Figure 9.2, left panels, lower than 4°C in the May start date forecasts (lead time 0, top left panel), while larger cold biases are found in the November start date over Northern Siberia and Northern Canada (lead time 0, bottom left panel). In fact, the November start date bias is very sensitive to snow initialization and evolution, whose bias can strongly affect near surface temperatures, triggering large errors. Similar dynamics are forced by sea–ice biases: if the simulation of Arctic sea–ice is defective, so will be the corresponding 2m temperature.

Cold and warm biases are homogeneously distributed in the May forecast, while in November warm (cold) errors are mostly occurring in the Southern (Northern) Hemisphere, with the exceptions of Southern Europe, Southwestern Asia and Northern India. In the other state-of-the-art system considered here (Arpege System 5, right panels) the sign of the anomalies is reversed in the November forecast, while in May the great majority of lands display a cold bias. On the basis of these figures, it can be concluded that CMCC-SPS3 accuracy is totally comparable to the other state-of-the-art SPS.

9.3 PRECIPITATION BIAS

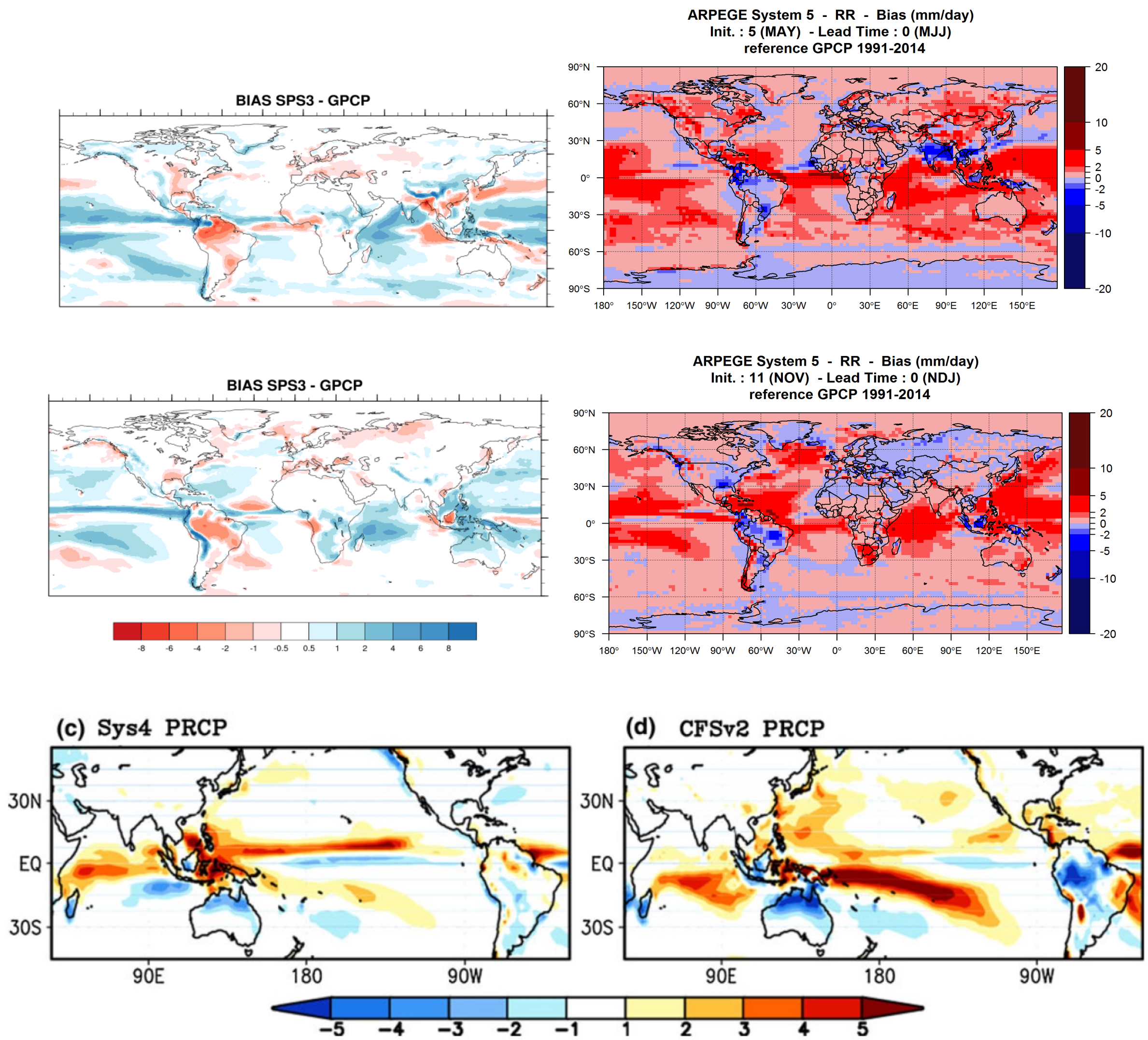

Figure 9.3 Precipitation three-monthly model mean bias (from ERA Interim) for May start dates (upper 2 panels), and for November start dates (middle 2 panels), lead time 0. Left panels: CMCC model. Right panels: ARPEGE System 5 model (Meteo France). Lower two panels: DJF bias of Sys4 (ECMWF, left panel) and CFSv2 (NCEP, right panel), both for lead time 1.

Figure 9.3 illustrates Precipitation bias. The colour–bars between CMCC-SPS3 (top and middle left panels) and Arpege System 5 (top and middle right panels) are reversed, and unfortunately the values intervals are different. However, it is possible to notice strong similarities between the biases of the two systems, both on land and ocean. Both systems show wet biases over the tropical oceans and in the winter Hemisphere, while on land they display dry errors in Asia and North America in the November forecast, and wet errors in the May forecast. South America is generally drier than NCEP (GPCP) reanalysis in both systems.

Also, the amplitude of biases is comparable between the two systems and also with ECMWF Sys4 and NCEP CFSv2 (two lower most panels), making CMCC-SPS3 as accurate as any other state-of-art prediction system.

Importantly, with the exception of Sys4, all other three systems display the typical double ITCZ error for both start dates.

9.4 ENSO (EL NIÑO 3.4)

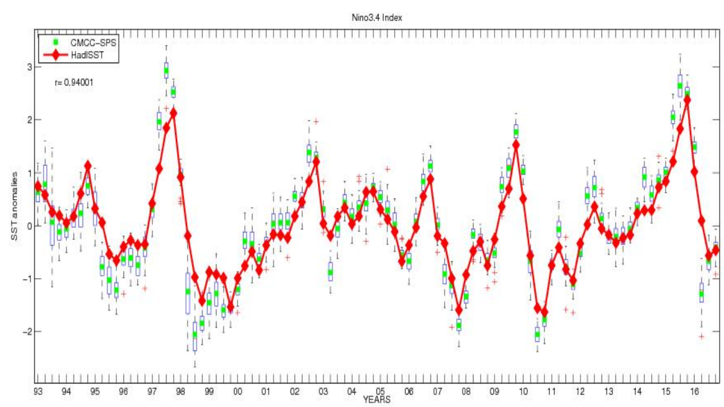

Figure 9.4. Nino 3.4 index predicted by CMCC-SPS3 for lead 1 on February, May, August and November start dates, years 1993-2016. The green dot identifies the ensemble mean, the central mark indicates the median, and the bottom and top edges of the box indicate the 25th and 75th percentiles, respectively. The whiskers extend to the most extreme data points not considered outliers, and the outliers are plotted individually using the red '+' symbol. The red diamonds linked by the red line are the observed NINO3.4 anomalies as in the HadSST2 (Rayner et al. 2006) observations.

In Figures 9.4 and 9.5 the values of the CMCC-SPS3 NINO3.4 index are compared to those of the North America Multi-Model (NMME), showing that values are quite comparable with those of a multi-model ensemble, which can feature about the double of ensemble members. Like NMME, SPS3 shows the largest discrepancies from observations in extreme ENSO years, such as 1997 (El Niño) and 1998-1999 (La Niña).

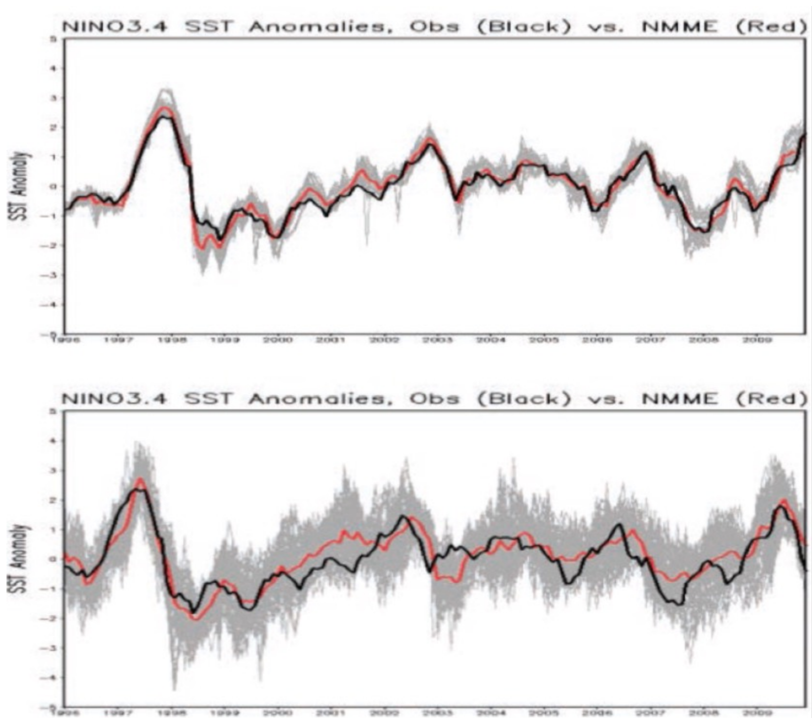

Figure 9.5 Nino 3.4 index as predicted by the NMME (North American Multi-Model Ensemble. Area-averaged SSTA 5°S–5°N, 170°–120°W) plumes for (top) lead month 0 and (bottom) lead month 6. Both series encompass the 1996–2010 period, red lines indicate the ensemble mean of NMME prediction, grey bands the 79 ensemble members, black lines the observations. From Kirtman et al., (2014).

9.5 PNA AND NAO

Regarding the predictive skill for the main extratropical teleconnections of the Northern Hemisphere, referring to the NAO and the PNA, the CMCC-SPS3 shows a behaviour similar to that of other state-of-the-art SPSs. Generally, the respective skill (ACC) for a given season and lead time is known to depend strongly on the ensemble size, as well as on the historical period considered. A fair comparison between different

SPSs should consider this dependence, yet such a thorough comparison would go beyond the scope of this report. Here only some general indications are given.

Regarding the PNA, the predictive skill of CMCC-SPS3 is very good. In particular, as mentioned earlier, the lead-1 CMCC-SPS3 skill for wintertime in the period 1997–2011 (0.82) matches that of the UKMO-GloSea5 computed for the same period (Athanasiadis et al., 2014, in Figure 9.6 top left panel). Also, the CMCC-SPS3 appears to outperform the CMCC-SPS2 (Figure 9.6 bottom left panel) as well as the ECMWF-Sys4 and CFSv2 (Kim et al., 2012, in Figure 9.6 bottom right panel). It should be noted, however, that the correlations quoted for these three systems in Figure 9.6 refer to slightly different periods and ensemble sizes.

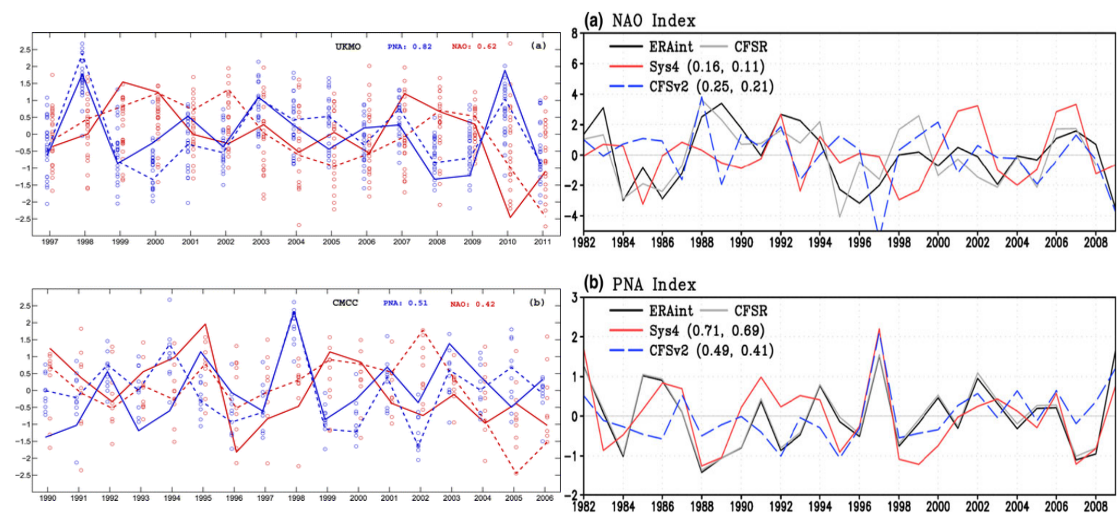

Figure 9.6 PNA and NAO indices as predicted by different SPSs, on the left for the UKMO-GloSea5 and CMCC-SPS2, from Athanasiadis et al. (2014) and on the right for ECMWF-Sys4 and NCEP-CFSv2, from Kim et al. (2012).

The predictive skill for the NAO in wintertime, with all correlations computed for the same period (1997–2011) and lead time (lead 1), appears to be higher in the UKMO-GloSea5 and CFSv2 systems than in CMCC-SPS3 (Athanasiadis et al., 2017, Table 1). Nevertheless, CMCC-SPS3 does exhibit a statistically significant correlation for that period (0.50). For a different period (1982–2008) ECMWF-Sys4 and CFSv2 do not exhibit statistically significant correlations (Kim et al., 2012, Figure 9.6 top right panel).

To conclude this section, it is evident that, in order to exhaustively assess the performance of CMCC-SPS3 against other state-of-the-art systems, further analysis is required.

9.6 ACC OF T2M

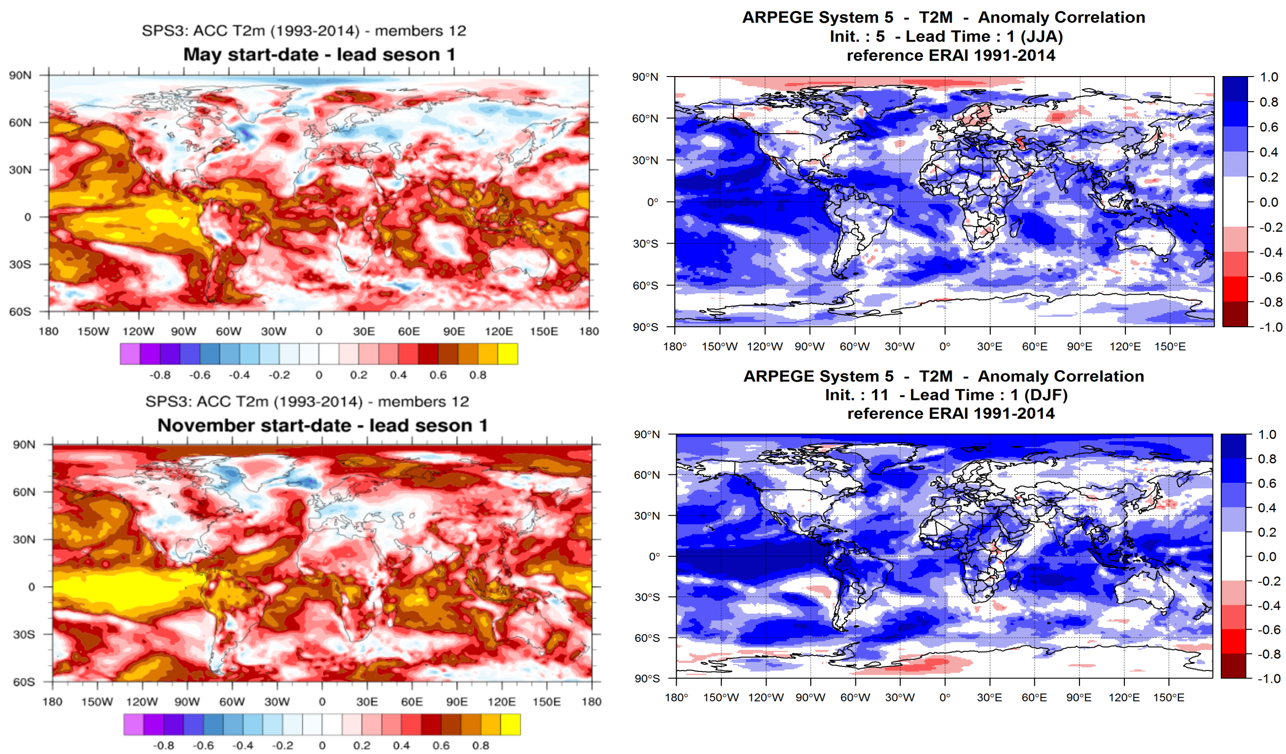

Figure 9.7. Anomaly Correlation Coefficient (ACC) for three-monthly mean T2m. May start date (upper panels) and November start date (lower panels), lead month 1. Left panels, CMCC model; right panels, ARPEGE System 5 model (Meteo France).

In terms of predicting near-surface air temperature (T2m) anomalies, a comparison is made separately for summertime (against ARPEGE-Sys5) and for wintertime (against ARPEGE-Sys5, ECMWF-Sys4 and NCEP CFSv2, see Figures 9.7 and 9.8). Yet, again, the respective periods are not precisely the same.

For the summer season (May start date, Figure 9.7, top panels) the CMCC-SPS3 seems to be performing better than the ARPEGE-Sys5 in the Tropics and to be slightly less skilful than the latter only over certain areas of the North Atlantic (e.g., south of Greenland, where CMCC-SPS3 suffers from significant SST biases). In contrast, the ACC of CMCC-SPS3 exceeds 0.8 over large parts of the Pacific (Tropics and extratropics) and of the tropical Atlantic.

Regarding wintertime (November start date, Figure 9.7, lower panels and Figure 9.8, left panels), the CMCC-SPS3 appears to overperform CFSv2 almost everywhere and also to match the ECMWF-Sys4 skill in most areas of the globe. Again, in the area south of Greenland, where the Gulf Stream extends, the CMCC-SPS3 seems to have difficulty in matching the skill of the other systems.

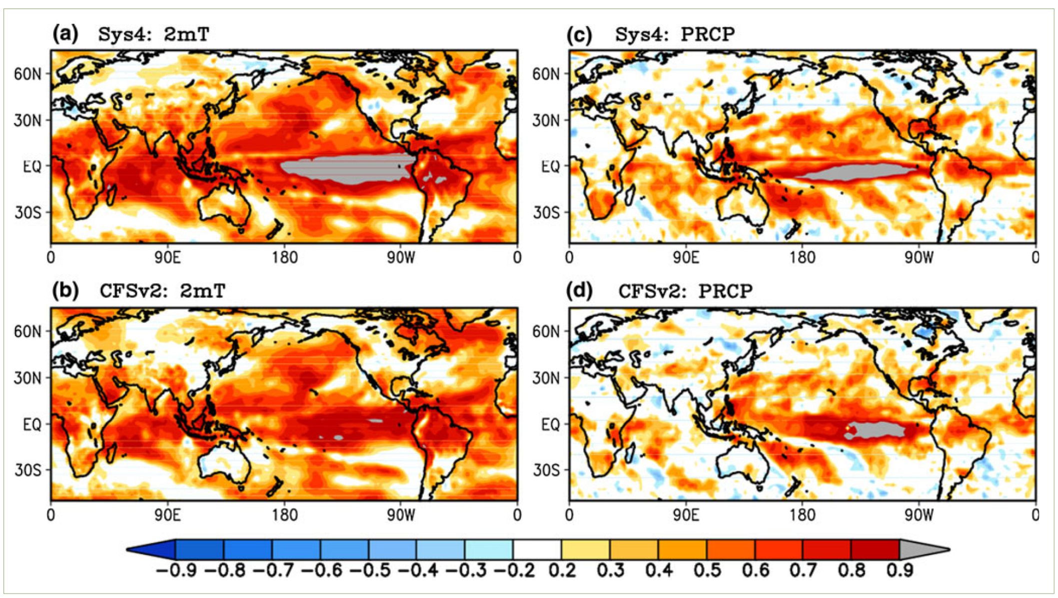

Figure 9.8. Figure adapted from Kim et al. (2012). Anomaly Correlation Coefficient (ACC) for the November start date (DJF), left panels for T2m and right panels for precipitation. Top panels Sys4 (ECMWF), left panels CFSv2 (NCEP).

9.7 ACC AND ROC SCORE FOR PRECIPITATION

Regarding precipitation and focusing on ACC, CMCC-SPS3 (Figure 9.9) compares very well with ECMWF-Sys4 and CFSv2 for the November start date (from Kim, et al., 2012; Fig 9.8, right panels). Again, noting that correlations are computed for slightly different periods (i.e. 1997–2011 versus 1993–2016), CMCC-SPS3 has larger areas with very high skill (>0.9) in the tropical Pacific than both of the above-mentioned systems. It also has better skill (>0.7) over the Indian Ocean, Western Australia, NE part of South America and the subtropical North Atlantic.

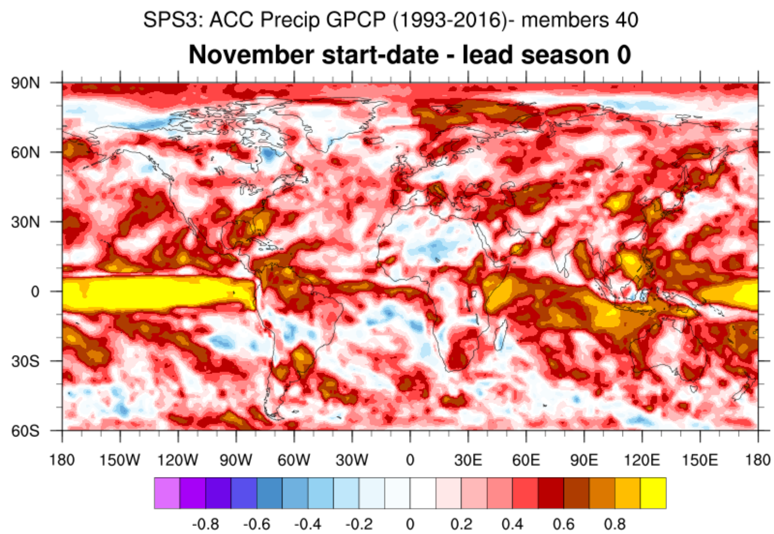

Figure 9.9. CMCC SPS3 Anomaly Correlation Coefficient (ACC) for three-monthly mean Precipitation. November start date, lead month 1.

Considering ROC scores for the three tercile categories (upper, middle and lower tercile) shown in Figure 9.10 and 9.11 for May and November start dates respectively, a comparison of CMCC-SPS3 with UKMO-GloSea5 shows that the former is at least equally good in the Tropics. It is, however, also equally bad in the extratropics, a feature unfortunately common to practically all currently operational state-of-the-art SPSs.

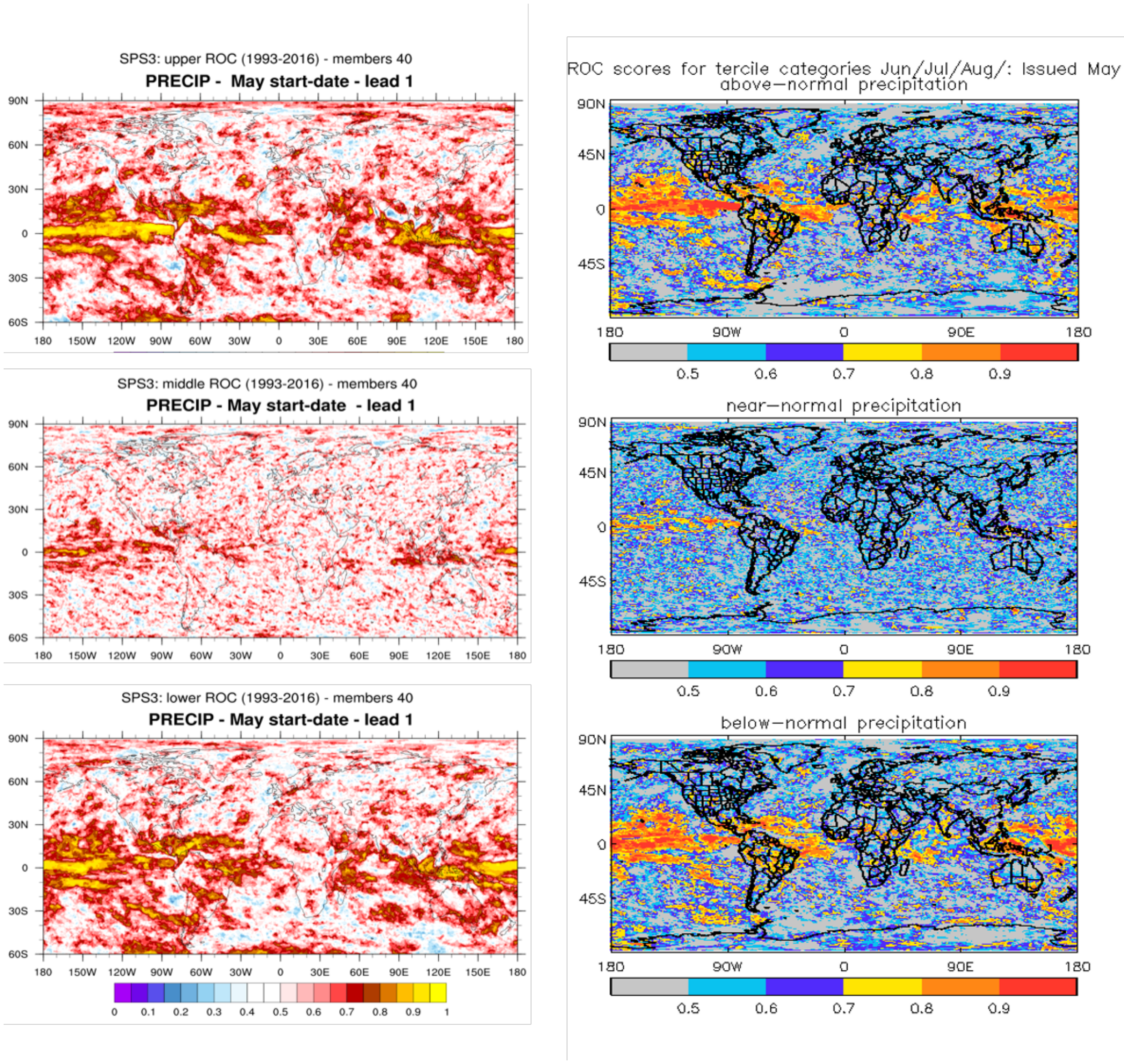

Figure 9.10. Relative Operating Characteristics (ROC Score) for three-monthly mean Precipitation, May start date, lead 1. Upper panel, upper tercile; middle panel, middle tercile; lower panel, lower tercile. Left panels, CMCC Model; right panels, UKMO Model.

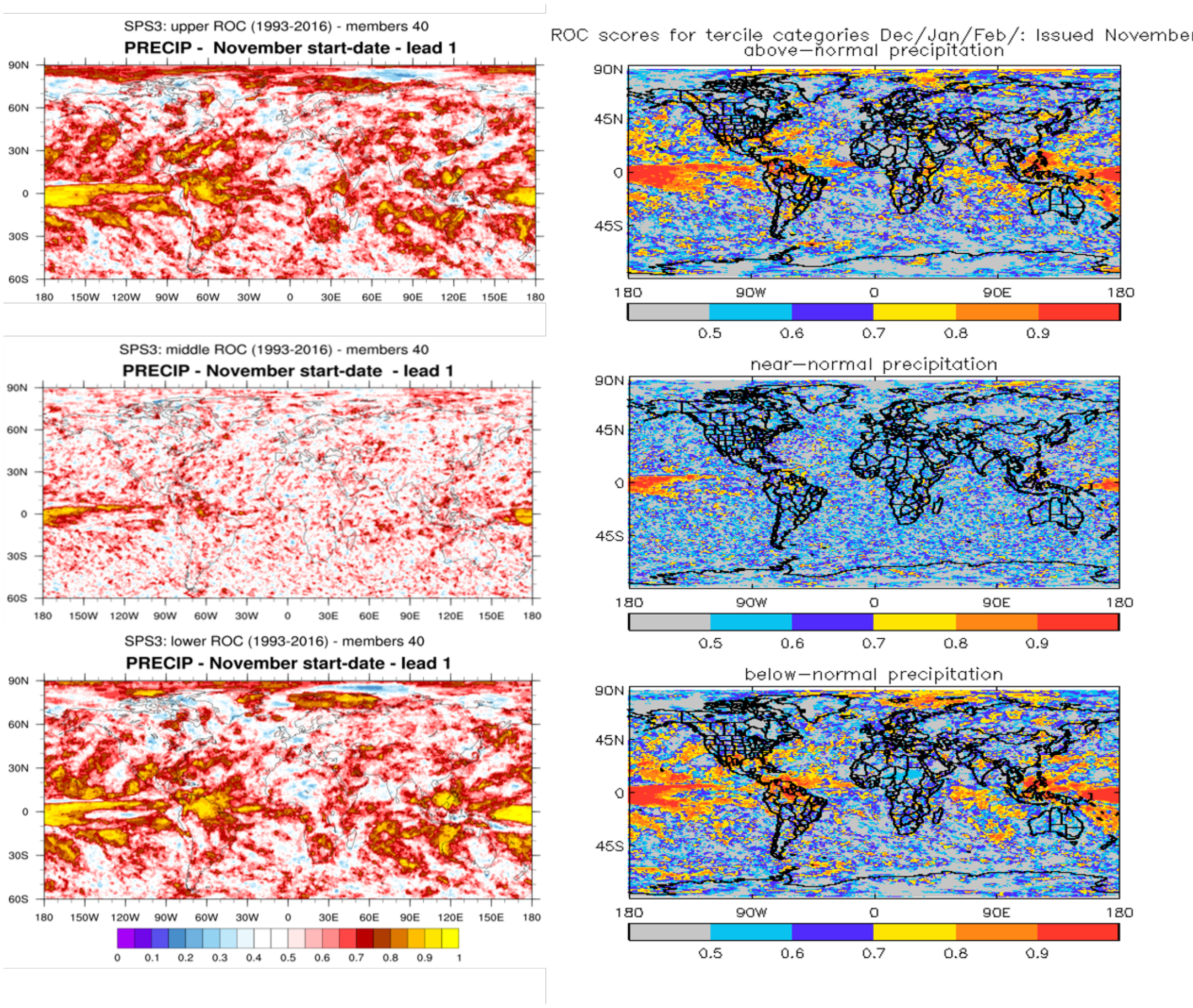

Figure 9.11. Relative Operating Characteristics (ROC Score) for three-monthly mean Precipitation, November start date, lead 1. Upper panel, upper tercile; middle panel, middle tercile; lower panel, lower tercile. Left panels, CMCC Model; right panels, UKMO Model.

10. CONCLUSIONS

The purpose of this Technical Report is to assess and document in an objective and comparable way the overall quality of the CMCC-SPS3 Seasonal Prediction System in full ensemble configuration, both in terms of model climate and of model performance in seasonal prediction mode. The assessment has been made on the basis of the so-called “re-forecast” period, i.e. the 24-year period spanning from 1993 to 2016, using 6-month forecasts starting from the 4 canonical dates of February 1st, May 1st, August 1st and November 1st and being based on forecast ensembles of 40 members. The overall number of single model integrations amounts, therefore, to 24x4x40=3840 6-month long integrations, for a total of 1920 years of model integration time.

The assessment has been based primarily on the computation of the model bias as portrayed by atmospheric temperature, precipitation, MSLP and 500 hPa height and of SST. Atmospheric 2m temperature and precipitation seasonal forecasts have been objectively scored in terms of RMS Errors, ACC and ROC Scores.

The capability of the model to represent and predict ENSO in terms of El Niño 3.4 Index has been assessed and compared with other models of similar complexity, usually used to produce similar seasonal forecasts.

In the light of the widespread interest in seasonal forecasts for the NH midlatitudes, the capability of the CMCC-SPS3 system to forecast important teleconnection patterns like the NAO and the PNA has also been assessed and compared with other systems.

The CMCC-SPS3 Seasonal Prediction System has been confirmed as a State-of-the-art seasonal prediction system capable of producing operational seasonal forecasts with acceptable model biases and demonstrable skill both in tropical regions and in the midlatitudes. Particularly good skill is shown in forecasting ENSO in tropical regions and important teleconnection patterns like NAO and PNA in midlatitudes.

11. BIBLIOGRAPHY

Adler R., G. Huffman, A. Chang, R. Ferraro, P. Xie, J. Janowiak, B. Rudolf, U. Schneider, S. Curtis, D. Bolvin, A. Gruber, J. Susskind, P. Arkin and E. Nelkin, 2003: The version 2 Global Precipitation Climatology Project (GPCP) monthly precipitation analysis (1979–present). J. Hydrometeorol. 4: 1147–1167.

Alessandri, A., A. Borrelli, S. Masina, A. Cherchi, S. Gualdi, A. Navarra, P. Di Pietro, A.F. Carril, 2010: The INGV–CMCC Seasonal Prediction System: Improved Ocean Initial Conditions. Mon. Wea. Rev., 138, 2930–2952. doi: 10.1175/2010MWR3178.1.

Alessandri, A., A. Borrelli, A. Navarra, A. Arribas, M. Déqué, P. Rogel, A. Weisheimer, 2011: Evaluation of Probabilistic Quality and Value of the ENSEMBLES Multimodel Seasonal Forecasts: Comparison with DEMETER. Mon. Wea. Rev., 139, 581–607. doi: 10.1175/2010MWR3417.1.

Athanasiadis, P. J., Bellucci, A., Hermanson, L., Scaife, A. A., MacLachlan, C., Arribas, A., ... & Gualdi, S., 2014. The Representation of Atmospheric Blocking and the Associated Low-Frequency Variability in Two Seasonal Prediction Systems. Journal of Climate, 27(24), 9082-9100, doi:10.1175/JCLI-D-14-00291.1.

Athanasiadis, P. J., J. M. Wallace, and J. J. Wettstein, 2010: Patterns of wintertime jet stream variability and their relation to the storm tracks. J. Atmos. Sci., 67, 1361–1381, doi:10.1175/ 2009JAS3270.1.

Athanasiadis, P.J. et al., 2017: A Multisystem View of Wintertime NAO Seasonal Predictions. Journ. Clim, 30, 1461-1475, doi: 10.1175/JCLI-D-16-0153.1

Beraki, A. F., D. G. DeWitt, W. A. Landman, and C. Olivier, 2014: Dynamical seasonal climate prediction using an ocean–atmosphere coupled climate model developed in partnership between South Africa and the IRI. *J. Climate*, 27, 1719–1741, doi:10.1175/JCLI-D-13-00275.1.

Bernie DJ, Guilyardi E, Madec G, Slingo JM, Woolnough SJ. 2007. Impact of resolving the diurnal cycle in an ocean-atmosphere GCM. Part 1: a diurnally forced OGCM. Clim. Dynam. 29: 575-590.

Bitz, C. M., and Lipscomb, W. H. (1999). A new energy-conserving sea ice model for climate study. J. Geophys. Res, 104(15), 669-15.

Branstetter, M.L., and James S. Famiglietti (1999). Testing the sensitivity of GCM-simulated runoff to climate model resolution using a parallel river transport algorithm. Proceedings of 14th Conference on Hydrology, American Meteorological Society, Dallas, Texas.

Branstetter, M.L. (2001). Development of a parallel river transport algorithm and applications to climate studies. University of Texas.

Briegleb, B. P., & Light, B. (2007). A Delta-Eddington multiple scattering parameterization for solar radiation in the sea ice component of the Community Climate System Model. NCAR Tech. Note NCAR/TN-472+ STR, 100.

Bretherton, M. G. Flanner, and D. Mitchell. Toward a minimal rep- resentation of aerosols in climate models: description and evaluation in the Community Atmosphere Model CAM5. Geosci. Model Dev., 5(3):709–739, 2012. doi: 10.5194/gmd-5-709-2012.

Cavalieri, D. J., C. L. Parkinson, P. Gloersen, J. C. Comiso, and H. J. Zwally, 1999. Deriving long-term time series of sea ice cover from satellite passive-microwave multisensor data sets. J. Geophys. Res., 104, 15803–15814.

Chen D., Cane M.A., Kaplan A., Zebiak S.E., Huang D., 2004: Predictability of El Nino over the past 148 years. Nature 428, 733-736.

Courtier, P., Anderson, E., Heckley, W., Pailleux, J., Vasiljeric, D., Hamrud, M., Hollingsworth, A., Rabier, F., and Fisher, M.: The ECMWF implementation of three-dimensional variational assimilation (3D-Var): Formulation (1998). Q. J. R. Meteorol. Soc., 124, 1783–1807.

Craig, A. P., Vertenstein, M., & Jacob, R. (2011). A new flexible coupler for earth system modeling developed for CCSM4 and CESM1. International Journal of High Performance Computing Applications, 1094342011428141.

Davini, P., C. Cagnazzo, S. Gualdi, and A. Navarra, 2012: Bidimensional diagnostics, variability, and trends of Northern Hemisphere blocking. J. Climate, 25, 6496–6509, doi:10.1175/ JCLI-D-12-00032.1.

Dee, D., et al., 2011. The ERA-Interim reanalysis: configuration and performance of the data assimilation system. Q. J. R. Meteorol. Soc., 137, 553–597.

Dobricic S, Pinardi N. 2008. An oceanographic three-dimensional assimilation scheme. Ocean Model. 22: 89-105.

Flanner, M.G., et al. (2007). Present-day climate forcing and response from black carbon snow. Journal of Geophysical Research: Atmospheres. 112, D11.

Fogli, Pier Giuseppe, and D. Iovino. "CMCC–CESM–NEMO: Toward the New CMCC Earth System Model." CMCC Research Paper 248 (2014).

Gaspar, P., Y. Gregoris, and J.-M. Lefevre (1990). A simple eddy kinetic energy model for simulations of the oceanic vertical mixing Tests at station papa and long-term upper ocean study site. J. Geophys. Res, 95 (C9).

Gettelman, A., H. Morrison, and Steven J. Ghan. (2008). A new two-moment bulk stratiform cloud microphysics scheme in the Community Atmosphere Model, version 3 (CAM3). Part II: Single-column and global results." Journal of Climate 21(15): 3660-3679.

Good S, Martin M, Rayner N. 2013. EN4: quality controlled ocean temperature and salinity profiles and monthly objective analyses with uncertainty estimates, Journal of Geophysical Research Oceans 118: 6704-6716,

Griffies, S. (2004). Fundamentals of ocean climate models. Princeton University Press, 434pp.

Holland, M.M., D. A. Bailey, B. P. Briegleb, B. Light, and E. Hunke. Improved sea ice shortwave radiation physics in CCSM4: the impact of melt ponds and aerosols on Arctic sea ice (2012). J. Climate, 25(5): 1413–1430, 2012. doi:10.1175/ JCLI-D-11-00078.1.

Gualdi S., A. Navarra, E. Guilyardi, and P. Delecluse, 2003: Assessment of the Tropical Indo-Pacific Climate in the SINTEX CGCM. Ann Geophys, 46, 1-26.

Gualdi S., A. Alessandri, and A. Navarra, 2005: Impact of atmospheric horizontal resolution on ENSO forecasts. Tellus, 57A, 357-374

Hunke, E. C., and Dukowicz, J. K. (1997). An elastic-viscous-plastic model for sea ice dynamics. Journal of Physical Oceanography, 27(9), 1849-1867.

Hunke, E. C., Lipscomb, W. H., & Turner, A. K. (2010). CICE: the Los Alamos Sea Ice Model Documentation and Software User's Manual Version 4.1 LA-CC-06-012. T-3

Fluid Dynamics Group, Los Alamos National Laboratory, 675.

Hurrell, James W., et al. (2013) The community earth system model: a framework for collaborative research. Bulletin of the American Meteorological Society 94(9):1339-1360.

Iacono M.J., J. S. Delamere, E. J. Mlawer, M. W. Shephard, S. A. Clough, and W. D. Collins. Radiative forcing by long-lived greenhouse gases: Calculations with the AER radiative transfer models (2008). J. Geo- phys. Res.: Atmospheres, 113(D13). doi:10.1029/2008JD009944.

Ingleby, B. and M. Huddleston, 2007: Quality control of ocean temperature and salinity profiles - Historical and real-time data. J. Mar. Syst., 65, 158–175.

IPCC (2013): Climate Change (2013): The Physical Science Basis. Contribution of Working Group I to the Fifth Assessment Report of the Intergovernmental Panel on Climate Change [Stocker, T.F., D. Qin, G.-K. Plattner, M. Tignor, S.K. Allen, J. Boschung, A. Nauels, Y. Xia, V. Bex and P.M. Midgley (eds.)]. Cambridge University Press, Cambridge, United Kingdom and New York, NY, USA, 1535 pp, doi:10.1017/CBO9781107415324.

Kalnay, E., Kanamitsu, M., Kistler, R., Collins, W., Deaven, D., Gandin, L., ... & Zhu, Y. (1996). The NCEP/NCAR 40-year reanalysis project. Bulletin of the American Meteorological Society, 77(3), 437-471.

Kim, H.M., P. Webster and J.A. Curry, 2012: Seasonal prediction skill of ECMWF System 4 and NCEP CFSv2 retrospective forecast for the Northern Hemisphere Winter, Clim Dyn, 39,2957–2973. DOI 10.1007/s00382-012-1364-6

Kirtman, B.P. et al., 2014: The North American Multimodel Ensemble -. Phase-1 Seasonal-to-Interannual Prediction; Phase-2 Toward Developing Intraseasonal Prediction, Bull. American. Met. Soc., April issue, 585-601.

Koster, R. D., Z. Guo, R. Yang, P. A. Dirmeyer, K. Mitchell, M. J. Puma, 2009: On the nature of soil moisture in land surface models. *J. Clim.*, **22**, 4322–4335. doi: http://dx.doi.org/10.1175/2009JCLI2832.1

Kucharik C.J. and K. R. Brye (2003). Integrated BIosphere Simulator (IBIS) Yield and Nitrate Loss Predictions for Wisconsin Maize Receiving Varied Amounts of Nitrogen Fertilizer. J. Environ. Qual., 32:247—268. doi:10.2134/jeq2003.2470.

Large W., Danabasoglu G. (2006). Attribution and impacts of upper- ocean biases in CCSM3. J Clim 19:2325–2345

Large, W. G. and S. G. Yeager, 2004: Diurnal to decadal global forcing for fcean and sea-ice models: the data sets and flux climatologies. Tech. Rep. No 460, NCAR Technical Note.

Lawrence, P.J., et al. (2012). "Simulating the biogeochemical and biogeophysical impacts of transient land cover change and wood harvest in the Community Climate System Model (CCSM4) from 1850 to 2100." Journal of Climate 25.9: 3071-3095.

Lawrence D.M., A. G. Slater, and S. C. Swenson (2011). Simulation of Present-Day and Future Permafrost and Seasonally Frozen Ground Conditions in CCSM4. J. Climate, 25(7):2207–2225. doi:10.1175/ JCLI-D-11-00334.1.

Li, J., and J. X. L. Wang, 2003: A new North Atlantic Oscillation index and its variability. Adv. Atmos. Sci., 20, 661–676, doi:10.1007/BF02915394.

Liu X., R. C. Easter, S. J. Ghan, R. Zaveri, P. Rasch, X. Shi, J.-F. Lamarque, A. Gettelman, H. Morrison, F. Vitt, A. Conley, S. Park, R. Neale, C. Hannay, A. M. L. Ekman, P. Hess, N. Mahowald, W. Collins, M. J. Iacono, C. S. (2012). Toward a minimal representation of aerosols in climate models: description and evaluation in the Community Atmosphere Model CAM5. Geosci. Model Dev., 5(3):709–739, 2012. doi: 10.5194/gmd-5-709-2012.

Madec, Gurvan (2008). NEMO ocean engine. Institut Pierre Simon Laplace, Note du Pole de Modelisation 27, 2008. URL: http://www.nemo-ocean.eu/ content/download/21612/97924/ file/NEMO_book_3_4.pdf.

Masato, G., B. J. Hoskins, and T. Woollings, 2012: Wave-breaking characteristics of midlatitude blocking. Quart. J. Roy. Meteor. Soc., 138, 1285–1296, doi:10.1002/qj.990.

Materia, S., Borrelli, A., Bellucci, A., Alessandri, A., Di Pietro, P., Athanasiadis, P., ... & Gualdi, S. (2014). Impact of atmosphere and land surface initial conditions on seasonal forecasts of global surface temperature. Journal of Climate, 27(24), 9253-9271.

Morrison, Hugh, and Andrew Gettelman (2008). "A new two-moment bulk stratiform cloud microphysics scheme in the Community Atmosphere Model, version 3 (CAM3). Part I: Description and numerical tests." Journal of Climate 21, 15, 3642-3659.

Neale R.B. and Coauthors (2010). Description of the NCAR Community Atmosphere Model (CAM 5.0). NCAR Technical Note NCAR/TN-486, National Center for Atmospheric Research. URL: http://www.cesm.ucar. edu/models/cesm1.1/cam/docs/description/cam5_desc.pdf.

Oleson K.W., G. B. Bonan, J. Feddema, M. Vertenstein, and C. Grimmond (2008). An ur- ban parameterization for a global climate model. Part I: Formulation and evaluation for two cities. J. of Appl. Meteor. and Climatol., 47(4):1038–1060, 2008. doi: 10.1175/2007JAMC1597.1.

Oleson, K. W., et al. (2013). Technical description of version 4.5 of the Community Land Model (CLM). NCAR Tech. Note NCAR/TN-503+ STR. National Center for Atmospheric Research, Boulder, CO, 422 pp. doi: 10.5065/D6RR1W7M, 2013.

Park. S. and C. S. Bretherton (2008). The University of Washington shallow convection and moist turbulence schemes and their impact on climate simulations with the Community Atmosphere Model. J. Climate, 22(12):3449–3469, 2009. doi:10. 1175/2008JCLI2557.1.

Palmer T.N., A. Alessandri, U. Andersen, P. Cantelaube, M. Davey, P. Délécluse, M. Déqué, E. Díez, F. J. Doblas- Reyes, H. Feddersen, R. Graham, S. Gualdi, J.-F. Guérémy, R. Hagedorn, M. Hoshen, N. Keenlyside, M. Latif, A. Lazar, E. Maisonnave, V. Marletto, A. P. Morse, B. Orfila, P. Rogel, J.-M. Terres, M. C. Thomson, 2004: Development of a European Multi-Model Ensemble System for Seasonal to Inter-Annual Prediction (DEMETER). Bull Amer Meteo Soc, 85, 853-872

Patera A.T. (1984). A spectral element method for fluid dynamics - Laminar flow in a channel expansion. Journal of Computational Physics, 54:468--488, 1984.

Pincus, R., H. W. Barker, and J.-J. Morcrette (2002). A fast, flexible, approximate technique for computing radiative transfer in inhomogeneous cloud fields. J. Geophys. Res.: Atmospheres, 108(D13), 2003. doi: 10.1029/2002JD003322.

Rayner N.A., Brohan P., Parker D.E., Folland C.K., Kennedy J.J., Vanicek M., Ansell T.J., Tett S.F.B., 2006: Improved analyses of changes and uncertainties in sea surface temperature measured in situ since the mid-nineteenth century: the HadSST2 dataset. J. Clim. 19(3): 446–469.

Reynolds, R. W., T. M. Smith, C. Liu, D. B. Chelton, K. S. Casey, and M. G. Schlax, 2007: Daily high-resolution blended analyses for sea surface temperature. J. Climate, 20, 5473–5496.

Richter, J. H., Solomon, A., & Bacmeister, J. T. (2014). Effects of vertical resolution and nonorographic gravity wave drag on the simulated climate in the Community Atmosphere Model, version 5. Journal of Advances in Modeling Earth Systems, 6(2), 357-383.

Riddle, E. E., A. H. Butler, J. C. Furtado, J. L. Cohen, and A. Kumar, 2013: CFSv2 ensemble prediction of the wintertime Arctic Oscillation. Climate Dyn., 41, 1099–1116, doi:10.1007/ s00382-013-1850-5.

Roemmich, D. and W. B. Owens, 2000: The Argo Project: global ocean observations for the understanding and prediction of climate variability. Oceanography, 13, 45-50

Scaife, A. A., T. Woollings, J. Knight, G. Martin, and T. Hinton, 2010: Atmospheric blocking and mean biases in climate models. J. Climate, 23, 6143–6152, doi:10.1175/2010JCLI3728.1.

Scaife, A. A. and Coauthors, 2011: Improved Atlantic winter blocking in a climate model. Geophys. Res. Lett., 38, L23703, doi:10.1029/ 2011GL049573.

Scaife, A. A. and Coauthors, 2014: Skillful long range prediction of European and North American winters. Geophys. Res. Lett., 41, 2514–2519, doi:10.1002/2014GL059637.

Shi, W., Schaller, N., MacLeod, D., Palmer, T. N.and Weisheimer, A. (2015), Impact of hindcast length on estimates of seasonal climate predictability. Geophys. Res. Lett., 42: 1554–1559. doi: 10.1002/2014GL062829.

Simmons, H. L., S. R. Jayne, L. C. St. Laurent, and A. J. Weaver (2004). Tidally driven mixing in a numerical model of the ocean general circulation. Ocean Modelling, 245–263.

Stanski H.R., L.J. Wilson and W.R. Burrows, 1989: ‘Survey of common verification methods in meteorology’, Technical report 8. WMO: Geneva, Switzerland.

Storto A., S. Dobricic, S. Masina, and P. Di Pietro (2011). Assimilating along-track altimetric observations through local hydrostatic adjustments in a global ocean reanalysis system. Mon. Wea. Rev. 139: 738-754.

Storto A, Masina S, Dobricic S. 2014. Estimation and impact of nonuniform horizontal correlation length scales for Global Ocean physical analyses. J. Atmos. Ocean. Technol. 31: 2330-2349.

Subin, Z. M., Riley, W. J., & Mironov, D. (2012). An improved lake model for climate simulations: Model structure, evaluation, and sensitivity analyses in CESM1. Journal of Advances in Modeling Earth Systems, 4(1).

Swenson, S. C., Lawrence, D. M., & Lee, H. (2012). Improved simulation of the terrestrial hydrological cycle in permafrost regions by the Community Land Model. Journal of Advances in Modeling Earth Systems, 4(3).

Thorndike, A. S., Rothrock, D. A., Maykut, G. A., & Colony, R. (1975). The thickness distribution of sea ice. Journal of Geophysical Research, 80(33): 4501-4513.

Thornton P.E., J.-F. Lamarque, N. A. Rosenbloom, and N. M. Mahowald (2007). Influence of carbon-nitrogen cycle coupling on land model response to CO2 fertilization and climate variability. Global Biogeochem. Cycles, 21(4). doi:10. 1029/2006GB002868.

Tibaldi, S., and F. Molteni, 1990: On the operational predictability of blocking. Tellus, 42A, 343–365, doi:10.1034/ j.1600-0870.1990.t01-2-00003.x.

Wallace, J. M., and D. S. Gutzler, 1981: Teleconnections in the geopotential height field during the Northern Hemisphere winter. Mon. Wea. Rev., 109, 784–812, doi:10.1175/ 1520-0493(1981)109,0784:TITGHF.2.0.CO;2.

Woollings, T., B. J. Hoskins, M. Blackburn, and P. Berrisford, 2008: A new Rossby wave–breaking interpretation of the North Atlantic Oscillation. J. Atmos. Sci., 65, 609–626, doi:10.1175/ 2007JAS2347.1.

Zalesak, S. T., 1979: Fully multidimensional flux corrected transport algorithms for fluids. J. Comput. Phys., 31.

Zender, Charles S., Huisheng Bian, and David Newman (2003). Mineral Dust Entrainment and Deposition (DEAD) model: Description and 1990s dust climatology. Journal of Geophysical Research: Atmospheres 108.D14

Zhang, J.L. and D.A. Rothrock, 2003. Modeling global sea ice with a thickness and enthalpy distribution model in generalized curvilinear coordinates. Mon. Weather Rev., 131, 845-861.

cmcc
Centro Euro-Mediterraneo sui Cambiamenti Climatici